



Observatório  
Nacional

PROGRAMA DE PÓS  
GRADUAÇÃO EM  
GEOFÍSICA

Ministério da  
Ciência, Tecnologia  
e Inovação



TESE DE DOUTORADO

PROCESSAMENTO E INVERSÃO DE DADOS DE  
CAMPOS POTENCIAIS:  
NOVAS ABORDAGENS

Vanderlei Coelho de Oliveira Junior

Orientadora

Valéria Cristina Ferreira Barbosa

Rio de Janeiro

2013

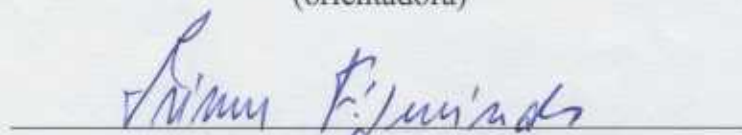
"PROCESSAMENTO E INVERSÃO DE DADOS DE CAMPOS POTENCIAIS:  
NOVAS ABORDAGENS"

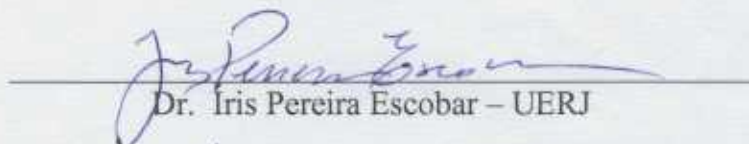
VANDERLEI COELHO DE OLIVEIRA JUNIOR

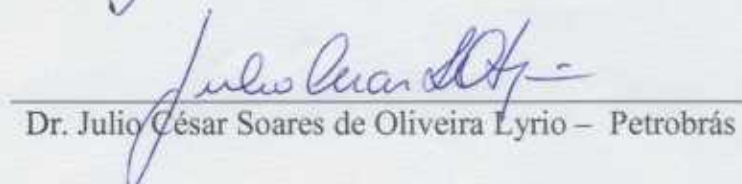
TESE SUBMETIDA AO CORPO DOCENTE DO PROGRAMA DE PÓS-GRADUAÇÃO  
EM GEOFÍSICA DO OBSERVATÓRIO NACIONAL COMO PARTE DOS REQUISITOS  
NECESSÁRIOS PARA A OBTENÇÃO DO GRAU DE DOUTOR EM GEOFÍSICA.

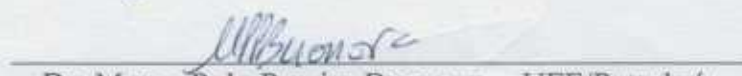
Aprovada por:

  
Dra. Valéria Cristina Ferreira Barbosa – ON/MCTI  
(orientadora)

  
Dr. Irineu Figueiredo – ON/MCTI

  
Dr. Iris Pereira Escobar – UERJ

  
Dr. Julio César Soares de Oliveira Lyrio – Petrobrás

  
Dr. Marco Polo Pereira Buonora – UFF/Petrobrás

RIO DE JANEIRO – BRASIL

16 DE JANEIRO DE 2013

PROCESSAMENTO E INVERSÃO DE DADOS DE CAMPOS POTENCIAIS:  
NOVAS ABORDAGENS

Vanderlei Coelho de Oliveira Junior

TESE SUBMETIDA AO CORPO DOCENTE DO PROGRAMA DE PÓS-GRADUAÇÃO  
EM GEOFÍSICA DO OBSERVATÓRIO NACIONAL COMO PARTE DOS REQUISITOS  
NECESSÁRIOS PARA OBTENÇÃO DO GRAU DE DOUTOR EM GEOFÍSICA.

Aprovada por:

---

Dra. Valéria Cristina Ferreira Barbosa (Orientadora)

---

Dr. Marco Polo Pereira Buonora

---

Dr. Julio Cesar S. O. Lyrio

---

Dr. Íris Pereira Escobar

---

Dr. Irineu Figueiredo

---

Dr. Cosme Ferreira da Ponte Neto (Suplente)

---

Dr. Fernando José Soares e Silva Dias (Suplente)

RIO DE JANEIRO - BRASIL  
2013

*“E nossa história não estará  
pelo avesso assim, sem final feliz.  
Teremos coisas bonitas pra contar.  
E até lá, vamos viver.  
Temos muito ainda por fazer,  
não olhe pra trás.  
Apenas começamos.  
O mundo começa agora.  
Apenas começamos”.*

Trecho de "Metal Contra as Nuvens", Legião Urbana

# AGRADECIMENTOS

A meus pais e a minha irmã, que sustentam os pilares da minha vida.

À minha orientadora Dra. Valéria C. F. Barbosa, que conduziu meus passos tal como uma segunda mãe e grande amiga.

Ao Conselho Nacional de Desenvolvimento Científico e Tecnológico (CNPq) pelo auxílio financeiro em forma de bolsa.

Ao Observatório Nacional por oferecer, assim como no mestrado, as melhores condições possíveis para que este trabalho fosse realizado.

Aos amigos do ON (em ordem alfabética para que não haja privilégio algum) Beck, Bonilla, Bruno, Cosme, Diego, Dionísio, Dona Emilia, Felipe Figura, Fillipe Cláudio, Gustavo Bragança, Jorge Leonardo, Papa, Pavel, Roig e Wallace.

Ao casal Balancin, que está sempre de braços abertos e desperta a minha admiração mais profunda.

Aos irmãos Leo, Saulo e Rodrigo, cuja amizade e companheirismo, tão importantes durante esta caminhada, eu seria incapaz de descrever com as palavras mais bonitas e sinceras que conheço.

Aos membros da banca, Professor Dr. Irineu, Professor Dr. Íris, Dr. Marco Polo e Dr. Julio Lyrio, por aceitarem revisar e contribuir com a conclusão deste trabalho.

A todos do centro Pae João da Caridade por toda a amizade e por todo o zelo constante.

A todos do Bazar da Cantoria, o palco das comemorações mais importantes.

Por último e não menos importante, à Florita, cujo sorriso é o céu, no branco do seu rosto, a irradiar ternura e cuja mão carrega a semente que inspira um beijo ardente, um convite para amar.

# SUMÁRIO

INTRODUÇÃO .....	1
PARTE A .....	3
PARTE B .....	52

## INTRODUÇÃO

No final de 2010, a empresa Bell Geospace Inc. forneceu ao Observatório Nacional dados de gradiometria gravimétrica provenientes de um aerolevante realizado por esta empresa sobre o domo de sal Vinton, localizado no estado da Louisiana, EUA. O acesso a este tipo de dado é difícil, uma vez que levantamentos dessa natureza são, em geral, realizados apenas por empresas mineradoras e de petróleo. A disponibilidade dos dados sobre o domo de sal Vinton possibilitou o desenvolvimento de pesquisa usando dados de gradiometria gravimétrica em ambiente de bacias sedimentares, que até então nunca havia sido feita pelo grupo de pesquisa liderado pela professora Valéria C. F. Barbosa, minha orientadora.

A primeira dúvida sobre os dados de gradiometria gravimétrica foi se seria necessário realizar algum tipo de processamento além dos já realizados pela empresa de aquisição. Este processamento seria feito com o intuito de avaliar a qualidade dos dados, verificar se seria necessário fazer algum tipo de separação regional-residual e se o ruído em todas as componentes era o mesmo. Tendo em vista que os dados medidos são irregularmente espaçados, a técnica escolhida para avaliar a qualidade dos dados, bem como processá-los, foi a camada equivalente. Além de permitir o processamento de dados irregularmente espaçados, a técnica da camada equivalente possibilita o processamento simultâneo de todas as componentes do tensor que, a princípio, são causadas pela mesma distribuição anômala de densidade em subsuperfície. A técnica da camada equivalente, no entanto, é computacionalmente custosa se o número de dados é muito grande. Essa

limitação computacional compromete a aplicação da técnica da camada equivalente convencional aos dados de gradiometria gravimétrica fornecidos pela empresa Bell Geospace Inc., uma vez que estes são provenientes de um aerolevante em grande escala. Este problema computacional nos motivou a desenvolver um método “rápido” para viabilizar o uso da camada equivalente no processamento de um grande volume de dados. A idéia é descrever a propriedade física dentro da camada equivalente por meio de funções polinomiais e estimar os coeficientes deste polinômio, ao invés de estimar a propriedade física de cada fonte equivalente que compõe a camada. Esta nova técnica, denominada *Camada Equivalente Polinomial*, foi aplicada com sucesso a dados magnetométricos e gravimétricos, resultando na publicação do artigo Oliveira Jr., V. C., Barbosa, V.C.F., and Uieda, L. (2013). "Polynomial equivalent layer." *GEOPHYSICS*, 78(1), G1–G13. doi: 10.1190/geo2012-0196.1, que compõe a parte A desta tese.

Paralelamente ao desenvolvimento do método *Camada Equivalente Polinomial*, eu adaptei a metodologia desenvolvida no mestrado, que é sobre inversão de dados gravimétricos, para a aplicação a dados de gradiometria gravimétrica. No decorrer desta adaptação, testes preliminares feitos via modelagem direta indicaram que não havia necessidade de realizar uma separação regional residual nos dados sobre o domo de sal Vinton. A adaptação da metodologia desenvolvida no mestrado, bem como a sua aplicação na interpretação dos dados sobre o domo de sal Vinton, resultaram no artigo intitulado “3-D radial gravity gradient inversion”, submetido à revista *Geophysical Journal International*, e compõe a parte B desta tese.

## **Parte A**

# **Polynomial Equivalent Layer**

## ABSTRACT

We have developed a new cost-effective method for processing large-potential-field data sets via the equivalent-layer technique. In this approach the equivalent layer is divided into a regular grid of equivalent-source windows. Inside each window, the physical-property distribution is described by a bivariate polynomial. Hence, the physical-property distribution within the equivalent layer is assumed to be a piecewise polynomial function defined on a set of equivalent-source windows. We perform any linear transformation of a large set of data as follows. First, we estimate the polynomial coefficients of all equivalent-source windows by using a linear regularized inversion. Second, we transform the estimated polynomial coefficients of all windows into the physical-property distribution within the whole equivalent layer. Finally, we pre-multiply this distribution by the matrix of Green's functions associated with the desired transformation to obtain the transformed data. The regularized inversion deals with a linear system of equations with dimensions based on the total number of polynomial coefficients within all equivalent-source windows. This contrasts with the classical approach of directly estimating the physical-property distribution within the equivalent layer, which leads to a system based on the number of data. Because the number of data is much larger than the number of polynomial coefficients, the proposed polynomial representation of the physical-property distribution within an equivalent layer drastically reduces the number of parameters to be estimated. By comparing the total number of floating-point operations required to estimate an equivalent layer via our method with the classical approach, both formulated with Cholesky's decomposition, we verify

that the computation time required for building the linear system and for solving the linear inverse problem can be reduced by as many as three and four orders of magnitude, respectively. Applications to both synthetic and real data show that our method performs the standard linear transformations of potential-field data accurately.

## INTRODUCTION

In accordance with potential theory, a discrete set of observations of a potential field produced by a 3D physical-property distribution can be exactly reproduced by a 2D physical-property distribution. This 2D physical-property surface distribution is continuous and infinite. In practice, it is approximated by a finite set of equivalent sources arranged in a layer with finite horizontal dimensions and located below the observation surface. Usually the equivalent sources are represented by magnetic dipoles, doublets, point masses or more complex sources, such as, prisms. In the literature, this layer that is made up of equivalent sources is referred to as the equivalent layer (Dampney, 1969).

By following the classical approach of the equivalent-layer principle, the physical property of each equivalent source is estimated by solving a linear inversion subject to fitting a discrete set of potential-field observations. Next, the estimated 2D physical-property distribution can be used to perform any standard linear transformation of the potential-field data such as interpolation (e.g., Cordell, 1992; Mendonça and Silva, 1994), upward (or downward) continuation (e.g., Emilia, 1973; Hansen and Miyazaki, 1984; Li and Oldenburg, 2010) and reduction to the pole of magnetic data (e.g., Silva 1986; Leão and Silva, 1989; Guspí and Novara, 2009). Specifically, the desired linear transformation of the potential-field data can be obtained by multiplying the matrix of Green's functions associated with the desired transformation by the estimated physical-property distribution (magnetization-intensity or density distributions).

The advent of airborne surveys made possible the acquisition of a huge volume of potential-field observations. In a typical airborne survey, these observations are collected every few meters, generating data sets that may contain hundreds of thousands observations (Uieda and Barbosa, 2012). Although airborne surveys provide high-resolution potential-field data, the processing of these large potential-field data sets may lead to costly computational schemes, such as the application of the equivalent-layer technique. Hence, the computational demand for performing discrete linear transformations of large potential-field data sets also increases. However, for processing a huge quantity of data via the equivalent-layer technique, a huge number of equivalent sources is required. Usually, the equivalent-layer technique requires a number of equivalent sources  $M$  greater than the number of observations  $N$ . The larger the number of equivalent sources, the smaller will be the dependence of the result on the type of source used (dipoles, prisms, etc.) and on the distribution of these sources within the equivalent layer. Thus, the use of a large number of equivalent sources increases the chance of the estimated physical-property distribution yields an acceptable data fit. On the other hand, a large number of equivalent sources makes the construction of the linear system and the solution of the resulting inverse problem prohibitively inefficient. Hence, the challenge for potential-field data processing via the equivalent-layer technique is that of a large-scale inversion. As properly pointed out by Barnes and Lumley (2011), the key to a successful equivalent-source processing scheme rests with carefully designed software that can handle large optimization problems efficiently. To overcome this difficulty, few methods have

been developed to make feasible the use of the equivalent-layer technique for processing large data sets.

Leão and Silva (1989) developed a fast method for performing any linear transformation of a large set of potential-field data using the equivalent-layer principle. These authors posed the linear inverse problem of estimating the physical properties of  $M$  equivalent sources from potential-field data in the data space. This leads to a linear system of equations with dimensions based on the number of data  $N$ , instead of the number of sources  $M$ . To greatly reduce the total processing time and memory requirements, Leão and Silva's (1989) method used a small-moving data window that is shifted over the whole gridded data set. By using the observations inside a small data window, Leão and Silva (1989) estimated the physical-property distribution of a set of equivalent sources forming a small equivalent layer. These authors set up an equivalent layer extending beyond the moving-data window and at a depth between two and six times the grid spacing of the observations. Next, they computed the transformed field at the center of the moving-data window only. This procedure is repeated for each position of a moving-data window which spans the data until the whole area is processed. Leão and Silva's (1989) method leads to a fast grid operator which is applied to the data by a procedure similar to a discrete convolution.

Mendonça and Silva (1994) developed the equivalent-data concept which makes the equivalent-layer technique a feasible interpolation method. The equivalent-data concept consists in determining a subset of all potential-field observations (named equivalent data) such that the estimated physical-property distribution within an equivalent layer that fits the determined subset

also fits the remaining potential-field observations automatically. The authors also pointed out that the computational efficiency of the method depends on the number of equivalent data. If the potential-field anomaly is nonsmooth, the number of equivalent data can be large and the method will be less efficient than the classical approach.

Li and Oldenburg (2010) developed a rapid method for processing large potential-field data sets by using the equivalent-layer principle. Li and Oldenburg's (2010) method uses the sparse wavelet representation of the matrix of Green's functions whose  $j$ th column contains the potential-field contribution of the  $j$ th equivalent source, with unit physical property, at the positions where the observations were made. To obtain a sparse representation of the matrix of Green's functions, Li and Oldenburg (2010) applied the 2D wavelet transform to each row and column of this matrix and set to zero the wavelet coefficients that are below a given threshold. Finally, these authors estimated the physical-property distribution within an equivalent layer by using the conjugate gradient least-squares strategy. By comparing with the classical equivalent-layer approach, the authors pointed out that, given the compression, their method reduces the computational time required for solving the linear system by as many as two orders of magnitude.

Barnes and Lumley (2011) reduced the noise level by a factor of 2.4 of the  $g_{zz}$  component of the gravity gradient tensor by using the equivalent layer technique. These authors grouped equivalent sources far from an observation point in blocks with average physical properties. This procedure aims at obtaining a linear system with a sparse matrix which reduces the memory storage and computational time. By using a weighted-least-squares conjugate-

gradient strategy, Barnes and Lumley (2011) solved the resulting linear inverse problem.

We present a new fast method for processing large potential-field data sets by applying the equivalent-layer technique. Our method divides the equivalent layer into a regular grid of equivalent-source windows inside which the physical-property distribution is described by bivariate polynomial functions. This polynomial representation of the physical-property distribution within the equivalent layer considerably decreases the number of parameters to be estimated in the linear inverse problem. Our inverse problem is posed in the space of the total number of polynomial coefficients within all equivalent-source windows. This contrasts with the classical equivalent layer technique, derived through operations within the data or model spaces. By comparing the classical equivalent layer technique with our method and formulating the corresponding linear inverse problems using Cholesky's decomposition, we illustrate that our method substantially reduces the required memory storage and number of floating-point operations. Tests conducted with large synthetic gravity- and magnetic-data sets and with a real magnetic-data set over the Goiás Magmatic Arc (in central Brazil) show the good performance of our method in producing equivalent layers able to carry out the standard linear transformations of potential-field data without a prohibitively costly computational load.

# METHODOLOGY

## Classical approach

Let  $\mathbf{d}$  be an  $N$ -dimensional vector of potential-field observations (gray dots in Figure A1a) and  $\mathbf{p}$  be an  $M$ -dimensional vector of the equivalent sources' physical-property values. We assume that the  $M$  equivalent sources (black dots in Figure A1b) are distributed in a regular grid with a constant depth  $z_0$  forming an equivalent layer. Usually, the equivalent sources can be either point of masses or dipoles, depending on the potential-field observations are gravity or magnetic data, respectively. Hence,  $\mathbf{p}$  contains a set of  $M$  densities, in the case of gravity data, or magnetic intensities, in the case of magnetic data. The potential field predicted by the equivalent layer at  $N$  observation points can be written in matrix notation as

$$\mathbf{g}(\mathbf{p}) = \mathbf{G}\mathbf{p} , \quad (\text{A1})$$

where  $\mathbf{g}(\mathbf{p})$  is an  $N$ -dimensional vector whose  $i$ th element  $g_i(\mathbf{p})$  is the potential-field data predicted at the  $i$ th observation point ( $x = x_i, y = y_i$ , and  $z = z_i$ , referred to a right-hand Cartesian coordinate system with the  $z$ -axis pointing downwards, Figure A1a) and  $\mathbf{G}$  is the  $N \times M$  matrix of Green's functions, whose  $ij$ th element is the potential field at the  $i$ th observation point produced by the  $j$ th equivalent source located at ( $x = x'_j, y = y'_j$ , and  $z = z_0$ , Figure A1b) and with unitary physical property.

In applying the classical equivalent-layer technique, the parameters to be estimated are the physical properties (densities or magnetic intensities) of the

$M$  equivalent sources (e. g., point of masses or dipoles). The inverse problem of estimating this discrete physical-property distribution (the parameter vector  $\mathbf{p}$ , in equation A1) from observed data is an ill-posed problem because its solution is non-unique and unstable. In the classical equivalent-layer technique a stable estimate of  $\mathbf{p}$  can be obtained by using a parameter-space approach with the zeroth-order Tikhonov regularization (Tikhonov and Arsenin, 1977), i.e.:

$$\mathbf{p}^* = (\mathbf{G}^T \mathbf{G} + \mu \mathbf{I})^{-1} \mathbf{G}^T \mathbf{d}, \quad (\text{A2})$$

where the superscript  $T$  stands for a transpose,  $\mu$  is a regularizing parameter and  $\mathbf{I}$  is an identity matrix of order  $M$ . After estimating the vector  $\mathbf{p}^*$ , a desired linear transformation, such as interpolation, reduction to the pole and upward (or downward) continuation, is performed by

$$\mathbf{t} = \mathbf{T} \mathbf{p}^*, \quad (\text{A3})$$

where  $\mathbf{t}$  is an  $N$ -dimensional vector containing the transformed field and  $\mathbf{T}$  is an  $N \times M$  matrix of Green's functions whose  $ij$ th element is the transformed field at the  $i$ th observation point (Figure A1a) produced by the  $j$ th equivalent source (Figure A1b) with unitary physical property. For example, if the desired transformation is an upward continuation of the gravity data, the  $ij$ th element of the matrix  $\mathbf{T}$  is the gravity effect at the continuation height produced by the  $j$ th point of mass located at  $(x'_j, y'_j, z_0)$  and with unitary density.

A linear transformation through the equivalent-layer technique is performed in two steps: 1) estimating the physical-property distribution (equation A2) and 2) performing a matrix-vector multiplication to obtain the transformed field (equation A3). In terms of computational load, the first step is the biggest obstacle in using the equivalent-layer technique. This step requires

the solution of a large linear system (equation A2) based on matrix  $(\mathbf{G}^T \mathbf{G} + \mu \mathbf{I})$  with dimension  $M \times M$ . Hence, the computational problem in forming and inverting an  $M \times M$  matrix is not feasible when the number of parameters is large. To avoid the dependence on the source pattern and on the spatial distribution of the sources within the equivalent layer, the equivalent-layer technique usually requires a number of equivalent sources  $M$  greater than the number of observations  $N$ , and thus, a large-scale inversion is expected.

Alternatively, a stable estimate of the parameter vector can be obtained by using a data-space approach with the zeroth-order Tikhonov regularization (Tikhonov and Arsenin, 1977), i.e.

$$\mathbf{p}^* = \mathbf{G}^T (\mathbf{G}\mathbf{G}^T + \mu \mathbf{I})^{-1} \mathbf{d}, \quad (\text{A4})$$

where  $\mathbf{I}$  is an identity matrix of order  $N$ . The data-space approach is computationally much more efficient than the parameter-space because it forms the  $N \times N$  matrix  $(\mathbf{G}\mathbf{G}^T + \mu \mathbf{I})$ , instead of the  $M \times M$  matrix in equation A2. To reduce even further the computational effort,  $\mathbf{p}^*$  (equation A4) can be obtained in two steps. In the first one, we solve the linear system

$$(\mathbf{G}\mathbf{G}^T + \mu \mathbf{I}) \mathbf{w} = \mathbf{d}, \quad (\text{A5})$$

where the vector  $\mathbf{w}$  is a dummy variable. In the second step we evaluate

$$\mathbf{G}^T \mathbf{w} = \mathbf{p}^* . \quad (\text{A6})$$

Although formulating the equivalent-layer problem in the data space (equation A4) reduces significantly the size of the linear system to be solved compared with the parameter-space approach (equation A2), the computational effort is still excessive. In practice, this makes it unfeasible when dealing with large values of  $N$  (i.e., the number of data). To overcome this difficulty, we

propose a new concept of equivalent layer that leads to a computationally efficient method to estimate  $\mathbf{p}^*$ .

### Polynomial equivalent layer (PEL)

Let an equivalent layer be composed of  $M$  equivalent sources (black dots in Figure A1b) whose physical properties (densities or magnetic intensities) are the elements of an  $M$ -dimensional parameter vector  $\mathbf{p}$ . Here, the equivalent sources consist of magnetic dipoles or point of masses, because they demand simple computer calculations. Let's divide this equivalent layer into  $Q$  equivalent-source windows (dashed rectangles in Figure A1b) with the same horizontal extensions and the same number  $M_s$  of equivalent sources, where  $M_s \ll M$  and  $M = M_s \cdot Q$ . Hence, we partition the parameter vector as  $\mathbf{p} = [\mathbf{p}^1 \dots \mathbf{p}^Q]^T$ , where  $\mathbf{p}^k$ ,  $k = 1, \dots, Q$ , is an  $M_s$ -dimensional vector containing the physical properties of the equivalent sources within the  $k$ th equivalent-source window. Here, the physical-property distribution within the  $k$ th window is described by a bivariate polynomial  $q_k$ ,  $k = 1, \dots, Q$ , of degree  $\alpha$ . The number  $P$  of constant coefficients of  $q_k$  is given by

$$P = \sum_{l=1}^{\alpha+1} l. \quad (\text{A7})$$

It follows that the physical-property values of the equivalent sources within the  $k$ th equivalent-source window,  $\mathbf{p}^k$ , can be expressed in terms of the coefficients  $c_l^k$ ,  $l = 1, \dots, P$ , of the  $\alpha$ th-order polynomial function  $q_k$ , i.e.,

$$\mathbf{p}^k = \sum_{l=1}^P \mathbf{b}_l^k c_l^k. \quad (\text{A8})$$

This linear relationship can be written in matrix notation as

$$\mathbf{p}^k = \mathbf{B}^k \mathbf{c}^k, \quad k=1, \dots, Q, \quad (\text{A9})$$

where  $\mathbf{c}^k$  is a  $P$ -dimensional vector whose  $l$ th element  $c_l^k$  is the  $l$ th coefficient of the polynomial  $q_k$ , and  $\mathbf{B}^k$  is an  $M_s \times P$  matrix whose  $l$ th column is the  $M_s$ -dimensional vector  $\mathbf{b}_l^k$ . A generic element of matrix  $\mathbf{B}^k$  is the first-order derivative of the  $\alpha$ th-order polynomial function  $q_k$  with respect to one of the  $P$  coefficients ( $c_1^k, \dots, c_P^k$ ). To illustrate this matrix, let's consider a  $k$ th equivalent-source window composed of  $M_s = 12$  equivalent sources whose physical-property distribution can be described by a second-order polynomial ( $\alpha = 2$  and  $P = 6$ , equation A7). In this case, the  $j$ th element of the  $12 \times 1$  parameter vector  $\mathbf{p}^k$  (equations A8 and A9) is

$$p_j^k = c_1^k + c_2^k x'_j + c_3^k y'_j + c_4^k x'^2_j + c_5^k x'_j y'_j + c_6^k y'^2_j, \quad j=1, \dots, 12 \quad (\text{A10})$$

and the  $12 \times 6$  matrix  $\mathbf{B}^k$  is

$$\mathbf{B}^k = \begin{bmatrix} 1 & x'_1 & y'_1 & x'^2_1 & x'_1 y'_1 & y'^2_1 \\ 1 & x'_2 & y'_2 & x'^2_2 & x'_2 y'_2 & y'^2_2 \\ \vdots & \vdots & \vdots & \vdots & \vdots & \vdots \\ 1 & x'_{M_s} & y'_{M_s} & x'^2_{M_s} & x'_{M_s} y'_{M_s} & y'^2_{M_s} \end{bmatrix}. \quad (\text{A11})$$

It is then clear that  $p_j^k$ ,  $j=1, \dots, 12$ , is numerically equal to the second-order polynomial  $q_k$  evaluated at the horizontal coordinates  $(x'_j, y'_j)$  of the  $j$ th equivalent source within the  $k$ th equivalent-source window.

Here, the physical-property distribution within the equivalent layer is assumed to be a set of  $Q$  piecewise  $\alpha$ th-order polynomial functions (i.e.,  $q_k$ ,

$k=1,\dots,Q$ ) defined on a user-specified set of  $Q$  equivalent-source windows. Hence, the physical-property distribution of the entire equivalent layer, which includes all equivalent sources from all windows, can be described as

$$\mathbf{p} = \mathbf{B}\mathbf{c} , \quad (\text{A12})$$

where  $\mathbf{B}$  is an  $M \times H$  matrix ( $H = P \cdot Q$ ) that can be partitioned as

$$\mathbf{B} = \begin{bmatrix} \mathbf{B}^1 & \mathbf{0} & \dots & \mathbf{0} \\ \mathbf{0} & \mathbf{B}^2 & \dots & \mathbf{0} \\ \vdots & \vdots & \ddots & \vdots \\ \mathbf{0} & \mathbf{0} & \dots & \mathbf{B}^Q \end{bmatrix} , \quad (\text{A13})$$

where  $\mathbf{0}$  is an  $M_s \times P$  matrix of zeros. The  $H$ -dimensional vector  $\mathbf{c}$  (equation A12) is partitioned as  $\mathbf{c} = [\mathbf{c}^{1T} \dots \mathbf{c}^{QT}]^T$ . Hence, the vector  $\mathbf{c}$  contains all coefficients describing all polynomial functions,  $q_k$ ,  $k=1,\dots,Q$ , which are associated with the  $Q$  equivalent-source windows composing the entire equivalent layer.

By using equation A12, the linear system in equation A1, of  $N$  equations in  $M$  unknowns, can be rewritten as

$$\mathbf{g}(\mathbf{p}) = \mathbf{G}\mathbf{B}\mathbf{c} . \quad (\text{A14})$$

Equation A14 represents a system of  $N$  linear equations in  $H$  unknowns.

In our approach, named Polynomial Equivalent Layer (PEL), we first solve the inverse problem of estimating the polynomial-coefficient vector  $\mathbf{c}$  from the potential-field observations. Next, we calculate the physical-property distribution using equation A12. Finally, we compute the desired transformation of the data using equation A3. To obtain a stable estimate  $\mathbf{c}$ , we impose the zeroth- and first-order Tikhonov regularization (Tikhonov and Arsenin, 1977).

Here, the linear inverse problem of estimating  $\mathbf{c}$  is formulated as an optimization problem of minimizing

$$\frac{f_g}{H} \|\mathbf{c}\|^2, \quad (\text{A15a})$$

and

$$\frac{f_g}{f_r} \|\mathbf{RBc}\|^2, \quad (\text{A15b})$$

subject to

$$\|\mathbf{g}(\mathbf{p}) - \mathbf{d}\|^2 = \delta, \quad (\text{A15c})$$

where  $\|\cdot\|$  is the Euclidean norm,  $\delta$  is the expected mean square of the noise realizations in the data, and  $\mathbf{R}$  is an  $L \times M$  matrix representing a set of  $L$  first-order differences (Aster et al., 2004). The zeroth-order Tikhonov regularization (equation A15a) imposes that all coefficients estimates (vector  $\mathbf{c}$ ) must be as close as possible to zero. The first-order Tikhonov regularization (equation A15b) imposes a smoothing constraint on estimated physical properties of the equivalent sources located at the boundary of adjacent windows. Finally,  $f_g$  and  $f_r$  are normalizing factors defined below.

By solving this constrained optimization problem (equation A15), we obtain the normal equation for the estimate  $\mathbf{c}^*$ , which is

$$[\mathbf{B}^T \mathbf{G}^T \mathbf{G} \mathbf{B} + \mu(\mu_0 \frac{f_g}{H} \mathbf{I} + \mu_1 \frac{f_g}{f_r} \mathbf{B}^T \mathbf{R}^T \mathbf{R} \mathbf{B})] \mathbf{c}^* = \mathbf{B}^T \mathbf{G}^T \mathbf{d}, \quad (\text{A16})$$

where  $\mathbf{I}$  is an identity matrix of order  $H$  and  $\mu$  is the regularizing parameter that balances the relative importance between the data-misfit function (equation A15c) and the two constraints (equations A15a and A15b). The constants  $\mu_0$  and  $\mu_1$  (in equation A16) are real-positive numbers controlling the importance of

the two constraints given by equations A15a and A15b, respectively. The normalizing factors  $f_g$  and  $f_r$  are the traces of the matrices  $\mathbf{B}^T \mathbf{G}^T \mathbf{G} \mathbf{B}$  and  $\mathbf{B}^T \mathbf{R}^T \mathbf{R} \mathbf{B}$ , respectively.

Equation A16 represents a system of  $H$  linear equations in  $H$  unknowns, where  $H$  is the total number of polynomial coefficients forming all equivalent-source windows. This number of coefficients is much smaller than both the number of equivalent sources  $M$  and the number of data  $N$ . Thus, the PEL requires much less computational effort than the classical equivalent-layer approach, even in the data-space formulation, which requires the solution of a system of  $N$  equations in  $N$  unknowns (equation A4). In our PEL algorithm, the full  $N \times M$  matrix of Green's functions  $\mathbf{G}$  and the full  $M \times H$  matrix  $\mathbf{B}$  (equation A13) are not stored; rather only the small  $H \times H$  matrix  $\mathbf{B}^T \mathbf{G}^T \mathbf{G} \mathbf{B}$  (equation A16) is directly computed and stored. In our approach, the elements of the matrices  $\mathbf{G}$  and  $\mathbf{B}$  are computed on demand. We compute only the row of  $\mathbf{G}$  and the column of  $\mathbf{B}$  needed to calculate an element of the matrix  $\mathbf{G} \mathbf{B}$ . The same procedure is adopted to compute the  $H \times H$  matrix  $\mathbf{B}^T \mathbf{R}^T \mathbf{R} \mathbf{B}$  (equation A16). Once the vector  $\mathbf{B}^T \mathbf{G}^T \mathbf{d}$  and the matrices  $\mathbf{B}^T \mathbf{G}^T \mathbf{G} \mathbf{B}$  and  $\mathbf{B}^T \mathbf{R}^T \mathbf{R} \mathbf{B}$  are computed, they are stored and then several reruns of the PEL program may be performed by setting different values for the inversion control constants ( $\mu, \mu_0$  and  $\mu_1$ , equation A16). The choice of these constants will be discussed later.

## Computational efficiency of the PEL

The application of the equivalent-layer technique for processing potential-field data sets requires overcoming two main obstacles. The first one is the construction of the linear system. The second obstacle is the computational effort required to solve the resulting linear system. The PEL approach overcomes the first obstacle, mainly because of the sparseness of the matrix  $\mathbf{B}$  (equation A13). The second obstacle is overcome by the PEL because it leads to a linear system of equations with dimensions based on the number of coefficients  $H$  within all equivalent-source windows, where  $H$  is much smaller than the number of parameters  $M$  and the data  $N$ . To illustrate the efficiency of the PEL when compared with the classical equivalent layer approach, we analyze below the total number of floating-point operations (flops) by solving the corresponding linear systems through Cholesky's decomposition.

Following Boyd and Vandenberghe (2004), we define a flop as an addition, subtraction, multiplication, or division of two floating-point numbers. In the classical equivalent-layer approach, the number of flops  $m_s$  required to solve the linear system (equation A5) by Cholesky's decomposition is

$$m_s = \frac{1}{3}N^3 + 2N^2. \quad (\text{A17a})$$

The construction of the linear system and the evaluation of the auxiliary operations (equation A6) requires  $m_c$  flops, where

$$m_c = MN^2 + 2NM, \quad (\text{A17b})$$

in which  $MN^2$  and  $2NM$  are the flops to evaluate  $\mathbf{GG}^T$  and equation A6, respectively. Thus, obtaining  $\mathbf{p}^*$  by using the classical equivalent-layer

approach posed in the data-space formulation (equations A5 and A6) requires  $m_s + m_c$  flops.

Conversely, solving the resulting linear system in the PEL approach (equation A16) from Cholesky's decomposition requires  $h_s$  flops, where

$$h_s = \frac{1}{3}H^3 + 2H^2. \quad (\text{A18a})$$

By taking advantage of the sparseness in  $\mathbf{B}$  (equation A13), the number of flops  $h_c$  required to construct the linear system and evaluate the auxiliary operations is given by

$$h_c = 2NM_sH + H^2N + 2NH + 2MP, \quad (\text{A18b})$$

where  $2NM_sH$ ,  $H^2N$ ,  $2NH$  and,  $2MP$  are the number of flops required to evaluate the terms  $\mathbf{GB}$ ,  $\mathbf{B}^T\mathbf{G}^T\mathbf{GB}$ ,  $\mathbf{B}^T\mathbf{G}^T\mathbf{d}$ , and the physical-property distribution (the parameter vector  $\mathbf{p}$  in equation A12), respectively. Notice that the use of zeroth-order Tikhonov regularization in the classical equivalent-layer approach (equation A4) and in the PEL approach (equation A16) demands, respectively,  $N$  and  $H$  addition operations; this is equivalent to add  $N$  flops to  $m_c$  (equation A17b) and  $H$  flops to  $h_c$  (equation A18b). Because  $H$  is much smaller than  $N$  ( $H \ll N$ ), the use of zeroth-order Tikhonov regularization in the PEL requires much less computational effort than in the classical equivalent-layer approach. On the other hand, the classical equivalent-layer approach (equations A2 and A4) does not use the first-order Tikhonov regularization. Thus, one might think that its use in the PEL (equation A16) would increase the number of flops  $h_c$  (equation A18b) because the demand of evaluating the term  $\mathbf{B}^T\mathbf{R}^T\mathbf{RB}$ . This is not true because the sparseness of matrices  $\mathbf{B}$  and  $\mathbf{R}$  leads to a negligible increase of the  $h_c$  flops (equation A18b). Notice that the PEL

requires the additional step of calculating the physical-property distribution (equation A12) after solving the linear system of equations to estimate the polynomial coefficients (equation A16). This must be done before computing the desired transformation of the data (equation A3). This additional step does not increase the computational cost significantly, because computing the physical-property distribution (equation A12) only requires a sparse matrix-vector multiplication. To sum up, even using an additional regularizing function (equation A15b) and introducing an extra step in the processing workflow (equation A12), our equivalent-layer approach (PEL) requires a lower computational effort when compared to the classical equivalent-layer approach even using the  $N$ -dimensional-data-space formulation (equation A4).

We stress that the use of Cholesky's decomposition to solve the resulting linear system of equations for both the PEL and the classical equivalent-layer approach is only taken as an example. Further optimization of the PEL approach is still possible by solving the linear system through a preconditioned conjugate gradient method. Regardless the algorithm used to solve the linear system in the equivalent-layer problem, the  $H$ -dimensional system of equations to be solved by the PEL is always smaller than the  $N$ -dimensional system of equations required by the classical data-space approach. Ergo, solving  $H \times H$  systems is much more efficient, in terms of time and memory requirements, than solving  $N \times N$  systems.

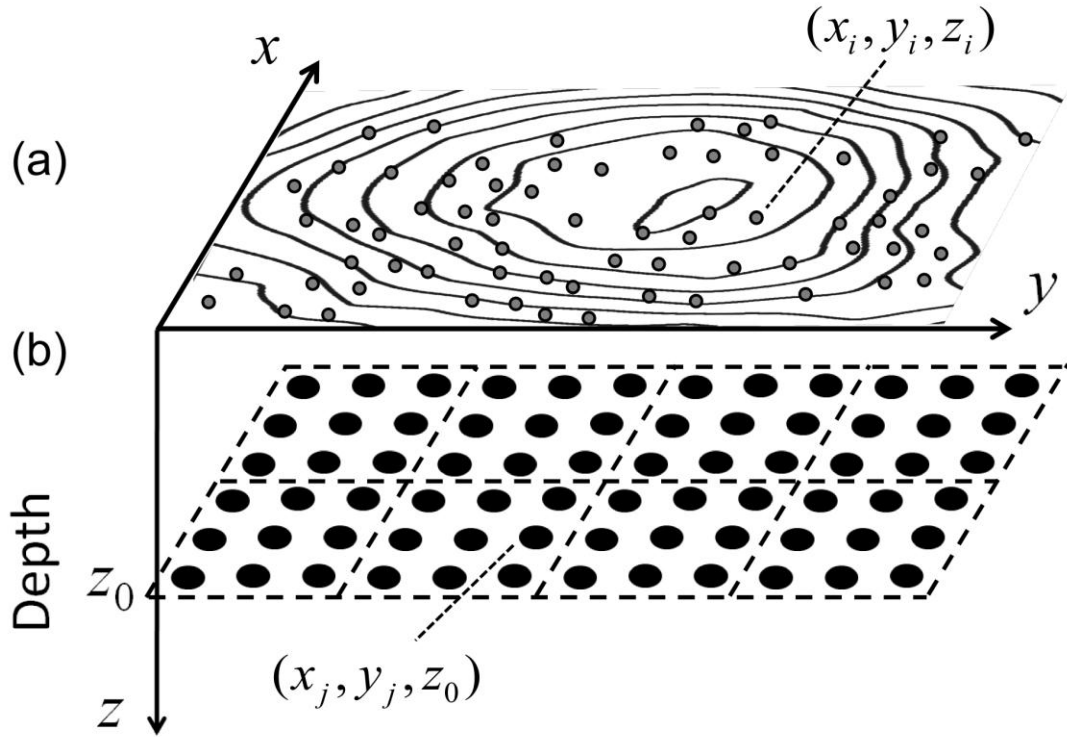


Figure A1 – Schematic representation of the equivalent layer. (a) Observed potential-field anomaly (black contour lines) measured at a set of  $N$  observation points (gray dots) located at coordinates  $(x_i, y_i, z_i)$ ,  $i = 1, \dots, N$ . (b) The equivalent layer is a thin slab in the subsurface which contains  $M$  fictitious equivalent sources (black dots) distributed in a grid at constant depth  $z_0$ . These sources are located at coordinates  $(x'_j, y'_j, z_0)$ ,  $j = 1, \dots, M$ , and they can be point masses (in the case of gravity data) or dipoles (in the case of magnetic data). This equivalent layer is divided into  $Q$  equivalent-source windows (dashed rectangles).

## PRACTICAL PROCEDURES

The practical procedures to use the PEL require the choice of two sets of variables. The first one is related to the geometry of the PEL and consists in choosing: (1) the depth to the equivalent layer ( $z_0$ ), (2) the degree  $\alpha$  of the polynomials describing the physical-property distribution within each equivalent-source window, (3) the size of the equivalent-source windows, (4) the number of equivalent-source windows  $Q$ , and (5) the number  $M_s$  of equivalent sources forming each equivalent-source window. The second set of variables to be assigned is the inversion control constants ( $\mu$ ,  $\mu_0$  and  $\mu_1$ , equation A16).

### Choice of the geometry of the PEL

Compared with the fast Fourier transform filtering technique, methods that employ the equivalent-layer technique for processing potential-field data usually do not require gridded data. Likewise, our formulation (PEL) does not require gridded data. Conversely, a common restriction of methods that employ the equivalent-layer technique concerns the vertical distance between the equivalent layer and the surface containing the potential-field observations. Some authors investigated this restriction empirically by using gridded data and established that the vertical distance between the equivalent layer and the surface containing the potential-field observations must be between two and six times the grid spacing of the observations (Dampney, 1969; Leão and Silva, 1989). The applications of the PEL have not shown a strong dependence with

respect to the vertical coordinate  $z_0$  of the equivalent layer. In practice, the equivalent layer in our formulation can be placed at a constant-vertical position  $z_0$  varying from about 150 to 300 m below the average height of the potential-field observations. Conversely, the dependence of the PEL on the size of the equivalent-source window and on the degree  $\alpha$  of the polynomials is more critical. Moreover, the chosen size of the equivalent-source window will be strongly dependent on the choice of the degree  $\alpha$  of the polynomials. Both choices must be grounded on the complexity of the potential-field anomalies. If the potential-field anomaly is characterized by long wavelength, we may use a large equivalent-source window and a high degree of the polynomial (e.g.,  $\alpha = 3$ ). Conversely, if the potential-field anomaly contains short-wavelength and high-amplitude components, we may use a small equivalent-source window and a low degree of the polynomial (e.g.,  $\alpha = 1$ ). This relation is illustrated later in the applications to synthetic and real data sets. A conservative practice when applying the PEL is to choose a small equivalent-source window and a low degree  $\alpha$  of the polynomial. This conservative option is recommended when the potential-field anomaly contains both long- and short-wavelength spectral contents. Additionally, we stress that this conservative choice works well even in the case of smooth anomalies with long-wavelength components only. Regardless of the chosen size of the equivalent-source window and degree  $\alpha$  of the polynomials, the estimated physical-property distribution of the PEL must produce a predicted data that fit the potential-field observations.

The division of the equivalent layer into  $Q$  equivalent-source windows consists of the following steps.

1) The interpreter must establish the smallest horizontal length  $L_s$  of a data square which contains a potential-field response with a short-wavelength. This square represents the area of an equivalent-source window.

2) The number of equivalent-source windows  $Q_x$  and  $Q_y$  in the  $x$  and  $y$  directions, respectively, are defined as

$$Q_x = \left\lceil (L_x / L_s) \right\rceil, \quad (\text{A19})$$

and

$$Q_y = \left\lceil (L_y / L_s) \right\rceil, \quad (\text{A20})$$

where  $L_x$  and  $L_y$  are the maximum horizontal lengths of the whole surveyed area in the  $x$  and  $y$  directions, respectively, and  $\left\lceil \right\rceil$  is the ceiling function (Graham et. al., 1988), which is defined as the least integer greater than or equal to its argument.

3) The number of equivalent-source windows  $Q$  is defined as

$$Q = Q_x \cdot Q_y. \quad (\text{A21})$$

4) Within each equivalent-source window, the number of equivalent sources in the  $x$  and  $y$  directions is the same and equal to

$$m = \left\lceil \sqrt{N/Q} \right\rceil, \quad (\text{A22})$$

where  $N$  is the number of potential-field observations.

5) Finally, the number of equivalent sources forming each equivalent-source window is defined as

$$M_s = m^2. \quad (\text{A23})$$

### **Choice of the inversion control constants**

The choice of the values of inversion control constants ( $\mu$ ,  $\mu_0$  and  $\mu_1$ , equation A16) is required to obtain a stable physical-property distribution via PEL. In practice, the value assigned to the regularizing parameter  $\mu$  is the unit. The values assigned to  $\mu_0$  and  $\mu_1$  are selected in such a way that the estimated physical-property distribution is stable and fits acceptably the observed data. If the values of  $\mu_0$  and  $\mu_1$  are poorly assigned, the estimated physical-property distribution within the equivalent layer does not fit the data.

We adopted the following practical procedure to choose  $\mu_0$  and  $\mu_1$ . Starting with small tentative values of  $\mu_0$  and  $\mu_1$ , we estimate the physical-property distribution within the equivalent layer through the PEL approach (equations A16 and A12). If this estimate yields an unacceptable data fit, the value of  $\mu_0$  is maintained, the value of  $\mu_1$  is increased (by multiples of 10) and the PEL algorithm is rerun (equation A16) to estimate a new physical-property distribution (equation A12). In the following numerical applications,  $\mu_1$  is defined in the range of  $10^{-7} \leq \mu_1 \leq 10^{-1}$  and  $\mu_0$  is kept fixed at a very small value such as  $10^{-15}$ .

These constants can be easily tuned through trial and error because, as pointed out before, our equivalent-layer method (PEL) is computationally

efficient by solving a small  $H$ -dimensional system of equations. Furthermore, after computing the vector  $\mathbf{B}^T \mathbf{G}^T \mathbf{d}$  and the matrices  $\mathbf{B}^T \mathbf{G}^T \mathbf{G} \mathbf{B}$ , and  $\mathbf{B}^T \mathbf{R}^T \mathbf{R} \mathbf{B}$  (equation A16), they are stored and then several reruns of the PEL algorithm may be performed by setting different values for the inversion control constants ( $\mu_0$  and  $\mu_1$ , equation A16).

## APPLICATION TO SYNTHETIC DATA

We illustrate the use of the PEL approach in processing synthetic gravity and magnetic data produced by simulated bodies. In applying the PEL approach to synthetic gravity data, we perform an upward continuation of the data set. In the application to synthetic magnetic data, the PEL approach is used to obtain the reduced-to-the-pole field.

### Synthetic-gravity data set

We simulate a set of  $N = 10,000$  noise-corrupted gravity observations (black lines and gray-scale map in Figure A2a), computed on a plane at  $z = -150$  m. The observations are produced by multiple sources (not shown) and are simulated on unevenly spaced stations. We corrupted the theoretical anomaly with zero-mean Gaussian pseudorandom noise with a standard deviation of 0.1 mGal. We set up a PEL with  $M = 10,000$  equivalent sources (point masses) distributed on a regular grid at constant depth  $z_0 = 200$  m. We divide this equivalent layer into  $Q = 100$  equivalent-source windows arranged in a grid of  $10 \times 10$  windows, each containing  $M_s = 100$  equivalent sources. The area of an equivalent-source window is shown projected onto the data as the white open rectangle in Figure A2a. We used third-order polynomials ( $\alpha = 3$ ) with  $P = 10$  coefficients each (equation A7), totaling  $H = 1000$  unknown coefficients which describe all  $Q$  polynomials that compose the equivalent layer. By setting  $\mu_0 = 10^{-15}$  and  $\mu_1 = 10^{-7}$ , the estimated  $H$  coefficients ( $\mathbf{c}^*$  in equation A16)

are used to compute an estimated density distribution ( $\mathbf{p}$ , in equation A12) in the equivalent layer. This layer produces a predicted gravity data set at  $z = -150$  m (in dashed white lines) which fits the simulated gravity data (in black lines and gray-scale map) as shown in Figure A2a. Figure A2b shows that the gravity data continued to a constant-vertical coordinate  $z = -500$  m using the estimated PEL (dashed white lines) agree very well with the true data computed at the same continuation height (black lines and gray-scale map). Histograms of the data misfits (insets of Figures A2a and A2b) corroborate the acceptance of the data fitting. In both histograms, most of the data misfits are smaller than the one standard deviation of the observational uncertainty being consistent with a normal distribution.

In this test, the efficiency of PEL approach comes from solving a 1000 x 1000 system versus a 10,000 x 10,000 system required by the classical equivalent-data approach in the data space. By using the Cholesky's decomposition as the algorithm for solving the linear systems, the number of flops required by the classical approach to solve the linear system (equation A17a) is approximately 994 times greater than that required by the PEL (equation A18a). Additionally, the construction of the linear systems (equations A17b and A18b) requires approximately 83 times more flops for the classical approach than that for the PEL.

In the previous section, we presented the practical procedures of choosing i) the degree  $\alpha$  of the polynomials describing the physical-property distribution within each equivalent-source window and ii) the size of the equivalent-source window. According to the criterion described in the previous section, if the potential-field anomaly is dominated by long-wavelength spectral

content (a smooth anomaly) there are two options. First, using a large equivalent-source window and a high degree  $\alpha$  of the polynomial, as in the application to synthetic-gravity data set presented above (Figures A2a and b). Second, using a small equivalent-source window and a low degree of the polynomial, following a conservative practice. To illustrate this conservative practice, we reproduced the previous application to synthetic-gravity data, only this time dividing the equivalent layer into  $Q = 400$  equivalent-source windows arranged in a grid of  $20 \times 20$  windows, each containing  $M_s = 25$  equivalent sources. The white open rectangle in Figure A2c represents the projection of the area of the equivalent-source window onto the data. Additionally, we used first-order polynomials ( $\alpha = 1$ ) with  $P = 3$  coefficients, totaling  $H = 1200$  unknown coefficients which describe all  $Q$  polynomials within the equivalent layer. This estimated equivalent layer produces a predicted gravity data set (dashed white lines) which fits the simulated gravity data (black lines and gray-scale map). The gravity data continued to a constant-vertical coordinate  $z = -500$  m using the estimated PEL (dashed white lines in Figure A2d) fit the true data computed at the same continuation height (black lines and gray-scale map in Figure A2d) equally well when compared with the previous result (Figure A2b). This shows the excellent performance of our method in upward-continuing the gravity data to an elevation of -500 m by using a conservative choice of both the size of the equivalent-source window and the degree  $\alpha$  of the polynomials. Histograms of the data misfits (insets of Figures A2c and A2d) resemble bell-shaped distributions confirming that the simulated measurement errors are normally distributed. In this test we set  $\mu_0 = 10^{-15}$  and  $\mu_1 = 10^{-7}$ ,

Regarding the computational performance, the PEL leads to computational efficiency by dealing with a  $1200 \times 1200$  system versus a  $10,000 \times 10,000$  one. By solving the resulting linear systems through Cholesky's decomposition, the number of flops required by the classical approach to solve and build the linear system is 576 times and 67 times greater than that required by the PEL, respectively. Thus, we verify that the PEL still provides a significant increase in performance, even if using a conservative choice of the size of the equivalent-source window and of the degree  $\alpha$  of the polynomials.

#### *Efficiency versus data-misfit measure*

As pointed out in the methodology section, PEL greatly reduces the linear system of equations to be solved by representing the physical-property distribution within the equivalent layer as a set of piecewise-polynomial functions. By taking a fixed size of equivalent-source window, the smaller the degree  $\alpha$  of the polynomial the smaller the number of the coefficients to be estimated ( $\mathbf{c}^*$  in equation A16), hence the smaller the  $H$ -dimensional system of equations to be solved by PEL and the faster the inversion will be. Then, it would be always desirable to use low-degree polynomials. This is true (or not), depending on whether the estimated physical-property distribution yields an acceptable (or unacceptable) data fit.

As discussed in the practical procedures section, PEL depends on the choice of the size of the equivalent-source window and on the choice of the degree  $\alpha$  of the polynomials. For a chosen size of the equivalent-source window, we can access the optimum degree  $\alpha$  of the polynomials. The optimum value for  $\alpha$  is the smallest one still producing an acceptable data fit.

This criterion ensures a maximum computational efficiency and a satisfactory data fitting. Thus, there is a trade-off between the computational efficiency and the data-misfit measure obtained by assigning different values of  $\alpha$ , for a given fixed size of the equivalent-source window in applying PEL approach.

Here, we analyze the trade-off between the data-misfit measure and the computational efficiency of our equivalent-layer approach (PEL) by assigning different degrees  $\alpha$  of the polynomials, for a given fixed size of the equivalent-source window. Figure A3 shows two curves plotted against  $\alpha$ : 1) the data-misfit measure (dashed line) and 2) the computational efficiency (solid line) of our equivalent-layer approach (PEL). These curves were computed by assuming the same size of the equivalent-source window shown in Figure A2a (white open rectangle). The computational efficiency of our equivalent-layer approach (PEL) is computed by the ratio  $N/H$  which represents a compression ratio of the linear system. We pointed out in the methodology section that small values of  $H$  lead to a great reduction of the size of the linear system to be solved through PEL (equation A16). For increasingly higher values of  $\alpha$ , the values of  $H$  increase and the computational efficiency of PEL becomes increasingly lower. Hence, the computational efficiency of PEL ( $N/H$ ) decreases with increasing  $\alpha$ .

The optimum value for  $\alpha$ , for a given fixed size of the equivalent-source window, is the smallest one still producing an acceptable data fit. This choice ensures the best computational efficiency of PEL in addition to fitting the geophysical observations. In Figure A3, the optimum value of  $\alpha$  is 3 which is the value used in Figures A2a and A2b. The data-misfit measure is computed as the square of the Euclidean norm of the residual between the observed and

fitted data divided by the number of observations. Depending on the size of the equivalent-source window used, values from  $\alpha$  different of the optimum value produce a poor data fit increasing the data-misfit measure. Values of  $\alpha$  smaller than an optimum value (e.g.,  $\alpha < 3$  in Figure A3) produce a poor data fit, increasing the data-misfit measure. This occurs because the size of the equivalent-source window is large and the low-degree polynomial used is not able to estimate a physical-property distribution (equations A16 and A12) that fits acceptably the data. Hence, the estimate of a physical-property distribution within the equivalent layer is roughly represented by piecewise  $\alpha$ th-order polynomial functions defined on a set of equivalent-source windows. Conversely, values of  $\alpha$  larger than an optimum value (e.g.,  $\alpha > 3$  in Figure A3) produce a poor data fit, increasing the data-misfit measure. This behavior occurs in PEL, because the inverse problem becomes ill-posed and, consequently, the tuning of the inversion control constants ( $\mu_0$  and  $\mu_1$ , equation A16) becomes difficult. Figure A3 illustrates the best trade-off between data-misfit measure (dashed line) and computational efficiency (solid line) of PEL in which  $\alpha = 3$  is the optimal balance of these two terms.

## Synthetic-magnetic data set

In this test, we simulate a complex magnetic response containing short- mid- and long-wavelength spectral contents. Because of this wide range of spectral contents, we must use a polynomial with a low degree ( $\alpha = 1$ ) and a small equivalent-source window whose size is able to contain the shortest wavelength of the simulated anomaly. As pointed out, the size of the equivalent-source window can be easily chosen. Here, we illustrate how we can check if this size was suitably chosen. To this end, we apply the PEL by setting large- and small-equivalent-source windows which illustrate, respectively, unsuitable and suitable windows.

Figure A4 shows the noise-corrupted total-field anomaly (black contour lines) produced by a set of synthetic bodies (not shown). We corrupted the theoretical anomaly with zero-mean Gaussian pseudorandom noise with a standard deviation of 5 nT. We simulated an airborne magnetic survey covering an area with an extent of 10,000 km in the  $x$ - and  $y$ -directions (north-south and east-west, respectively). The flight height is 150 m above the ground surface. The simulated flight pattern contains 50 flight-lines along north-south direction with line spacing of 200 m and 2 tie-lines along east-west direction with line spacing of 4000 m. Based on an average 270 km/h aircraft speed, the sampling frequency is 10 Hz and the number of data points per flight-line is 1333. The number of observations along the north-south and east-west are, respectively, 66,650 and 2666, totaling 69,316 observations. The simulated geomagnetic field has  $45^\circ$  declination and  $-3^\circ$  inclination. The simulated bodies (not shown) are magnetized uniformly, with a magnetization declination of  $-10^\circ$

and inclination of  $2^\circ$ . Notice that the spectral content of the magnetic response ranges from short to long wavelengths. At the northwestern (A) and easternmost (B) portions of the total-field anomaly map (Figure A4 in black contour lines), the magnetic responses are characterized predominantly by short- and long-wavelength spectral contents, respectively. Whereas, the magnetic response at the southernmost portion (C) contains mid-wavelength anomalies.

#### *Large-equivalent-source window*

We set up a PEL with  $M = 74,529$  equivalent sources (magnetic dipoles) distributed on a regular grid at constant depth  $z_0 = 200$  m. These magnetic dipoles have the same magnetization direction of the simulated body. This equivalent layer is divided into  $Q = 169$  equivalent-source windows arranged in a grid of  $13 \times 13$  windows, each one containing  $M_s = 441$  equivalent sources arranged in a grid of  $21 \times 21$  dipoles. The black open rectangle in Figure A4a shows the area of an equivalent-source window projected onto the data set. We used first-order polynomials ( $\alpha = 1$ ) with  $P = 3$  coefficients (equation A7), totaling  $H = 507$  unknown coefficients which describe all  $Q$  polynomials composing the equivalent layer. In this test we set  $\mu_0 = 10^{-15}$  and  $\mu_1 = 10^{-1}$ . After estimating the  $H$  coefficients (equation A16), we compute the magnetization-intensity distribution in the equivalent-source layer (equation A12) as show in Figure A5a. We also compute the predicted total-field anomaly (not shown) yielded by the magnetization-intensity distribution (Figure A5a) obtained through the PEL using a large equivalent-source window. Figure A4a

shows the differences (color-scale map) between the simulated noise-corrupted (black contour lines) and predicted (not show) total-field anomalies at  $z = -150$  m. For most of the area, these differences are around zero nT. Larger differences (smaller than -60 nT or greater than 60 nT) coincide exclusively with the region where the magnetic responses are characterized mainly by short-wavelength spectral contents (region A in Figure A4a). In this test, this poor data fit produced by the PEL occurs because of the low-degree polynomial combined with the large-equivalent-source window. This combination leads to a rough estimate of physical-property distribution (Figure A5a) within the equivalent layer. Because of this unacceptable anomaly fit, the choice of the size of the equivalent-source window (black open rectangle in Figure A4a) is considered unsuitable and the transformation of the data will not be done. In this case, the size of the equivalent-source window must be reduced until an acceptable data fit is obtained.

#### *Small-equivalent-source window*

We set up a PEL with  $M = 75,625$  equivalent sources (magnetic dipoles) distributed on a regular grid at constant depth  $z_0 = 200$  m. These magnetic dipoles have the same magnetization direction of the simulated body. This equivalent layer is divided into  $Q = 625$  equivalent-source windows arranged in a grid of  $25 \times 25$  windows, each one containing  $M_s = 121$  equivalent sources arranged in a grid of  $11 \times 11$  dipoles. The black open rectangle in Figure A4b shows the area of an equivalent-source window projected onto the data set. We set  $\mu_0 = 10^{-15}$  and  $\mu_1 = 10^{-1}$ . We used first-order polynomials ( $\alpha = 1$ ) with  $P =$

3 coefficients (equation A7), totaling  $H = 1875$  unknown coefficients which describe all  $Q$  polynomials composing the equivalent layer. After estimating the  $H$  coefficients, we compute the magnetization-intensity distribution in the equivalent-source layer (Figure A5b). By setting a small-equivalent-source window in applying PEL, the differences (color-scale map in Figure A4b) between the simulated noise-corrupted (black contour lines in Figure A4b) and predicted (not show) total-field anomalies at  $z = -150$  m are much smaller than those obtained by setting a large-equivalent-source window (color-scale map in Figure A4a). This excellent data fit produced by the PEL (color-scale map in Figure A4b) is due to the combination of both the low-degree polynomial and the small-equivalent-source window. This combination allows estimating a smoother magnetization-intensity distribution (Figure A5b) within the equivalent layer as compared with the distribution estimated by setting a large-equivalent-source window (Figure A5a). Histograms of the data misfits shown as insets of Figures A4a and A4b quantifies the poor and acceptable data fits produced by the PEL using large- and small-equivalent-source windows, respectively.

Because the data fitting is acceptable, the estimated magnetization-intensity distribution must be accepted and then the desired transformation of the data can be done. Hence, we used the equivalent layer estimated using the PEL to compute the reduced-to-the-pole anomaly (dashed white lines in Figure A6), which shows a close agreement with the true anomaly at the pole (black lines and gray-scaled map in Figure A6). The histogram of the data misfits (inset of Figure A6) quantifies this agreement. The PEL approach solves a reduced system of equations ( $1875 \times 1875$  system) while the classical equivalent-data approach should solve a large system ( $69,316 \times 69,316$

system). By using Cholesky's decomposition as the algorithm for solving the linear systems, the number of flops required by the classical approach to solve the linear system (equation A17a) is approximately 50,354 times greater than that required by the PEL (equation A18a). The construction of the linear system (equations A17b and A18b) requires approximately 1319 times more flops for the classical approach than for the PEL.

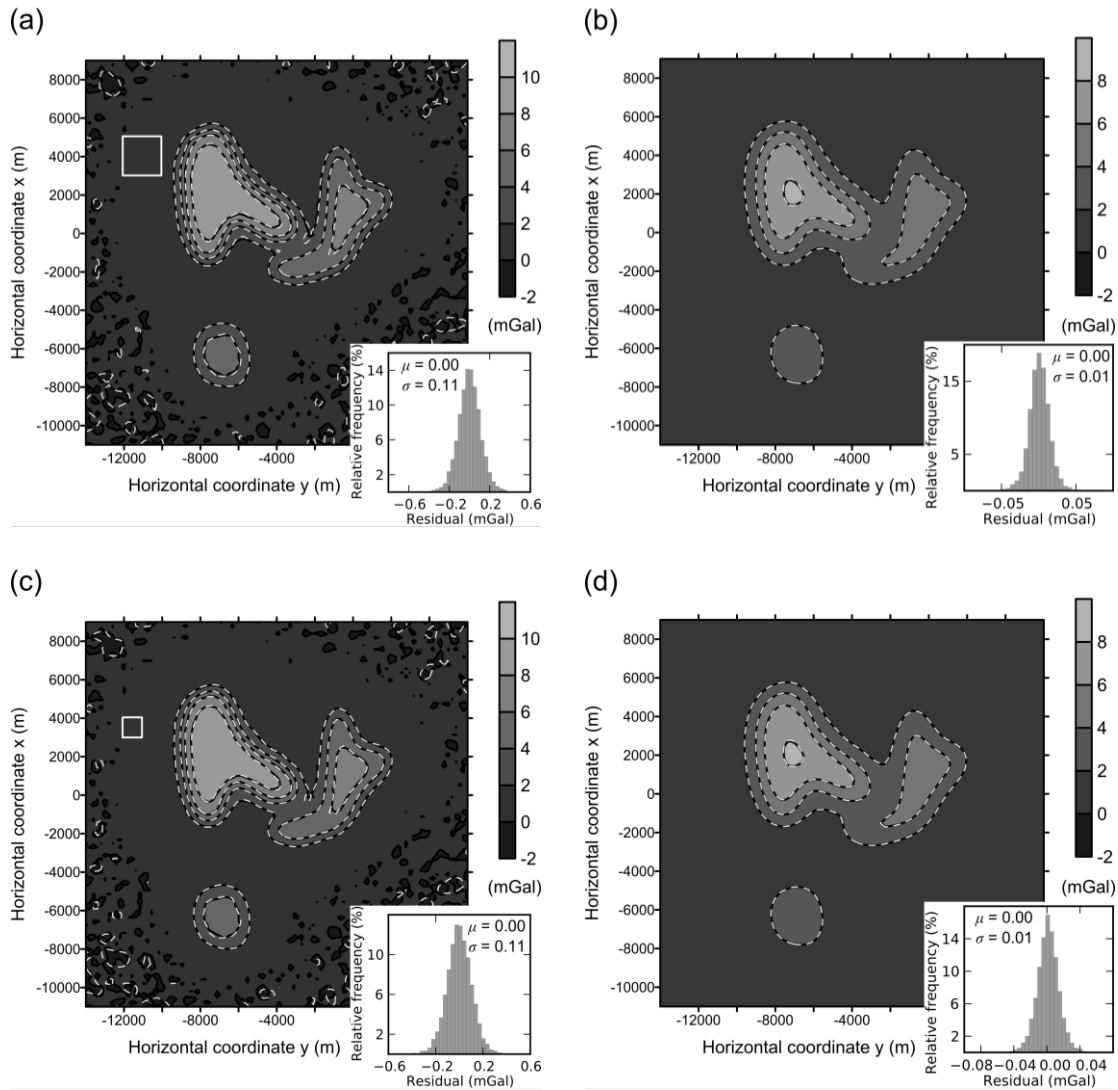


Figure A2 – Tests with synthetic gravity data. (a) Simulated noise-corrupted (black lines and gray-scale map) and predicted (dashed white lines) gravity anomalies at  $z = -150$  m; the latter is obtained by the estimated PEL using large-equivalent-source windows and third-order polynomials ( $\alpha = 3$ ). (b) Simulated noise-free (black lines and gray-scale map) and upward-continued (dashed white lines) anomalies at  $z = -500$  m. The latter is obtained using the PEL estimated from the anomaly shown in a with large-equivalent-source windows and third-order polynomials ( $\alpha = 3$ ). (c) Simulated noise-corrupted (black lines and gray-scale map) and predicted (dashed white lines) gravity anomalies at  $z = -150$  m. The latter is obtained through the PEL estimated using small-equivalent-source windows and first-order polynomials ( $\alpha = 1$ ). (d) Simulated noise-free (black lines and gray-scale map) and upward-continued (dashed white lines) anomalies at  $z = -500$  m. The latter is obtained by using the PEL estimated from the anomaly shown in c with small-equivalent-source windows and first-order polynomials ( $\alpha = 1$ ). The equivalent-source windows used in a-b and c-d are projected, respectively, onto a and c (outlined white rectangles). Histograms of the data misfits are shown as insets in a-d with their corresponding means  $\mu$  and standard deviations  $\sigma$ .

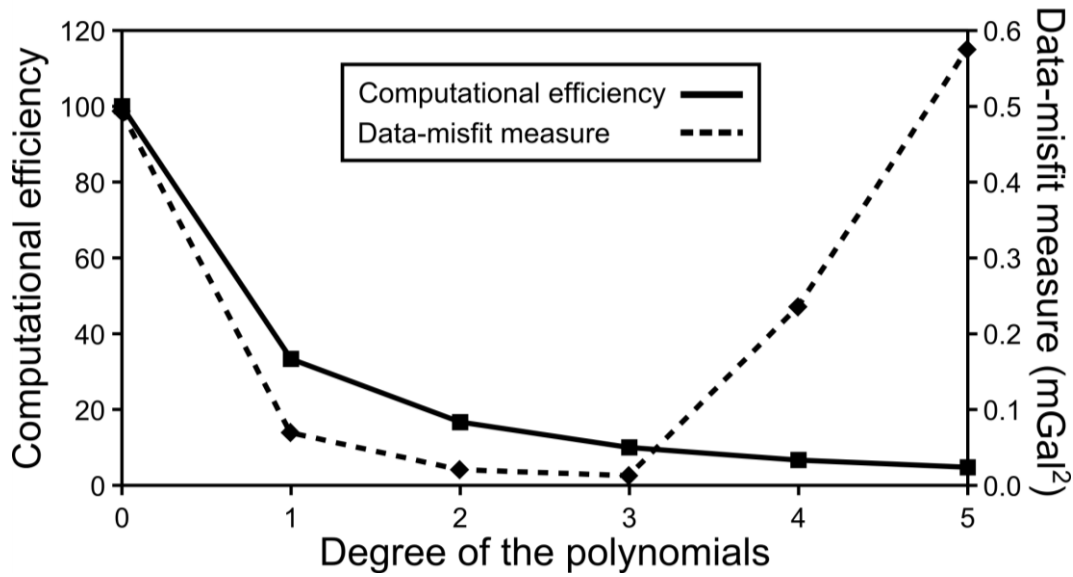


Figure A3 – The trade-off between the data-misfit measure and the computational efficiency of PEL by assigning different degrees  $\alpha$  of the polynomials. The data-misfit measure (dashed line) and the computational efficiency (solid line) of PEL were computed by assuming the same size of the equivalent-source window shown in Figure A2a (white open rectangle).

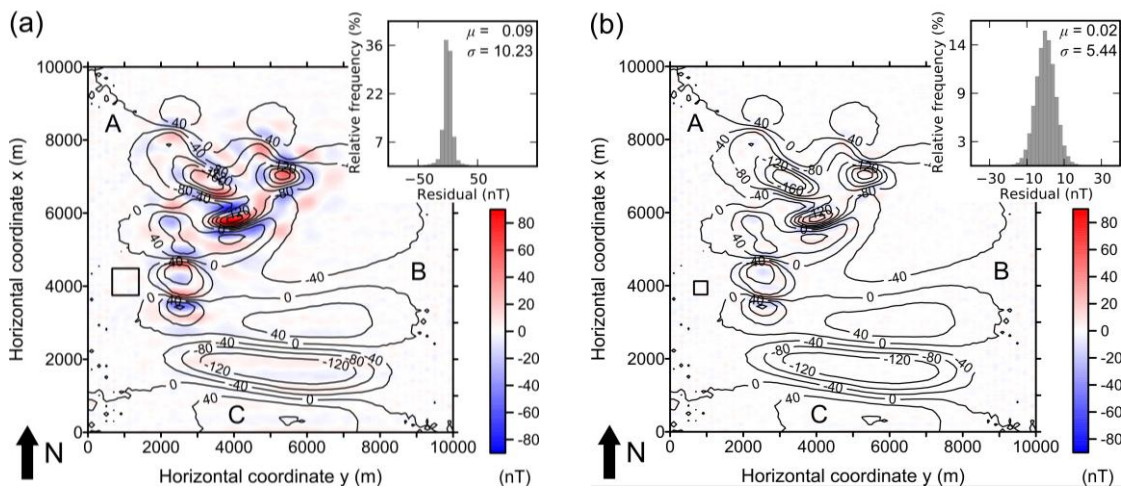


Figure A4 – Tests with synthetic magnetic data. (a) and (b) Simulated noise-corrupted (black lines) total-field anomaly at  $z = -150$  m characterized by short- (region A), mid- (region C), and long- (region B) wavelength spectral contents. The predicted total-field anomalies at  $z = -150$  m (not shown) are obtained by the estimated PEL (shown in Figure A5) using first-order polynomials ( $\alpha = 1$ ) and large (a) and small (b) equivalent-source windows. Color-scale maps in a and b show the differences between the simulated and predicted total-field anomalies. The equivalent-source windows used in a and b are projected onto the data set (outlined black rectangles). Histograms of the data misfits are shown as insets in a and b with their corresponding means  $\mu$  and standard deviations  $\sigma$ .

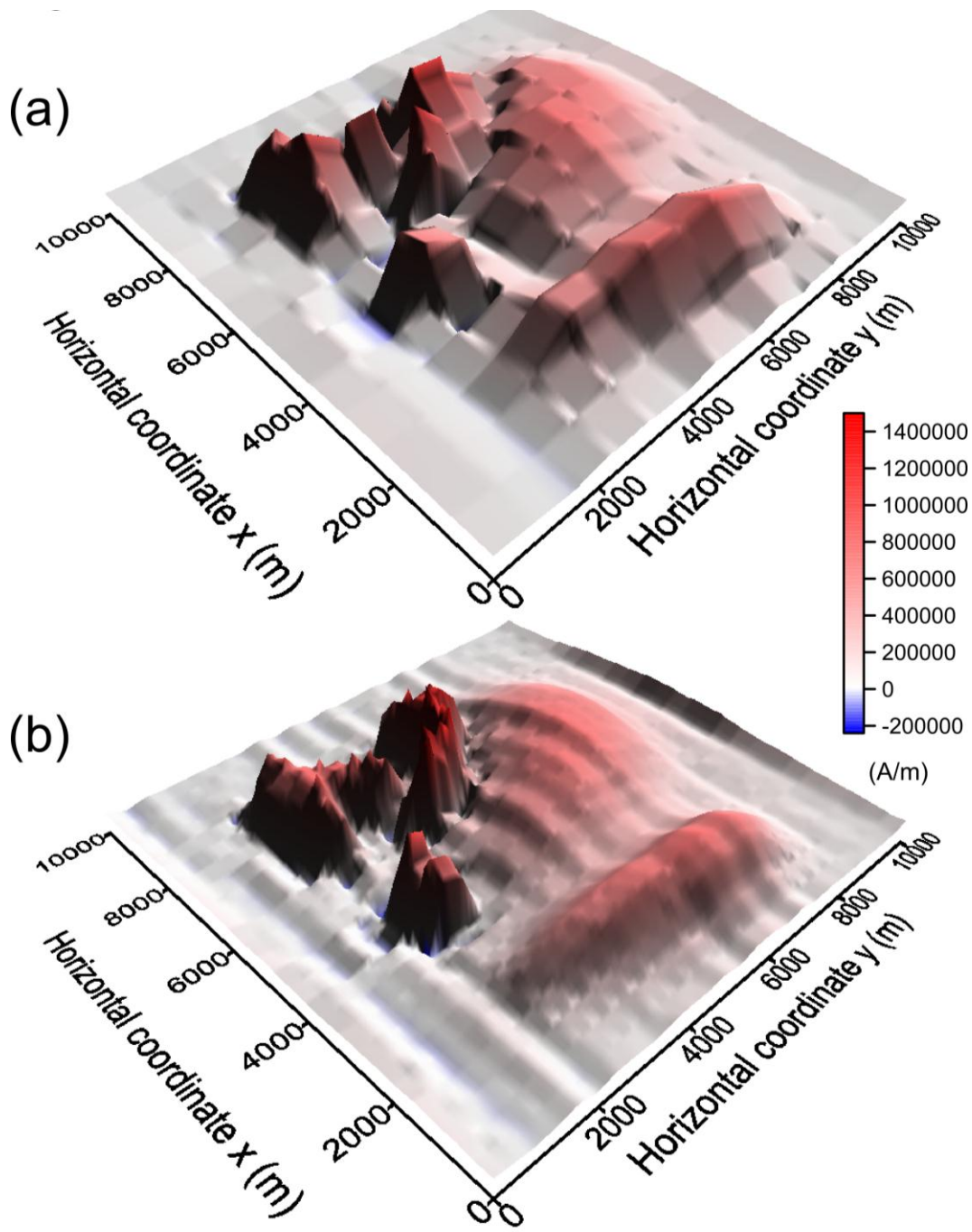


Figure A5 – Tests with synthetic magnetic data. Computed magnetization-intensity distributions obtained by PEL with first-order polynomials ( $\alpha = 1$ ) and large (a) and small (b) equivalent-source windows. The equivalent-source windows used in (a) and (b) are depicted in Figure A4a and 4b, respectively.

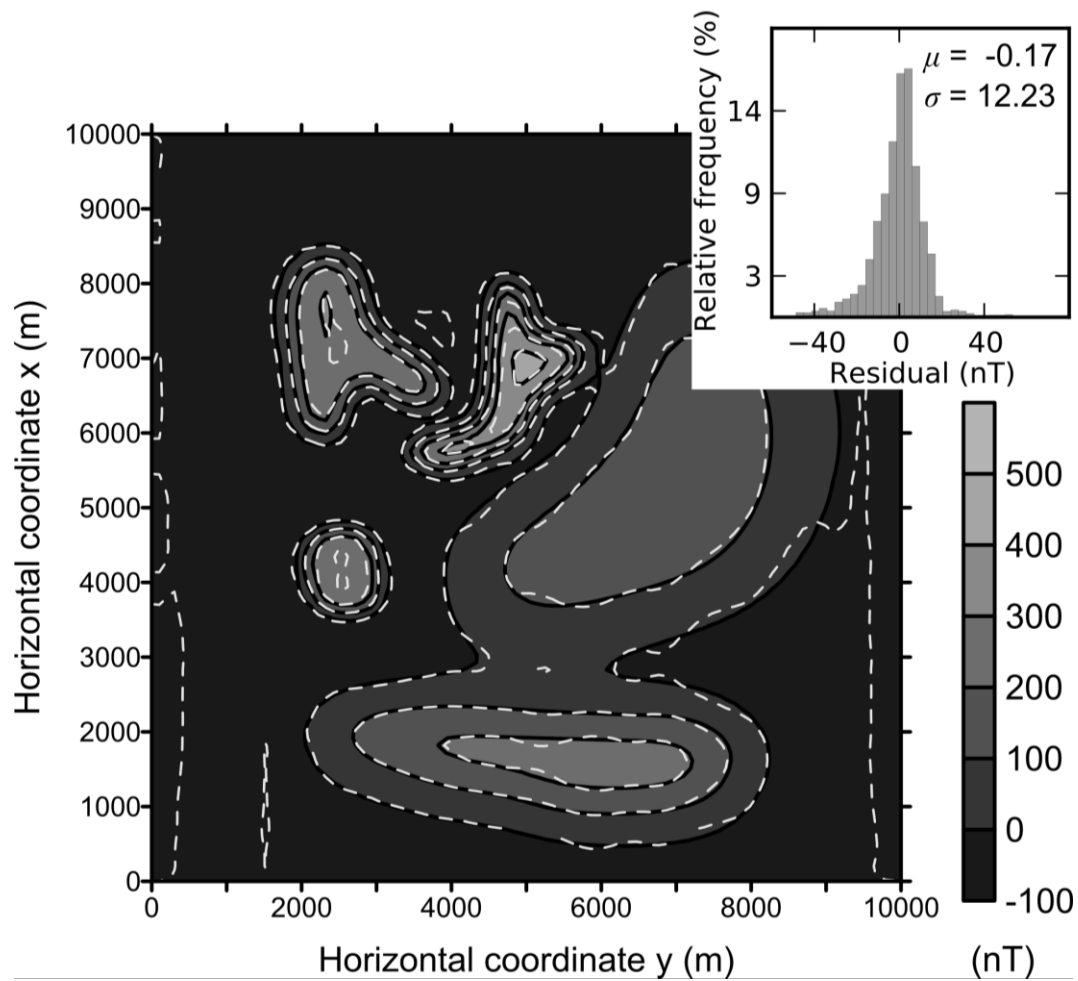


Figure A6 – Test with synthetic magnetic data. Noise-free total-field anomaly at the pole (black lines and gray-scale map) produced by the same set of simulated bodies described in Figure A4 and reduced-to-the-pole anomaly (dashed white lines) predicted by the estimated PEL shown in Figure A5b by using equivalent-source windows shown in Figure A4b. The inset shows the histogram of the residuals between the true noise-free anomaly at the pole and the reduced-to-the-pole anomaly predicted by the PEL with its mean  $\mu$  and standard deviation  $\sigma$ .

## APPLICATION TO REAL DATA

We apply our method (PEL) to process an aeromagnetic data set over the Goiás Magmatic Arc, in central Brazil. This region is mainly made up of metaplutonic rocks exposed between volcano-sedimentary sequences (Pimentel et al., 2000). The aeromagnetic data set covers the southern portion of the Goiás Magmatic Arc at the Arenópolis Arc (Figure A7a) and was acquired at an average vertical coordinate of  $z = -746$  m. The geomagnetic field has  $-19^\circ$  declination and  $-21.5^\circ$  inclination and we assume that the source has a total magnetization vector with  $-19^\circ$  declination and  $-40^\circ$  inclination based on Dutra and Marangoni (2009). The data set used contains  $N = 78,146$  observations. We set up a PEL with  $M = 81,000$  equivalent sources (dipoles) with  $-19^\circ$  declination and  $-40^\circ$  inclination and distributed on a regular grid at constant vertical coordinate  $z_0 = -400$  m. We divide this equivalent layer into  $Q = 810$  equivalent-source windows arranged in a grid of  $27 \times 30$  windows, each one with  $M_s = 100$  dipoles. The area of an equivalent-source window is projected onto the data set being outlined by the white open rectangle in Figure A7a. We used first-order polynomials ( $\alpha = 1$ ) with  $P = 3$  coefficients (equation A7). Therefore, the number of unknown coefficients describing the magnetization intensities of the dipoles is  $H = 2430$ . We set  $\mu_0 = 10^{-15}$  and  $\mu_1 = 10^{-7}$ . Figure A7a shows that the predicted total-field anomaly (dashed white lines) obtained by the PEL fits the observed total-field anomaly (black lines and gray-scale map). The histogram of the data misfit (inset of Figure A7a) resembles a bell-shaped distribution confirming that the measurement errors are normally

distributed with a small standard deviation. Next, we use the estimated PEL to compute the reduction to the pole of the aeromagnetic data at a  $z$  coordinate - 1300 m. Figure A7b shows the observed total-field anomaly upward-continued and reduced to the pole. We verify that our approach performed a meaningful reduction to the pole because the resulting reduced-to-the-pole anomaly (black lines and gray-scale map in Figure A7b) is predominantly positive.

In this test, the PEL is computationally efficient because it deals with a  $2430 \times 2430$  system instead of a  $78,146 \times 78,146$  one. By solving the resulting linear systems through Cholesky's decomposition, the number of flops required by the classical approach (equation A17a) is approximately 33,179 times greater than that required by the PEL (equation A18a). The construction of the linear system (equations A17b and A18b) requires approximately 992 times more flops for the classical approach than for the PEL.

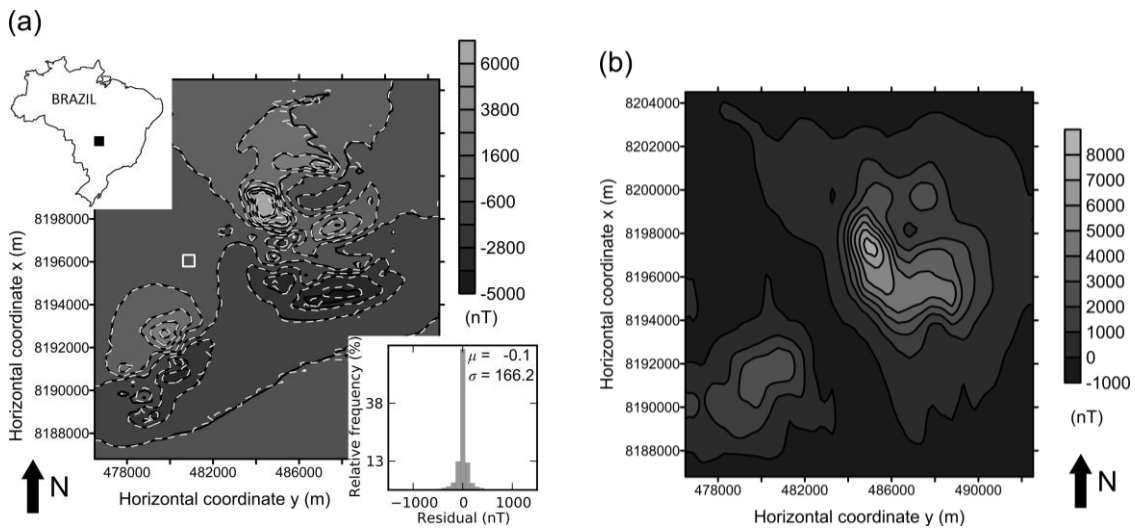


Figure A7 – Real test from Arenópolis Arc (Brazil). (a) Observed (black lines and gray-scale map) and predicted (dashed white lines) total-field anomalies. The latter is obtained by the estimated PEL (not shown). The inset on the right shows the histogram of the data misfit with its mean  $\mu$  and standard deviation  $\sigma$ . The equivalent-source window used are projected onto the data set (outlined white rectangle). The study area (black square) is shown as an inset in the map of Brazil. (b) Transformed data produced by applying the upward continuation and the reduction to the pole via the estimated PEL to the anomaly shown in a.

## CONCLUSIONS

We have presented a new fast method for processing large sets of potential-field data via the equivalent-layer technique. The novelty of our method consists in dividing the equivalent layer into a regular grid of equivalent-source windows, whose physical-property distributions are described by bivariate polynomials. Thus, we assumed that the physical-property distribution within the equivalent layer can be described by a piecewise-polynomial function. After setting the size of equivalent-source window and the degree of the polynomial, our method estimates the polynomial coefficients, for each window, by using a regularized potential-field inversion. Next, the physical-property distribution within an equivalent layer is obtained by means of a transformation which maps the estimated polynomial coefficients into the physical-property distribution. Finally, the transformation of the data is performed by pre-multiplying the determined physical-property distribution by the matrix of Green's functions associated with the desired transformation.

The proposed polynomial representation of the physical-property distribution within the equivalent layer leads to a drastic reduction of the linear system of equations that needs to be solved for estimating this physical-property distribution compared with the classical equivalent-layer technique. This occurs because, in the classical equivalent-layer technique, the inverse problem of estimating the physical-property distribution within the equivalent layer is posed in the data space. In this case the inverse problem leads to a linear system of equations with dimensions based on the number of data,  $N$ . In contrast, the inverse problem of our method leads to a linear system of

equations with dimensions based on the total number of polynomial coefficients within all equivalent-source windows, which is significantly smaller than  $N$ . Conversely, the PEL requires an additional step of converting the estimated coefficients into the physical-property distribution within an equivalent layer. However, this does not imply a meaningful increase of the computational cost. This occurs because the transformation for mapping the estimated polynomial coefficients into the physical-property distribution is a linear function which involves only a sparse matrix-vector multiplication.

Applications to both synthetic and real data sets show that our method produces effective equivalent-source layers for performing any linear transformation of potential-field data without a huge computational load and a long processing time as compared with the classical approach. One might think that the choices of the size of the equivalent-source window and of the degree of the polynomials would be a difficult task. However, a simple criterion that may be used is that the shorter the wavelength components of the potential-field anomaly, the smaller the size of the equivalent-source window and the lower the degree of the polynomial should be. A conservative choice is to use a small equivalent-source window and a low degree polynomial. A simple and effective way to check if the choices of the size of the equivalent-source window and the degree of the polynomial were correctly done consists in verifying if the estimated physical-property distribution via the PEL yields an acceptable data fit. If the data fitting is poor, the estimated physical-property distribution via PEL must be rejected and a smaller size of the equivalent-source window and (or) another degree of the polynomial must be tried. This procedure is repeated until an acceptable data fit is obtained. Thus, a poor fit of the observed data

may be used as a criterion to evaluate the optimum size of the equivalent-source window and the optimum degree of the polynomial.

Further improvements in the methodology of the PEL could be attained by combining the division of the equivalent layer into a non-regular set of equivalent-source windows with the use of different degrees of the polynomials. This improvement could be implemented accordingly to the spectral content of the potential-field anomaly. The number of equivalent-source windows should be greater and the degree of the polynomial function should be lower where the data are characterized by short-wavelength components. Another improvement in the PEL methodology could be accomplished by using a moving-data-window scheme that is shifted over the whole data set. When inverting the observations inside a small data window by using a small equivalent-source located below the data window, only the transformed field near the center of the data window can be computed. Yet another improvement in the PEL methodology could be formulated by setting up an equivalent layer with a continuous distribution of the physical property which varies horizontally according to a piecewise-polynomial function. Hence, the potential-field forward problem could be numerically computed through Gaussian quadrature, for example.

Further computational efficiency of the PEL algorithm might be achieved by using different methods for solving the linear system. Here, we have used Cholesky's decomposition, however other algorithms could be employed such as the preconditioned conjugate gradient method.

Additionally, in the case of full-tensor gradiometry, our method could be used for processing all components together in a joint scheme, since all observations derive from common sources. The application of our polynomial

equivalent layer is extremely fast, making feasible the processing of the large data sets, often encountered in airborne surveys, through the equivalent-layer technique. However, our method fails to provide a significant performance increase when processing a small number of sparsely spaced potential-field observations, as is routinely encountered in localized ground based surveys. The practical implementation of the proposed polynomial equivalent layer is straight forward and does not require supercomputers or data compression algorithms.

## REFERENCES

- Aster, R. C., B. Borchers, and C. H. Thurber, 2004, *Parameter estimation and inverse problems*: Elsevier Academic Press.
- Barnes, G., and J. Lumley, 2011, Processing gravity gradient data: *Geophysics*, **76**, no. 2, 133–147, doi: 10.1190/1.3548548.
- Boyd, S., and L. Vandenberghe, 2004, *Convex optimization*: Cambridge University Press.
- Cordell, L., 1992, A scattered equivalent-source method for interpretation and gridding of potential-field data in three dimensions: *Geophysics*, **57**, 629–636, doi: 10.1190/1.1443275.
- Dampney, C. N. G., 1969, The equivalent source technique: *Geophysics*, **34**, 39–53, doi: 10.1190/1.1439996.
- Dutra, A. C., and Y. R. Marangoni, 2009, Gravity and magnetic 3D inversion of Morro do Engenho complex, Central Brazil: *Journal of South American Earth Sciences*, **28**, 193–203, doi: 10.1016/j.jsames.2009.02.006.
- Emilia, D. A., 1973, Equivalent sources used as an analytic base for processing total magnetic field profiles: *Geophysics*, **38**, 339–348, doi: 10.1190/1.1440344.

Graham, R. L., Knuth, D. E., and O. Patashnik, 1988, *Concrete Mathematics*: Addison-Wesley /publishing Company.

Guspí, F. and I. Novara, 2009, Reduction to the pole and transformations of scattered magnetic data using Newtonian equivalent sources: *Geophysics*, **74**, no. 5, L51–L59, doi: 10.1190/1.3170690.

Hansen, R. O., and Y. Miyazaki, 1984, Continuation of potential fields between arbitrary surfaces: *Geophysics*, **49**, 787–795, doi: 10.1190/1.1441707.

Leão, J. W. D., and J. B. C. Silva, 1989, Discrete linear transformations of potential fields data: *Geophysics*, **54**, 497–507, doi: 10.1190/1.1442676.

Li, Y., and D. W. Oldenburg, 2010, Rapid construction of equivalent sources using wavelets: *Geophysics*, **75**, no. 3, L51–L59, doi: 10.1190/1.3378764.

Mendonça, C. A., and J. B. C. Silva, 1994, The equivalent data concept applied to the interpolation of potential field data: *Geophysics*, **59**, 722–732, doi: 10.1190/1.1443630.

Pimentel, M. M., R. A. Fuck, H. Jost, C. F. Ferreira Filho, and S. M. Araújo, 2000, The basement of the Brasília Fold Belt and the Goiás Magmatic Arc, *in* U. G. Cordani, E. J. Milani, A. Thomaz Filho and D. A. Campos, eds., *Tectonic evolution of South America: 31st International Geological Congress*, 195–230.

Silva, J. B. C., 1986, Reduction to the pole as an inverse problem and its application to low-latitude anomalies: *Geophysics*, **51**, 369–382, doi: 10.1190/1.1442096.

Tikhonov, A. N., and V. Y. Arsenin, 1977, *Solution of ill-posed problems*: Winston & Sons.

Uieda, L. and V. C. F. Barbosa, 2012, Robust 3D gravity gradient inversion by planting anomalous densities: *Geophysics*, **77**, no. 4, G55–G66, doi: 10.1190/GEO2011-0388.1.

## **Parte B**

# **3-D radial gravity gradient inversion**

## SUMMARY

We have developed a non-linear method for inverting gravity-gradient data to estimate the shape of an isolated 3-D geologic body located in subsurface. The method assumes the knowledge about the depth to the top and density contrast of the source. The geologic body is approximated by an interpretation model formed by an ensemble of vertically juxtaposed 3-D right prisms, each one with known thickness and density contrast. All prisms forming the interpretation model have a polygonal horizontal cross-section that approximates a depth slice of the body. Each polygon defining a horizontal cross-section has the same fixed number of vertices, which are equally spaced from  $0^\circ$  to  $360^\circ$  and have their horizontal locations described in polar coordinates referred to an arbitrary origin inside the polygon. Although the number of vertices forming each polygon is known, the horizontal coordinates of these vertices are unknown. To retrieve a set of juxtaposed depth slices of the body and, consequently, its shape, our method estimates the radii of all vertices and the horizontal Cartesian coordinates of all arbitrary origins defining the geometry of all polygons describing the horizontal cross-sections of the prisms forming the interpretation model. To obtain a stable estimate that fits the observed data, we impose constraints on the shape of the estimated body. These constraints are imposed through the well-known zeroth- and first-order Tikhonov regularizations allowing, for example, the estimate of vertical or dipping bodies. Although the proposed inverse method can obtain a stable estimate that fits the observed data, different estimates with different maximum depths can produce equally acceptable data fits. To deal with this ambiguity, we use a criterion based on the relationship between the  $\ell$ -1 norm of the residuals ( $s$ ) and the volume of the estimates ( $v_p$ ) obtained by using interpretation models with different maximum depths. By plotting each  $v_p$  against  $s$ , we construct the  $v_p \times s$  curve. The best estimate is the one producing the minimum of  $s$  and fitting the data. A well-defined minimum of  $s$  indicates that the data have enough resolution to recover the shape of the body entirely. Conversely, if the observed data do not have enough resolution, some estimates with different maximum depths produce, practically, the same

minimum value of  $s$ . In this case, the best estimate among a suite of estimates producing equally data fits is the one fitting the gravity-gradient data and producing the minima of both the source's bottom depth and volume. The histograms of the residuals can be used to quantify systematic errors in the data, allowing a data preprocessing to remove these errors. After removing these errors, we confirmed the ability of our method to recover the source geometry entirely (or its upper part only), if the data have sufficient (or insufficient) resolution. By inverting the data from a survey over the Vinton salt dome (Louisiana, USA) with a density contrast of  $0.55 \text{ g/cm}^3$ , we estimated a massive cap rock whose maximum depth attains  $460 \pm 10 \text{ m}$  and its shallowest portion is elongated in the northeast-southwest direction.

# 1. INTRODUCTION

The vertical component of the gravity field has long been used to retrieve the shape of 3-D (or 2-D) geological sources. Two approaches for the reconstruction of bodies from vertical component of the gravity anomaly have been usually adopted.

The first and most straightforward approach adopts the interactive gravity forward modeling (e.g., Oezsen 2004; Caratori-Tontini *et al.* 2009; Gordon *et al.* 2012). This first approach has been frequently used to interpret multiple anomalous sources with complex shapes and closely separated (either vertically and laterally) from each other by short distances.

The second approach to obtain the shape of anomalous sources is based on linear or non-linear gravity inversion. This approach can be used to directly estimate either the density-contrast distribution or the geometry of the anomalous sources. Many gravity-inversion methods have been developed for estimating density-contrast distribution and some examples are given in Last & Kubik (1983), Guillen & Menichetti (1984), Barbosa & Silva (1994), Li & Oldenburg (1998), Portniaguine & Zhdanov (1999), Bertete-Aguirre *et al.* (2002); Silva & Barbosa (2006), Farquharson (2008), Lelièvre & Oldenburg (2009), Silva Dias *et al.* (2009), Fregoso & Gallardo (2009), Silva Dias *et al.* (2011). In these gravity-inversion methods, the Earth's subsurface is discretized into a grid of cubic cells (2-D or 3-D) and the density-contrast distribution is estimated to retrieve the sources' shapes. Other class of gravity-inversion methods to retrieve the shape of anomalous sources estimates a set of geometric parameters which approximates the anomalous source shape.

Usually, these gravity-inversion methods assume the knowledge about the density contrast and may be grouped into two categories. The first one estimates the depths to the lower (or upper) boundary of a geologic body by assuming the knowledge of the upper (or lower) boundary, while the second category estimates the shape of the boundary surface entirely enclosing a geologic body. Most of gravity-inversion methods in the first category have been developed to produce depth-to-basement estimates. Examples for depth-to-basement estimation include the spectral and non-spectral inversion methods (see Barbosa & Silva 2011 for a complete review). The spectral inversion methods for depth-to-basement estimation use the Parker's (1973) forward method to rapidly compute the potential-field anomaly of an arbitrary interface separating two homogeneous media. By assuming the knowledge about the average depth of the basement, Guspí (1993) followed spectral inversion to successfully obtain the depth-to-basement estimates for a variety of density contrasts. The non-spectral inversion methods for depth-to-basement estimation discretize the sedimentary pack into a regular grid of rectangular prisms with prescribed densities, fixed tops and unknown thicknesses which represent the depths to the basement. Examples of successful inversion of gravity data to estimate basement relief by using non-spectral information are given in Richardson & MacInnes (1989), Barbosa *et al.* (1997, 1999), Martins *et al.* (2010, 2011) and Silva *et al.* (2010). The methods belonging to this category gave rise to plethora of gravity-inversion algorithms. Conversely, the second category, that retrieves the shape of geologic sources by estimating the coordinates of the boundary surface entirely enclosing a geologic body, has led to few gravity-inversion methods (e.g., Silva *et al.* 2000; Moraes & Hansen

2001; Silva & Barbosa 2004; Wildman & Gazonas, 2009; Luo 2010; and Oliveira Jr *et al.* 2011).

Recently, gravity gradient data have been used to interpret 3-D (or 2-D) geological sources. Some interpretation methods using gravity gradient data follow a well-known automatic aeromagnetic interpretation method called Euler deconvolution. These gravity-gradient interpretation methods are suitable to locate the depth and horizontal positions of geologic bodies. Zhang *et al.* (2000) modified the conventional Euler deconvolution method for gravity tensor gradient data. Other examples of gravity-gradient interpretation methods in this direction are based on eigenvectors of the gravity tensor and on Euler deconvolution (e.g., Mikhailov *et al.* 2007; Beiki & Pedersen 2010).

More recently, few gravity-gradient data inversions have been developed not only to locate but also to delineate geological bodies. To date, most of the available gradient-inversion methods estimate a 3-D density-contrast distribution by assuming a piecewise constant function defined on a user-specified grid of cells (e.g., Li 2001; Zhdanov *et al.* 2004; Uieda & Barbosa 2012). Such methods take advantage of the rapid linear optimization problems. However, these methods have the disadvantage of dealing with intractable large-scale 3-D inversion with hundreds of thousands of parameters and tens of thousands of data. This disadvantage requires computational strategies to handle with large amount of computer memory and processing time. Besides, the linear gradient-inversion methods for estimating a 3-D density-contrast distribution demand large amount of prior information about the source; otherwise the inversion produces rough image of the source distribution whose

maximum and minimum estimated values occur at the boundary of the discretized region.

To our knowledge, up to now, only one published method solves a non-linear gravity-gradient data inversion to retrieve the shape of anomalous source by estimating a set of geometric parameters which approximates the anomalous source shape. This non-linear inversion is proposed by Barnes & Barraud (2012) to estimate the upper surface of salt bodies by incorporating the total variation regularization and depth estimates from the interpretation of 2-D seismic. However, there is as yet no non-linear inversion of gravity-gradient data that retrieves the shape of geologic sources by estimating the boundary surface that encloses the geologic body entirely.

This paper follows this latter non-linear inversion of gravity-gradient data that estimates the source's boundary entirely. To the authors' knowledge, this approach for inverting gradient data has never been performed. Specifically, we adopted the same strategy used in Oliveira Jr *et al.* (2011), the so-called Radial inversion. This non-linear inversion of gravity-gradient data eliminates most of the above-mentioned disadvantages of linear inversion methods for estimating a 3-D density-contrast distribution. Like Oliveira Jr *et al.* (2011), we approximate the 3-D source by a set of vertically stacked right prisms whose thicknesses and density contrasts are known and their horizontal cross-sections are described by unknown polygons. The polygon sides of all prisms approximately describe the edges of horizontal depth slices of the 3-D geologic source. By using polar coordinates to describe the polygon vertices of each prism, our method estimates the radii associated with each polygon vertex for a fixed number of equally spaced central angles from  $0^{\circ}$  to  $360^{\circ}$ , and the

horizontal Cartesian coordinates of an arbitrary origin located within the top of the prism. We used a wide variety of regularizing constraints to obtain stable solutions. Here, we generalize the Oliveira Jr *et al.*'s (2011) criterion for determining the optimum depth-to-bottom estimate of the anomalous source which is based on the relationship between the estimated total-anomalous mass and the  $\ell$ -1 norm of the data-misfit. Our criterion is based on the curve between the volume of the estimated source versus the  $\ell$ -1 norm of the data-misfit obtained by using multiple inversions, using different tentative maximum depths for the set of assumed juxtaposed 3-D prisms. Finally, tests on synthetic gravity-gradient data and on field data collected over the Vinton salt dome, southwest Louisiana, USA, confirm the potential of our approach.

## 2. METHODOLOGY

Assume that a 3-D source is confined in the interior of a finite region  $\mathfrak{R}$  (Fig. B1) in the  $x$ - $y$ - $z$  space beneath the earth's surface with its  $x$ -axis pointing north,  $y$ -axis pointing east, and  $z$ -axis pointing down. The 3-D source is either outcropping or buried, but with a known depth to the top  $z_0$ . We also assume a known density contrast between the 3-D source and the host rocks. This density contrast can be constant or variable along the  $z$ -direction. An arbitrary but unknown closed surface  $S$  is assumed to separate the 3-D source from the host rocks. To estimate the surface  $S$ , we approximate the volume of the source (dark grey volume in Fig. B1a) by a set of  $L$  vertically stacked 3-D prisms (light grey prisms, identified by  $P^k, k = 1, \dots, L$ , in Fig B1a). The density contrast within each prism,  $\rho^k, k = 1, \dots, L$ , is assumed constant and known. All prisms have constant and known thicknesses  $dz$ , but their horizontal cross-sections are described by arbitrary and unknown polygons. Notice that the horizontal coordinates of the polygon vertices approximately represent the edges of horizontal depth slices of the 3-D geological source 3-D. The top of the  $k$ th prism  $P^k$  is described by  $M^k$  vertices (white dots in Fig. B1b) with Cartesian coordinates  $(x_j^k, y_j^k, z_1^k), j = 1, \dots, M^k, k = 1, \dots, L$ , where  $z_1^k$  is given by  $z_0 + (k-1)dz, k = 1, \dots, L$ , and where  $z_0$  is a pre-specified depth to the top of the true geologic source which is presumably known by the interpreter. Like Oliveira Jr *et al.* (2011), instead of use Cartesian coordinates, we describe the horizontal location of the vertices of the  $k$ th prism  $P^k$  by using the polar

coordinates  $(r_j^k, \theta_j^k)$ ,  $j = 1, \dots, M^k$ ,  $k = 1, \dots, L$  (white dots in Fig. B1c). The set of polar coordinates describing the vertices of the  $k$ th prism  $P^k$  is referred to an arbitrary origin  $O^k$  (grey dot in Fig. B1c), whose horizontal Cartesian coordinates are given by  $(x_0^k, y_0^k)$ ,  $k = 1, \dots, L$ . We assume a fixed number of vertices  $M^k$ ,  $k = 1, \dots, L$ , for each prism based on the interpreter's knowledge about the complexity of true source (dark grey volume in Fig. B1a). Additionally, we establish that the vertices are equally spaced from  $0^\circ$  to  $360^\circ$ . Thus, given the number of vertices  $M^k$ , the set of angular coordinates describing the vertices of the  $k$ th prism  $P^k$  is automatically obtained by

$$\theta_j^k = (j-1)\Delta\theta^k, \quad j = 1, \dots, M^k, \quad (\text{B1})$$

where  $\Delta\theta^k = \frac{2\pi}{M^k}$ ,  $k = 1, \dots, L$ .

Like Oliveira Jr *et al.* (2011), our inversion method retrieves the shape of a 3-D source by estimating the horizontal Cartesian coordinates  $(x_0^k, y_0^k)$  of all unknown origins  $O^k$ ,  $k = 1, \dots, L$ , and the radii  $r_j^k$ ,  $j = 1, \dots, M^k$ ,  $k = 1, \dots, L$ , of the vertices describing all prisms forming the interpretation model. In contrast with Oliveira Jr *et al.* (2011), our approach inverts gravity gradient data set.

These horizontal Cartesian coordinates  $(x_0^k, y_0^k)$  and radii  $r_j^k$  are arranged in the  $M$ -dimensional parameter vector  $\mathbf{m}$ , which will be estimated from the observed gravity gradient data set. The number  $M$  of unknown parameters is given by  $M = 2L + \sum_{k=1}^L M^k$ . For convenience, the parameter vector is partitioned as

$$\mathbf{m} = [\mathbf{m}^{1T} \quad \dots \quad \mathbf{m}^{kT} \quad \dots \quad \mathbf{m}^{LT}]^T, \quad (\text{B2})$$

where the superscript  $T$  stands for a transpose, and  $\mathbf{m}^k$  is the  $(M^k + 2) \times 1$  vector given by

$$\mathbf{m}^k = [\mathbf{r}^{kT} \quad x_0^k \quad y_0^k]^T, \quad k = 1, \dots, L, \quad (\text{B3})$$

where  $\mathbf{r}^k = [r_1^k \quad \dots \quad r_{M^k}^k]^T$  is the  $M^k$ -dimensional vector containing the radii of the  $M^k$  vertices of the  $k$ th prism  $P^k$ .

Let  $\mathbf{g}^{\alpha\beta}$  be an  $N^{\alpha\beta}$ -dimensional vector whose  $i$ th element  $g_i^{\alpha\beta}$  is the  $\alpha\beta$ -component of the gravity gradient tensor measured at the  $i$ th observation point  $(x_i, y_i, z_i)$ , where  $\alpha$  and  $\beta$  belong to the set of  $x$ -,  $y$ -, and  $z$ -directions of a right-sided Cartesian coordinate system (Fig. B1). This observed data  $g_i^{\alpha\beta}$  can be approximated by the sum of the effect predicted by the  $L$  vertically stacked 3-D prisms (light grey prisms in Fig B1a) setting up the interpretation model, i.e.:

$$d_i^{\alpha\beta} \equiv \sum_{k=1}^L f_i^{\alpha\beta}(\mathbf{r}^k, x_0^k, y_0^k, \boldsymbol{\theta}^k, \rho^k), \quad i = 1, \dots, N^{\alpha\beta}, \quad (\text{B4})$$

where  $\boldsymbol{\theta}^k$  is the  $M^k$ -dimensional vector whose  $j$ th element is given in eq. B(1).

The nonlinear function  $f_i^{\alpha\beta}(\mathbf{r}^k, x_0^k, y_0^k, \boldsymbol{\theta}^k, \rho^k)$  represents the predicted  $\alpha\beta$ -component of the gravity gradient tensor, computed at the  $i$ th observation point  $(x_i, y_i, z_i)$ , produced by the  $k$ th prism  $P^k$  (Fig. B1c), which has the depth to the top  $z_1^k$ , the thickness  $dz$ , the density contrast  $\rho^k$ , and whose polygonal cross-section is described by the variables  $\mathbf{r}^k$ ,  $\boldsymbol{\theta}^k$ ,  $x_0^k$  and  $y_0^k$ . The  $i$ th nonlinear function  $f_i^{\alpha\beta}(\mathbf{r}^k, x_0^k, y_0^k, \boldsymbol{\theta}^k, \rho^k)$ ,  $i = 1, \dots, N^{\alpha\beta}$ , is the product between the gravitational constant, the density  $\rho^k$ , and a volume integral that has a closed form given by Plouff (1976, equation 9).

Let  $\psi^{\alpha\beta}(\mathbf{m})$  be the data-misfit function which measures the squared  $\ell_2$ -norm of the difference between the observed and predicted  $\alpha\beta$ -component of the gravity gradient tensor, i.e.,

$$\psi^{\alpha\beta}(\mathbf{m}) = w^{\alpha\beta} \|\mathbf{d}^{\alpha\beta} - \mathbf{g}^{\alpha\beta}\|_2^2, \quad (\text{B5})$$

where  $\mathbf{d}^{\alpha\beta}$  is the  $N^{\alpha\beta}$ -dimensional vector whose  $i$ th element  $d_i^{\alpha\beta}$  is given by eq. B(4) and  $w^{\alpha\beta}$  is a normalizing factor defined as

$$w^{\alpha\beta} = \frac{\sqrt{N^{\alpha\beta}}}{\|\mathbf{g}^{\alpha\beta}\|_2}. \quad (\text{B6})$$

The total data-misfit function  $\Psi(\mathbf{m})$  is defined as the sum of the individual data-misfit functions for each one of the  $\alpha\beta$ -components of the gravity tensor, i.e.,

$$\Psi(\mathbf{m}) = \psi^{xx}(\mathbf{m}) + \psi^{xy}(\mathbf{m}) + \psi^{xz}(\mathbf{m}) + \psi^{yy}(\mathbf{m}) + \psi^{yz}(\mathbf{m}) + \psi^{zz}(\mathbf{m}). \quad (\text{B7})$$

The data-misfit function given in eq. B(7) holds when the six components of the gravity-gradient tensor are considered. If some component is not considered, the practical procedure is to set up the respective normalizing factor (eq. B6) as zero. For example, if the  $xy$ - and the  $yy$ - components are not considered, the interpreter must assign null values to the normalizing factors  $w^{xy}$  and  $w^{yy}$  (eq. B6).

The nonlinear inverse problem of estimating the parameter vector  $\mathbf{m}$  that minimizes the total data-misfit function  $\Psi(\mathbf{m})$  (eq. B7) is an ill-posed problem because the solution is neither unique nor stable. To transform this problem into a well-posed problem, we formulate a constrained nonlinear inversion to obtain a 3-D shape of a geologic body by minimizing

$$\Gamma(\mathbf{m}) = \Psi(\mathbf{m}) + \mu \sum_{\ell=1}^{LC} \phi^{\ell}(\mathbf{m}), \quad (\text{B8a})$$

subject to

$$m_{\min_j} < m_j < m_{\max_j}, \quad j = 1, \dots, M. \quad (\text{B8b})$$

In eq. B8a,  $\mu$  is the regularizing parameter. In the inequality constraints (eq. B8b), the  $m_{\min_j}$  and  $m_{\max_j}$  are expressing the lower and upper bounds, respectively, to the  $j$ th element  $m_j$  of the parameter vector  $\mathbf{m}$ . These bounds  $m_{\min_j}$  and  $m_{\max_j}$ , both on the radii of all vertices of all prisms ( $r_j^k$ ,  $j = 1, \dots, M^k$ ,  $k = 1, \dots, L$ ) and on the horizontal Cartesian coordinates of all arbitrary origins ( $x_0^k$ ,  $y_0^k$ ,  $k = 1, \dots, L$ ) are defined element by element by the interpreter based on either the horizontal extent of the gravity gradient data or the geological knowledge about the studied area. In eq. B(8a),  $\phi^\ell(\mathbf{m})$  is the  $\ell$ th constraining function in a set of  $LC$  constraining functions that were proposed by Oliveira Jr *et al.* (2011). All these constraining functions (from now on named constraints) are defined on parameter space. The chosen constraints for our method are:

- Constraint 1 -  $\phi^1(\mathbf{m})$ :

Smoothness constraint on the adjacent radii defining the horizontal section of each prism. Mathematically, this constraint represents the first-order Tikhonov regularization (Tikhonov & Arsenin, 1977) on the radii within a prism of the interpretation model. This constraint imposes that each horizontal cross-section of the estimated 3-D source must be approximately circular.

- Constraint 2 -  $\phi^2(\mathbf{m})$ :

Smoothness constraint on the adjacent radii of the vertically adjacent prisms. Mathematically, this constraint represents the first-order Tikhonov regularization

on the radii of vertically adjacent prisms of the interpretation model. This constraint imposes that the horizontal cross-section of the estimated 3-D source must have an approximately constant form along the vertical direction 3-D.

- Constraint 3 -  $\phi^3(\mathbf{m})$ :

Source's outcrop constraint. By assuming an outcropping source, this constraint incorporates prior knowledge about the outcropping source's boundaries separating the geological body from the host rock. This constraint imposes that the estimated boundary of the shallowest prism of the interpretation model must be as close as possible to the known boundary of the outcropping body.

- Constraint 4 -  $\phi^4(\mathbf{m})$ :

Source's horizontal location constraint. By assuming an outcropping source, this constraint imposes that the estimated horizontal Cartesian coordinates of the arbitrary origin within the shallowest prism of the interpretation model must be as close as possible to the known horizontal Cartesian coordinates of a point on the outcropping body.

- Constraint 5 -  $\phi^5(\mathbf{m})$ :

Smoothness constraint on the horizontal positions of the arbitrary origins of the vertically adjacent prisms. Mathematically, this constraint represents the first-order Tikhonov regularization on the horizontal Cartesian coordinates of the arbitrary origins of the vertically adjacent prisms of the interpretation model. This constraint imposes a smooth horizontal displacement between vertically adjacent prisms, forcing the estimated 3-D source to be vertical.

- Constraint 6 -  $\phi^6(\mathbf{m})$ :

Minimum Euclidean norm constraint on the radii defining the horizontal cross-section of each prism. Mathematically, this constraint represents the zeroth-order Tikhonov regularization (Tikhonov & Arsenin, 1977) on the all radii forming the interpretation model. This constraint imposes that all estimated radii within each prism must be close to null values.

Estimating the vector  $\hat{\mathbf{m}}$  (the caret denotes estimate) by solving the constrained nonlinear inverse problem defined in eq. B(8) is accomplished by Marquardt's (1963) method, incorporating the Gauss-Newton approximation of the Hessian matrix at each iteration. This algorithm is fully described in Silva *et al.* (2001) and Silva Dias *et al.* (2007). Finally, the inequality constraints (eq. B8b) are introduced through a homeomorphic transformation (Barbosa *et al.* 1999).

To obtain a stable solution which retrieves the shape of geological source, we adopted the same practical procedure described in Oliveira Jr *et al.* (2011). It follows that we obtain a set of  $Q$  estimates  $\hat{\mathbf{m}}_1, \dots, \hat{\mathbf{m}}_Q$ , each one estimated by inverting gravity gradient observations corrupted with different Gaussian pseudorandom noise sequences with zero mean and a specified standard deviation. Then, we compute the sample mean vector  $\tilde{\mathbf{m}}$  and the sample standard deviation vector  $\tilde{\boldsymbol{\sigma}}$ . Here,  $\tilde{\mathbf{m}}$  is an  $M \times 1$  vector whose  $i$ th element  $\tilde{m}_i$ ,  $i=1, \dots, M$ , is the sample mean of a set of  $Q$  estimates of the  $i$ th elements of  $\hat{\mathbf{m}}_k$ ,  $k=1, \dots, Q$ , and  $\tilde{\boldsymbol{\sigma}}$  is an  $M \times 1$  vector whose  $i$ th element  $\tilde{\sigma}_i$ ,  $i=1, \dots, M$ , is the sample standard deviation of a set  $Q$  estimates of the  $i$ th elements of  $\hat{\mathbf{m}}_k$ ,  $k=1, \dots, Q$ . The sample mean vector  $\tilde{\mathbf{m}}$  is assumed to be a

stable solution of the source shape (parameter vector  $\mathbf{m}$ ) if all sample standard deviations ( $\tilde{\sigma}_i, i=1, \dots, M$ ) are smaller than 4 percent (checar) of its corresponding sample mean ( $\tilde{m}_i, i=1, \dots, M$ ).

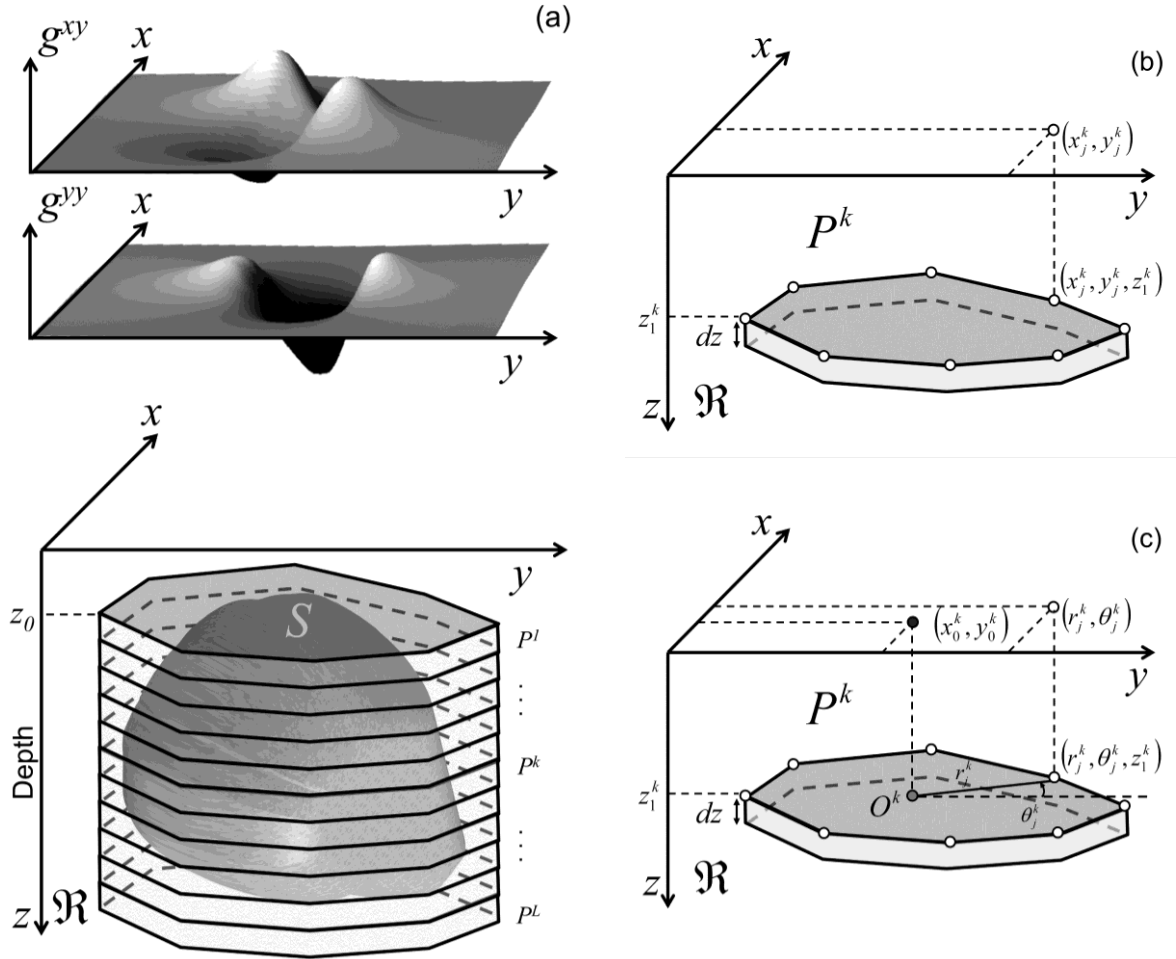


**Figure B1.** Schematic representation of the interpretation model. (a) Observed  $g^{xy}$  and  $g^{yy}$  components of the gravity gradient tensor (grey scale maps) produced by the 3-D source (dark grey volume) limited by the closed surface  $S$ . The interpretation model is formed by  $L$  juxtaposed prisms  $P^k$ ,  $k=1, \dots, L$ , (light grey). (b) Polygonal cross-section of the  $k$ th prism  $P^k$  with thickness  $dz$  and being described by  $M^k$  vertices (white dots) with the Cartesian coordinates  $(x_j^k, y_j^k, z_1^k)$ ,  $j=1, \dots, M^k$ ,  $k=1, \dots, L$ . (c) Representation of the  $M^k$  vertices forming the polygonal cross-section of the  $k$ th prism  $P^k$  by polar coordinates  $(r_j^k, \theta_j^k)$ ,  $j=1, \dots, M^k$ ,  $k=1, \dots, L$  (white dots), referred to an arbitrary origin  $O^k$  (grey dot) with horizontal Cartesian coordinates  $x_0^k$  and  $y_0^k$  (black dot).

### 3. CRITERION FOR ESTIMATING THE TRUE (OR MINIMUM) DEPTH TO THE BOTTOM OF THE SOURCE

In section 2, we established an interpretative model formed by an ensemble of  $L$  prisms (Fig. B1a), with a constant and known thickness  $dz$ . The shallowest prism has the depth to the top equal to  $z_0$ , that presumably coincides with the top of the true geologic source. These variables ( $L$ ,  $dz$  and  $z_0$ ) define the maximum depth to the bottom  $z_{\max}$  of the estimated body by:

$$z_{\max} = z_0 + (L \cdot dz). \quad (\text{B9})$$

After setting up the interpretation model, our method obtains a stable estimate  $\tilde{\mathbf{m}}$  of the 3-D shape of the source by applying the practical procedure described in the section 2. For a fixed maximum depth to the bottom of the interpretation model  $z_{\max}$ , we obtain a stable estimate  $\tilde{\mathbf{m}}$  that fits the data. However, by assigning different depths  $z_{\max}$  to the bottom for the interpretation model, the method produces different stable estimates  $\tilde{\mathbf{m}}$  that fit the data as well. To overcome this dependence of the estimate on the correct choice of the maximum bottom depth  $z_{\max}$ , we developed a new criterion for estimating an *optimum* maximum depth to the bottom of the interpretation model. This *optimum* maximum depth can be the true depth to the bottom of the source if (and only if) the observed gravity gradient data have enough in-depth resolution to reconstruct the source. If not, the developed new criterion estimates the minimum depth to the bottom needed for the interpretation model to produce an acceptable data fit. This new criterion generalizes the criterion developed by Oliveira Jr *et al.* (2011) to determine a *optimum* maximum depth

to the bottom of the source. Here, this new criterion is based on the relationship between the volume  $v_p$  of the estimated source (predicted volume) and the  $\ell_1$ -norm  $s$  of the residuals between the observed and predicted gravity gradient data.

### 3.1. Relationship between the predicted volume $v_p$ and the $\ell_1$ -norm $s$ of the residuals

In this sub-section we present the theoretical relationship between the volume  $v_p$  of an estimate (predicted volume) and the  $\ell_1$ -norm  $s$  of the residuals between the observed and the predicted data. First, let  $g_i^{\alpha\beta}$ ,  $\alpha\beta = xx, xy, xz, yy, yz, zz$ , be the  $\alpha\beta$ -component of the gravity tensor field measured at the  $i$ th observation point  $(x_i, y_i, z_i)$ . Consider that  $g_i^{\alpha\beta}$  is produced by a 3-D geologic source located at subsurface, with constant density contrast  $\rho$  and defined by a volume  $v_0$  (continuous black line in Fig. B2). Let's suppose that this geologic source is approximated by an estimated homogeneous source with the same constant density contrast  $\rho$  and with a predicted volume  $v_p$  (dashed black line in Fig. B2). This approximation of the true geologic source produces, at the same  $i$ th observation point, a predicted component of the gravity tensor  $d_i^{\alpha\beta}(v_p)$ ,  $\alpha\beta = xx, xy, xz, yy, yz, zz$ , that can be described by

$$d_i^{\alpha\beta}(v_p) = \rho \iiint_{v_p} G^{\alpha\beta}(\xi_i, \xi') dv, \quad (\text{B10})$$

where  $G^{\alpha\beta}(\xi_i, \xi')$ ,  $\alpha\beta = xx, xy, xz, yy, yz, zz$ , is the Green's function associated with the  $\alpha\beta$ -component of the gravity tensor,  $\xi_i$  is the position vector of the  $i$ th

observation point and the integration is conducted with respect to the variable  $\xi'$  denoting the position vector of an elementary volume inside  $v_p$ . By assuming that  $g_i^{\alpha\beta} = d_i^{\alpha\beta}(v_0)$  and  $v_p = v_0 + \Delta v$ , where  $\Delta v$  is a small enough volume, then the predicted data  $d_i^{\alpha\beta}(v_p)$  can be considered as an approximation of the observed data  $g_i^{\alpha\beta}$ . This approximation can be represented by a Taylor's expansion of first order about  $v_0$ , leading to

$$\Delta d_i^{\alpha\beta} \approx \frac{d}{dv} d_i^{\alpha\beta}(v_0) \cdot (v_p - v_0), \quad (\text{B11})$$

where  $\Delta d_i^{\alpha\beta} = d_i^{\alpha\beta}(v_p) - g_i^{\alpha\beta}$  and  $\frac{d}{dv} d_i^{\alpha\beta}(v_0)$  is the first-order derivative of the  $\alpha\beta$ -component of the gravity tensor evaluated at  $v_0$ . Eq. B(11) shows that the linear relationship between  $\Delta d_i^{\alpha\beta}$  and  $v_p$ , calculated at a fixed observation point  $(x_i, y_i, z_i)$ , depends on the derivative  $\frac{d}{dv} d_i^{\alpha\beta}(v_0)$ . If  $\frac{d}{dv} d_i^{\alpha\beta}(v_0)$  is positive, the linear relationship between  $\Delta d_i^{\alpha\beta}$  and  $v_p$  has a positive angular coefficient. If  $\frac{d}{dv} d_i^{\alpha\beta}(v_0)$  is negative, the linear relationship between  $\Delta d_i^{\alpha\beta}$  and  $v_p$  has a negative angular coefficient. The relationship between  $\Delta d_i^{\alpha\beta}$  and  $v_p$  can be illustrated by using the 2-D sketches shown in Fig. B3. In Fig. B3(a), the predicted data set (dashed lines) represents a situation in which the predicted volume  $v_p$  is smaller than the true volume  $v_0$ . In opposition, the predicted data set shown in Fig. B3(b) (dashed lines) represents a situation in which the predicted volume  $v_p$  is greater than the true volume  $v_0$ . The Fig. B3(c) exemplifies the linear relationship between  $\Delta d_i^{\alpha\beta}$  and  $v_p$  calculated at the position  $I$  of the 2-D sketches shown in Figs. B3(a) and (b). Similarly, the Fig. B3(d) exemplifies the linear relationship between  $\Delta d_i^{\alpha\beta}$  and  $v_p$  calculated at the

position  $II$  of the 2-D sketches shown in Figs. B3(a) and (b). In Figs. B3(c) and (d), the region A represents the situation illustrated in Fig. B3(a), where the volume  $v_p$  is smaller than the true volume  $v_0$ . Conversely, the region B represents the situation illustrated in Fig. B3(b), where the volume  $v_p$  is greater than the true volume  $v_0$ . This dependence of the signal of the angular coefficient of the linear relationship between  $v_p$  and  $\Delta d_i^{\alpha\beta}$ , calculated at the  $i$ th observation point  $(x_i, y_i, z_i)$ , disappears if we plot the predicted volume  $v_p$  against  $|\Delta d_i^{\alpha\beta}|$  (instead of  $\Delta d_i^{\alpha\beta}$ ). The resulting curve shows a symmetric “<” shape whose minimum  $|\Delta d_i^{\alpha\beta}|$  occurs when the predicted volume  $v_p$  is equal to the true volume  $v_0$  (Fig. B3e). This can be shown by calculating the absolute value of  $\Delta d_i^{\alpha\beta}$  and substituting it into eq. B(11). The resulting equation is given by

$$v_p \approx v_0 + \beta_i^{\alpha\beta} \cdot |\Delta d_i^{\alpha\beta}|, \text{ for } v_p > v_0 \quad (\text{B12a})$$

or

$$v_p \approx v_0 - \beta_i^{\alpha\beta} \cdot |\Delta d_i^{\alpha\beta}|, \text{ for } v_p < v_0, \quad (\text{B12b})$$

where  $\beta_i^{\alpha\beta} = \left| \frac{d}{dv} d_i^{\alpha\beta}(v_0) \right|^{-1}$ . Eqs. B12(a) and B12(b) show, respectively, two straight lines with positive and negative angular coefficients. These lines intercept each other at  $|\Delta d_i^{\alpha\beta}| = 0$  and  $v_p = v_0$  (Fig. B3e).

If we calculate the  $v_p \times |\Delta d_i^{\alpha\beta}|$  curve (eqs. B12a and B12b) for each observation point  $(x_i, y_i, z_i)$ ,  $i = 1, \dots, N$ , and stack them, the resulting curve still shows the symmetric “<” shape. This stack is equivalent to plot the predicted volume  $v_p$  against the  $\ell_1$ -norm  $s^{\alpha\beta}$  of the residuals between the predicted data

$d_i^{\alpha\beta}(v_p)$  and the observed gravity gradient data  $g_i^{\alpha\beta}$ ,  $i=1,\dots,N$ . This norm is given by

$$s^{\alpha\beta} = \frac{1}{N} \sum_{i=1}^N |\Delta d_i^{\alpha\beta}|. \quad (\text{B13})$$

By substituting the  $\ell_1$ -norm  $s^{\alpha\beta}$  into eq. B(11) we obtain

$$v_p \approx v_0 + \hat{\beta}^{\alpha\beta} \cdot s^{\alpha\beta}, \text{ for } v_p > v_0 \quad (\text{B14a})$$

or

$$v_p \approx v_0 - \hat{\beta}^{\alpha\beta} \cdot s^{\alpha\beta}, \text{ for } v_p < v_0, \quad (\text{B14b})$$

where

$$\hat{\beta}^{\alpha\beta} = \left[ \frac{1}{N} \sum_{i=1}^N \left| \frac{d}{dv} d_i^{\alpha\beta}(v_0) \right| \right]^{-1}, \quad (\text{B14c})$$

and  $\alpha\beta = xx, xy, xz, yy, yz, zz$ . Eqs. B14(a) and B14(b) represent two straight lines with, respectively, positive and negative angular coefficients. These lines intercept each other at  $s^{\alpha\beta} = 0$ , where  $v_p = v_0$ . In comparison with the  $v_p \times |\Delta d_i^{\alpha\beta}|$  curve (eqs. B12a and B12b), which is calculated at a fixed observation point  $(x_i, y_i, z_i)$ , the two straight lines forming the  $v_p \times s^{\alpha\beta}$  curve (eqs. B14a and B14b) have different angular coefficients, however the minimum  $s^{\alpha\beta}$  still occurs when the predicted volume  $v_p$  is equal to the true volume  $v_0$  (Fig. B3f). By combining all components of the gravity tensor, we define a new  $\ell_1$ -norm of the residuals between the observed and predicted gravity gradient data given by

$$s = w^{xx} s^{xx} + w^{xy} s^{xy} + w^{xz} s^{xz} + w^{yy} s^{yy} + w^{yz} s^{yz} + w^{zz} s^{zz}, \quad (\text{B15})$$

where  $w^{\alpha\beta}$ ,  $\alpha\beta = xx, xy, xz, yy, yz, zz$ , is given by eq. B(6). Subsequently, by substituting the  $\ell_1$ -norm of the residuals  $s$  into the Taylor's expansion given in eq. B(11), we obtain

$$v_p \approx v_0 + \hat{\beta} \cdot s, \text{ for } v_p > v_0 \quad (\text{B16a})$$

or

$$v_p \approx v_0 - \hat{\beta} \cdot s, \text{ for } v_p < v_0, \quad (\text{B16b})$$

where

$$\hat{\beta} = \left[ \frac{w^{xx}}{\hat{\beta}^{xx}} + \frac{w^{xy}}{\hat{\beta}^{xy}} + \frac{w^{xz}}{\hat{\beta}^{xz}} + \frac{w^{yy}}{\hat{\beta}^{yy}} + \frac{w^{yz}}{\hat{\beta}^{yz}} + \frac{w^{zz}}{\hat{\beta}^{zz}} \right]^{-1}, \quad (\text{B16c})$$

and the angular coefficients  $\hat{\beta}^{\alpha\beta}$ ,  $\alpha\beta = xx, xy, xz, yy, yz, zz$ , are given by eq. B(14c). As pointed out before in section 2, if the interpreter does not use all components of the gravity tensor, he must set the corresponding scale factor  $w^{\alpha\beta}$ ,  $\alpha\beta = xx, xy, xz, yy, yz, zz$ , as zero. In comparison with the  $v_p \times |\Delta d_i^{\alpha\beta}|$  curve (eqs. B12a and B12b and Fig. B3e) and the  $v_p \times s^{\alpha\beta}$  curve (eqs. B14a and B14b), the two straight lines forming the  $v_p \times s$  curve (eqs. B16a and B16b) have different angular coefficients, however the minimum  $s$  still occurs when the predicted volume  $v_p$  is equal to the volume  $v_0$ . The  $v_p \times s$  curve is schematically illustrated in Fig. B3(f).

In the next section we present the relationship between the  $v_p \times s$  curve (eqs. B16a and B16b) and the depth to the bottom  $z_{\max}$  (eq. B9) of the interpretation model. In addition, we provide the practical procedure for construct an estimated  $v_p \times s$  curve.

### 3.2. Relationship between the $v_p \times s$ curve and the depth to the bottom $z_{\max}$ of the interpretation model and practical procedure for constructing the estimated $v_p \times s$ curve

Let's assume that the gravity tensor anomaly is caused by an isolated body with a constant density contrast with the host rocks and having a known depth to the top. In this case, we can expect that, when  $z_{\max}$  approximates the true depth to the bottom of the source, the predicted volume  $v_p$  approximates the true volume  $v_0$  and then the predicted gravity tensor data fits the observed gravity tensor data. In this situation, a minimum value of the  $\ell_1$ -norm of the residuals  $s$  (eq. B15) is expected.

If  $z_{\max}$  is smaller than the true depth to the bottom of the source, the maximum absolute value of the predicted gravity tensor data will underestimate the maximum absolute value of the observed gravity tensor data (as shown in Fig. B3a). In this case, the theoretical relationship between  $v_p$  and  $s$  is the straight line approximation described by eq. B16b, which is similar to the straight line with negative angular coefficient shown in Fig. B3(f). Conversely, if  $z_{\max}$  is greater than the true depth to the bottom of the source, the maximum absolute value of predicted gravity tensor data will overestimate the maximum absolute value of the observed gravity tensor data (as shown in Fig. B3b). In this case, the theoretical relationship between  $v_p$  and  $s$  is the straight line approximation described by eq. B16a, which is similar to the straight line with positive angular coefficient shown in Fig. B3(f). Finally, if  $z_{\max}$  coincides with the true depth to the bottom of the source, the predicted gravity tensor data will be

approximately equal to the observed gravity tensor data and a minimum value of the  $\ell$ -1 norm of the residuals  $s$  given in eq. B15 is expected. This minimum value of  $s$  is schematically shown in Fig. B3(f). In this way, by varying the thickness of all prisms forming the interpretation model ( $dz$ , in eq. B9) and, consequently, varying the maximum depth to the bottom of the interpretation model ( $z_{\max}$ , in eq. B9) we construct an estimated  $v_p \times s$  curve similar to the theoretical  $v_p \times s$  curve (Fig. B3f). The tentative value for  $z_{\max}$  producing the smallest data-misfit measure  $s$  on the estimated  $v_p \times s$  curve is an optimum estimate of the depth to the bottom of the source.

In this work, we compute the volume  $v_p$  of the estimated source as the sum of the volume of each prism forming the interpretation model. The volume of the  $k$ th prism,  $k=1, \dots, L$ , is given by the product between the thickness  $dz$  and the area  $a^k$  of the horizontal cross section of the  $k$ th prism. This area can be computed as the sum of the area between each pair of adjacent radius within the  $k$ th prism. So, the area  $a^k$  can be given by

$$a^k = \sin(\Delta\theta^k) \frac{1}{2} \left[ (\tilde{r}_{M^k}^k \cdot \tilde{r}_1^k) + \sum_{j=1}^{M^k-1} (\tilde{r}_j^k \cdot \tilde{r}_{j+1}^k) \right], \quad (\text{B17})$$

where  $\Delta\theta^k = 2\pi/M^k$ ,  $k=1, \dots, L$ , is the angle between two adjacent radius within the  $k$ th prism and  $\tilde{r}_j^k$ ,  $j=1, \dots, M^k$ ,  $k=1, \dots, L$ , is a stable estimate of the radial coordinate of the  $j$ th vertex forming the  $k$ th prism. Finally, the volume  $v_p$  of the estimated source is given by

$$v_p = dz \cdot \sum_{k=1}^L a^k, \quad (\text{B18})$$

where  $a^k$  is given by eq. B(17).

In practice, we compute the estimated  $v_p \times s$  curve as follows. First, we establish the depth to the top  $z_0$ , the number of prisms  $L$ , a small value for the thickness  $dz$  of all prisms and, by using the eq. B(9), we calculate the depth to the bottom  $z_{\max}$  of the interpretation model. So, by assuming the correct density contrast  $\rho$  of the geologic source, we estimate a stable parameter vector  $\tilde{\mathbf{m}}$  by using the proposed inverse method (eq. B8). After that, by using the  $\alpha\beta$ -components,  $\alpha\beta = xx, xy, xz, yy, yz, zz$ , of the gravity tensor predicted by the estimated source, we compute the  $\ell$ -1 norm of the residuals  $s$  given in eq. B15. Finally, we compute the volume  $v_p$  of the estimated source by using the eq. B18 and plot  $v_p$  against  $s$ , producing the first point of the estimated  $v_p \times s$  curve. This procedure is repeated for increasingly larger values of bottom depth  $z_{\max}$  of the interpretation model.

In the next section we illustrate the practical use of the estimated  $v_p \times s$  curve for compute the true (or minimum) depth to the bottom of the interpretative model and, consequently, of the source. However, in practice, the estimated  $v_p \times s$  curve does not have the perfect symmetric “<” shape shown in Fig. B3(f). This departure of the estimated  $v_p \times s$  curve from the theoretical  $v_p \times s$  curve (eqs. B16a and B16b) can be attributed to i) large differences between the predicted volume  $v_p$  and the true volume  $v_0$ , which violates the Taylor’s expansion described by the eq. B(11); ii) the inadequacy of the interpretation model in retrieving the true geological body and then the estimated source does not fit acceptably the observed data; iii) the presence of noise in the observed data and; iv) the lack of in-depth resolution of the gravity

gradient data, which is inherent in the nature of potential-field data. These effects will be shown in synthetic tests.

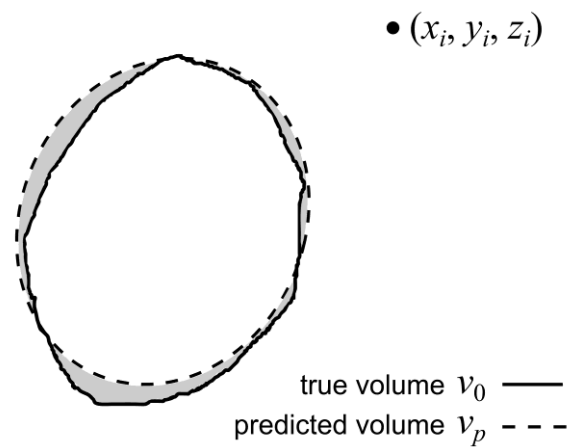


**Figure B2.** 2-D sketch of the true and predicted volumes. The gravity gradient components produced by a homogeneous geologic source with volume  $v_0$  (continuous black line) are measured at the observation point  $(x_i, y_i, z_i)$ . The gravity gradient components produced by a homogeneous estimated source with volume  $v_p$  (dashed black line) are computed at the same observation point  $(x_i, y_i, z_i)$ . The difference between the true ( $v_0$ ) and the predicted ( $v_p$ ) volumes is displayed as grey area.

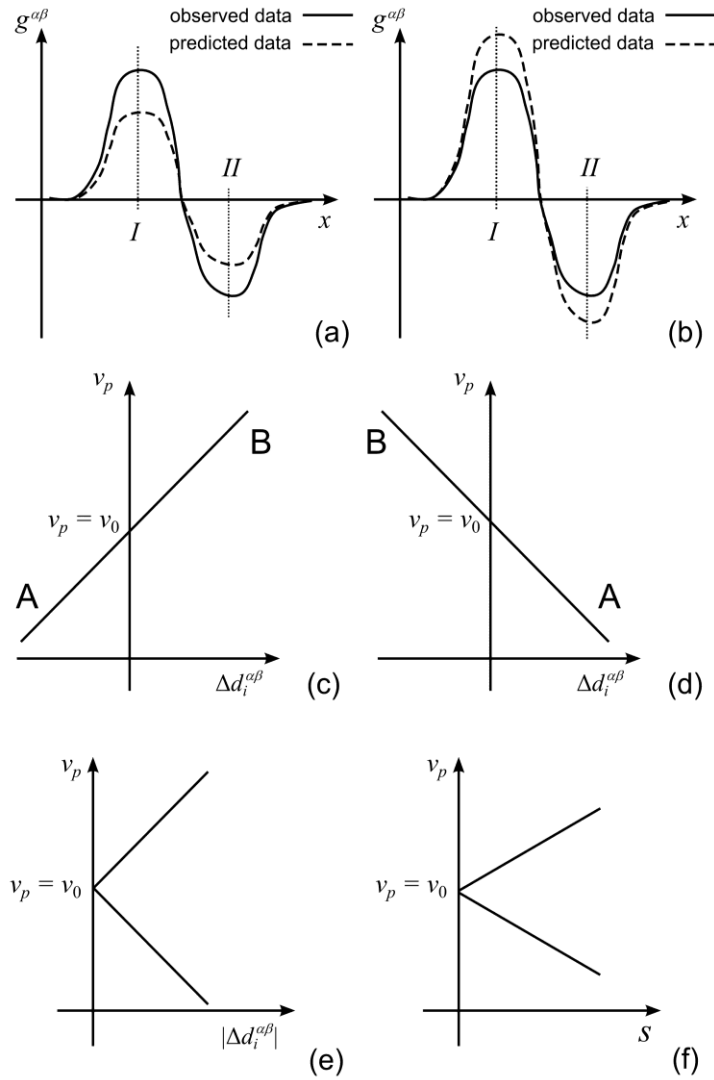


**Figure B3.** Sketches of the linear relationships and the “<” shape of the  $v_p \times s$  curve. Two-dimensional illustration of a case in which the true ( $v_0$ ) and predicted ( $v_p$ ) volumes, respectively, of the true and estimated sources are: (a)  $v_p < v_0$  and (b),  $v_p > v_0$ . Observed (solid line) and predicted (dashed line) gravity gradient components shown in (a) and (b); the former component is produced by a homogeneous geologic body with volume  $v_0$  and the latter component is produced by an estimated source with volume  $v_p$ . Linear relationships between  $\Delta d_i^{\alpha\beta}$  and  $v_p$  calculated, respectively, at the positions (c) I and (d) II. The positions I and II are pinpointed in (a) and (b). The regions A and B displayed in (c) and (d) represent, respectively, the situations in which  $v_p < v_0$  and  $v_p > v_0$ . (e)  $v_p \times |\Delta d_i^{\alpha\beta}|$  curve calculated at the  $i$ th position of the observation. (f)  $v_p \times s$  curve exhibiting its characteristic “<” shape.

## 4. NUMERICAL VALIDATION AND APPLICATION OF THE ESTIMATED $v_p \times s$ CURVE FOR DETERMINING THE TRUE (OR MINIMUM) DEPTH TO THE BOTTOM OF THE SOURCE

Here, we present two tests with synthetic data in order to validate the theoretical statements about the  $v_p \times s$  curve and illustrate the practical use of the estimated  $v_p \times s$  curve for determine the true (or minimum) depth to the bottom  $z_{\max}$  (eq. B9) of the interpretation model and, consequently, the true (or minimum) depth to the bottom of the source. In the first test, the symmetric “<” shape of the  $v_p \times s$  curve (schematically shown in Fig. B3(f) and mathematically described in eqs. B16a and B16b) is confirmed and the synthetic gravity gradient data are able to resolve both the true depth to the bottom of the source and its true volume. In the second synthetic test, we illustrate the situation in which the gravity gradient data cannot resolve both the true source’s bottom and its true volume; however, in this case, the  $v_p \times s$  curve can determine the minimum depth-to-the-bottom and the minimum volume needed for the interpretation model to produce an acceptable data fit.

### 4.1. Validation of the theoretical statements about the $v_p \times s$ curve

We conducted a numerical analysis to validate the theoretical behavior of the  $v_p \times s$  curve and its utility in completely retrieving the geometry of the true source, with correct source’s bottom and volume. For this purpose, we

computed, on plane  $z=0$  m, the synthetic noise-free (not shown) and noise-corrupted data (grey scale maps in Fig. B4) of the  $xx$ -,  $xy$ -,  $xz$ -,  $yy$ -,  $yz$ - and  $zz$ - components of the gravity gradient tensor. The synthetic data are corrupted with a pseudorandom Gaussian noise with zero mean and standard deviation of 3.0 Eötvös and are produced by a single homogeneous source with a density contrast  $\rho$  of 1.0 g/cm<sup>3</sup> relative to the background and a volume of 0.8 km<sup>3</sup> (red prisms in Figs. B5a-c). The source has maximum horizontal dimension of 2400 m and top and base at 150 and 450 m, respectively.

We applied the proposed inverse method to both synthetic noise-free (not shown) and noise-corrupted data (grey scale maps in Fig. B4). In both applications, we used an interpretation model formed by an ensemble of  $L=5$  prisms, all of them with the true density contrast  $\rho^k = 1.0$  g/cm<sup>3</sup> ( $k=1, \dots, L$ ) and the same number of polygon vertices  $M^k = 16$  ( $k=1, \dots, L$ ), which describes the horizontal cross-sections. We also assumed the knowledge about the actual depth to the top of the simulated source, hence we set the depth to the top of the interpretation model as  $z_0 = 150$  m. The five prisms which make up the initial approximation used in both applications have the same horizontal Cartesian coordinates of the arbitrary origins of  $x_0^k = 0.0$  m and  $y_0^k = 0.0$  m for all  $k=1, \dots, 5$ . All vertices forming these prisms have the same radii  $r_j^k = 1000$  m,  $j=1, \dots, 16$ ,  $k=1, \dots, 5$ .

By varying only the depth to the bottom  $z_{\max}$  of the interpretation model, we applied the proposed inverse method to the synthetic noise-corrupted data (grey scale maps in Fig. B4) and produced five estimates. The value of  $z_{\max}$  varies from 350 m to 550 m, in steps of 50 m, which lead to an uncertainty of  $\pm$

25 m in the estimated depth to the bottom. We used all the constraining functions described in the Section 2, except for the third and fourth constraints (named source's outcrop constraint and source's horizontal location constraint, respectively). In all these inversions, the lower and upper bounds for all radii forming all prisms of the interpretation model are 500 m and 1300 m, respectively. Similarly, the lower and upper bounds for all horizontal Cartesian coordinates  $x_0^k$  and  $y_0^k$ ,  $k = 1, \dots, L$ , are -1000 m and 1000 m, respectively. Figs. B5(b) and (c) show perspective views of the estimated 3-D source (blue prisms) with  $z_{\max} = 450$  m. This estimate produces the predicted components of the gravity gradient tensor shown in Fig. B4 (black contour maps) and has a predicted volume  $v_p$  of 0.8 km<sup>3</sup>. The used initial approximation is shown in Fig. B5(a) (blue prisms). Each one of the five estimates obtained with the proposed method produces a  $\ell$ -1 norm of the residuals  $s$  (eq. B15) and a predicted volume  $v_p$  (eq. B18) forming a point on the estimated  $v_p \times s$  curve represented in Fig. B6 by open circles. On this curve, the estimated 3-D source shown in Fig. B5 is associated with the minimum  $s$ , which in turn is obtained by using a maximum depth  $z_{\max} = 450$  m for the interpretation model. This estimated  $v_p \times s$  curve (open circles in Fig. B6), which is obtained from the synthetic noise-corrupted data (grey scale maps in Fig. B4), suggests that the proposed method can retrieve the geometry of the simulated source (red prisms in Fig. B5) completely. This fact is confirmed by Figs. B5(b) and (c), which shows an estimate (blue prism) that retrieves the geometry of the simulated source completely. Notice that, in this synthetic test, the best depth-to-the-bottom ( $450 \pm 25$  m) and source volume (0.8 km<sup>3</sup>) estimates are equal to the true ones.

By applying the proposed method to the noise-free data (not shown), we produced a similar  $v_p \times s$  curve (black dots in Fig. B6) by varying the  $z_{\max}$  from 350 m to 550 m, in steps of 50 m. In contrast with the estimated  $v_p \times s$  curve obtained by using synthetic noise-corrupted data (open circles in Fig. B6), this curve (black dots in Fig. B6) exhibits a perfect symmetric “<” shape. Likewise, the minimum of  $s$  on both estimated  $v_p \times s$  curves (black dots and open circles in Fig. B6) are associated with  $z_{\max} = 450$  m and volume  $v_p = 0.8$  km<sup>3</sup>. The estimated sources (blue prisms) using the maximum depth  $z_{\max} = 450$ m, for both noise-free (not shown) and noise-corrupted (Figs. B5b and c) data, recover very well the geometry of the true simulated source (red prisms in Fig. B5).

Notice that the estimated  $v_p \times s$  curve obtained by using the noise-free data (black dots in Fig. B6) confirms the linear relationships between the estimated source volume  $v_p$  and the  $\ell$ -1 norm of the residuals  $s$ , which were described in the section 3. This curve clearly shows one straight line with a negative angular coefficient and other with a positive angular coefficient. The intersection point of these straight lines occurs very close to  $s = 0$  (black dots in Fig. B6), which represents a perfect fitting of the data. In this particular case, the estimated  $v_p \times s$  curve are perfectly consistent with the theoretical behaviour of the  $v_p \times s$  curve because we are dealing with an ideal synthetic test. This ideal test is characterized by the following factors: (1) the noise-free data set, (2) the adequacy of the interpretation model to retrieve the simulated source, and (3) the sufficient resolution of the gravity gradient data set to resolve the simulated source. Conversely, the estimated  $v_p \times s$  curve obtained by using the noise-corrupted data (open circles in Fig. B6) is slightly different from the theoretical

behaviour of the  $v_p \times s$  curve (see section 3). Likewise, this curve (open circles in Fig. B6) exhibits the linear relationships between  $v_p$  and  $s$ , one with a negative and the other with a positive angular coefficient. In contrast with the theoretical behaviour of the  $v_p \times s$  curve, the straight lines making up the estimated  $v_p \times s$  curve (open circles in Fig. B6) do not intersect each other at  $s = 0$  and do not exhibit a perfect symmetric “<” shape. In this case, the intersection point of the straight lines departs from  $s = 0$  Eötvös because of the presence of noise in data.

We can clearly see well-defined minima of the  $\ell$ -1 norm of the residuals  $s$  in the estimated  $v_p \times s$  curves (Fig. B6) associated with  $z_{\max} = 450$  m, both for noise-free (black dots) and noise-corrupted (open circles) data. These results validate the theoretical basis for determining not only the best estimate of the depth to the bottom of a source, but also the best estimate of its volume, as described in Section 3. The criterion to choose the best depth-to-the-bottom estimate as the tentative value for the maximum depth  $z_{\max}$  producing the minimum of the  $\ell$ -1 norm of the residuals  $s$  is numerically confirmed in this synthetic test. We also validate the criterion to choose as the best source’s volume estimate the one associated with the minimum of  $s$ . In both simulated cases (noise-free and noisy-data, curves in Fig. B6), the best depth-to-the-bottom ( $z_{\max} = 450 \pm 25$  m) and source’s volume ( $v_p = 0.8 \text{ km}^3$ ) estimates are equal to the true ones. Additionally, we conclude that the two gravity-gradient data sets (noise-free and noisy data) have enough resolution to completely retrieve the true volume and the true depth to the bottom of the simulated body. These results confirmed numerically that our criterion for determining both the

source's bottom and its volume, based on a well-defined minimum value of the  $\ell^{-1}$  norm of the residuals  $s$  on the  $v_p \times s$  curve, is empirically sound.

#### **4.2. The use of the estimated $v_p \times s$ curve for determine the true (or minimum) depth to the bottom of the source**

In the previous synthetic test, the estimated  $v_p \times s$  curves (Fig. B6) show well-defined minima of  $s$  indicating that the synthetic gravity-gradient data have enough resolution to completely retrieve the geometry of the simulated source, assuming the correct knowledge about its top and density contrast. In this section, we illustrate with synthetic gravity-gradient data the situation in which the data do not have enough resolution to completely recover the geometry of the simulated source. Here, we analyzed the validation and the utility of the  $v_p \times s$  curve in recovering, at most, the lower-bound estimates of the source's depth to the bottom and of the source's volume. The results of this analysis are compared with a case in which the  $v_p \times s$  curve can determine correctly both the true source's depth to the bottom and the true source's volume.

For these purposes, we computed, on plane  $z = 0$  m, three synthetic data sets of the  $xx$ -,  $xy$ -,  $xz$ -,  $yy$ -,  $yz$ - and  $zz$ - components of the gravity gradient tensor which were corrupted with a pseudorandom Gaussian noise with zero mean and standard deviation of 2.0 Eötvös. These data sets were produced by dipping bodies with density contrast  $\rho$  of 1.0 g/cm<sup>3</sup> and depth to the top of 50 m. These bodies differ from each other by the depths to their bottoms. Fig. B7 shows grey scale maps of the six components of the gravity gradient tensor which were produced by the shallow-bottomed body (depth to the bottom at 350

m) shown in Fig. B9 (red prisms). Fig. B8 shows grey scale maps of  $xx$ -,  $yy$ - and  $zz$ - components of the gravity gradient tensor which were produced by the deep-bottomed body (depth to the bottom at 1000 m) shown in Fig. B10 (red prisms). The other components produced by the deep-bottomed body, as well as, the synthetic data set produced by the intermediate-bottomed body (depth to the bottom at 550 m) are not shown.

We applied the proposed inverse method to all synthetic noise-corrupted components of the gravity-gradient tensor produced by the three simulated sources. In all applications, we used an interpretation model formed by an ensemble of  $L = 7$  prisms, all of them with the true density contrast  $\rho^k = 1.0$  g/cm<sup>3</sup> ( $k = 1, \dots, 7$ ) and the same number of polygon vertices  $M^k = 8$  ( $k = 1, \dots, 7$ ), which describe the horizontal cross-sections. We also assumed the knowledge about the actual depth to the top of the simulated sources, hence we set the depth to the top of the interpretation model as  $z_0 = 50$  m. The seven prisms which make up the initial approximations used in all applications have the same horizontal Cartesian coordinates  $x_0^k = 120$  m and  $y_0^k = -80$  m,  $k = 1, \dots, 7$ , of the arbitrary origins. All vertices forming these seven prisms have the same radii  $r_j^k = 50$  m, for all  $j = 1, \dots, 8$ ,  $k = 1, \dots, 7$ . In all inversions we used all the constraining functions described in the Section 2, except for the fourth and sixth constraints (named source's horizontal location and minimum Euclidean norm constraints, respectively). Here, the lower and upper bounds for all radii forming all prisms of the interpretation model are 0 m and 300 m, respectively. Similarly, the lower and upper bounds for all horizontal Cartesian coordinates of the arbitrary origins are -600 m and 600 m, respectively.

Fig. B11 shows the estimated  $v_p \times s$  curves A, B and C, which are produced by inverting the synthetic gravity-gradient data produced, respectively, by the shallow- (red prisms in Fig. B9), deep- (red prisms in Fig. B10) and intermediate-bottomed (not shown) sources. Each  $v_p \times s$  curve contains six black dots, each one associated with an estimated 3-D source producing a  $v_p$  (the predicted volume given by eq. B18) and an  $s$  (the  $\ell$ -1 norm of the data-misfit measure given by eq. B15). In each one of the three estimated curves, the six estimates are obtained by varying the depth to the bottom  $z_{\max}$  of the interpretation model. In the estimated  $v_p \times s$  curve A, the  $z_{\max}$  varies from 200 m to 450 m, in steps of 50 m, which lead to an uncertainty of  $\pm 25$  m in the depth-to-the-bottom estimate of the simulated shallow-bottomed source. In the estimated  $v_p \times s$  curve B, the  $z_{\max}$  varies from 400 m to 1400 m, in steps of 200 m, which lead to an uncertainty of  $\pm 100$  m in the depth-to-the-bottom estimate of the simulated deep-bottomed source. In the estimated  $v_p \times s$  curve C, the  $z_{\max}$  varies from 250 m to 750 m, in steps of 50 m, which lead to an uncertainty of  $\pm 25$  m in the depth-to-the-bottom estimate of the simulated intermediate-bottomed source.

The minima of  $s$  on the estimated  $v_p \times s$  curves A, B and C (Fig. B11) do not occur at zero Eötvös because the presence of noise in data. By comparing the estimated  $v_p \times s$  curves produced by the shallow- (curve A in Fig. B11) and deep- (curve B in Fig. B11) bottomed sources, we verify contrasting patterns. The  $v_p \times s$  curve produced by the shallow-bottomed source (curve A in Fig. B11) has a well-defined minimum of  $s$ , while the minimum of  $s$  on the  $v_p \times s$  curve

produced by the deep-bottomed source (curve B in Fig. B11) is ill defined. This difference occurs because, under the imposed constraints, the gravity gradient data produced by the shallow-bottomed source (red prisms in Fig B9) have enough resolution to estimate both the true depth to the bottom and the true volume of the simulated source. In contrast, the gravity gradient data produced by the simulated deep-bottomed source (red prisms in Fig B10) are unable to resolve both the maximum depth to the source bottom and the correct volume of the source.

In accordance with the proposed theory (Section 4.1), the well-defined minimum value of  $s$  on the  $v_p \times s$  curve A (Fig. B11) is produced by an estimate (blue prisms in Figs. B9b and c) that recovers completely the shape of the simulated shallow-bottomed source (red prisms in Fig B9). This estimate produces predicted gravity gradient components (black contour lines in Fig. B7), that fit the synthetic noise-corrupted data (grey scale maps in Fig. B7) having a bottom depth of  $z_{\max} = 350 \pm 25$  m and a predicted volume of  $v_p = 0.012$  km<sup>3</sup>, both of them coinciding with the true ones. The initial approximation used in this inversion is shown in Fig. B9(a).

Similarly to the estimated  $v_p \times s$  curve A, the estimated  $v_p \times s$  curve C (Fig. B11) is produced by applying our inverse method to the synthetic noise-corrupted data produced by the intermediate-bottomed body (not shown). Although the minimum of  $s$  on the curve C is not so well-defined as in curve A, we stress that this minimum is produced by an estimated 3-D source (not shown) that recover very well the geometry of the simulated intermediate-bottomed body (not shown). This estimate has a bottom depth  $z_{\max} = 550$  m

and a predicted volume of  $v_p = 0.020 \text{ km}^3$ , both of them coinciding with the true ones. Moreover, this estimate also produces gravity gradient components (not shown) fitting the synthetic noise-corrupted data (not shown).

In contrast with the estimated  $v_p \times s$  curve A, the estimated  $v_p \times s$  curve B (Fig. B11) exhibits an ill-defined minimum of  $s$ , which indicates that the synthetic gravity-gradient data (grey scale maps in Fig. B8) produced by the deep-bottomed body (red prisms in Fig. B10) do not have enough resolution for retrieve the geometry of the simulated body completely. The  $v_p \times s$  curve B (Fig. B11) reveals multiple minima of  $s$ , which are associated with  $z_{\max}$  greater than or equal to 800 m. Figs. B10(b) and (c) show two perspective views of the estimated deep-bottomed source (blue prisms) using the maximum depth of  $z_{\max} = 800 \text{ m}$  for the interpretation model. This estimated source (blue prisms in Figs. B10b and c) is obtained by using the initial approximation (blue prisms) shown in Fig. B10(a). Figs. B10(e) and (f) show two perspective views of the estimated deep-bottomed source (blue prisms) using the maximum depth of  $z_{\max} = 1000 \text{ m}$  for the interpretation model. This estimated source (blue prisms in Figs. B10e and f) is obtained by using the initial approximation (blue prisms) shown in Fig. B10(d). These estimates (blue prisms in Figs. B10b-c and Figs. B10e-f) produce, practically, the same values of  $s$  on the  $v_p \times s$  curve B (Fig. B11) and might be equally accepted because their corresponding predicted gravity gradient components (black contour lines in Figs. B8a-c and Figs. B8d-f) produce equally acceptable data fits. Although the estimate shown in Figs. B10(b) and (c) (blue prisms) retrieves the geometry of the simulated body until the depth 800 m, it has a depth to the bottom ( $z_{\max} = 800 \text{ m}$ ) smaller than the

true one (1000 m) and a volume ( $v_p = 0.031 \text{ km}^3$ ) smaller than the true one ( $0.038 \text{ km}^3$ ). On the other hand, although the estimate shown in Figs. B10(e) and (f) (blue prisms) has correct depth to the bottom ( $z_{\max} = 1000 \text{ m}$ ) and correct volume ( $v_p = 0.038 \text{ km}^3$ ), it does not recover the geometry of the simulated body at depths greater than 800 m.

These results confirm that estimated  $v_p \times s$  curves presenting well-defined minima of  $s$  (e.g., the curves A and C in Fig. B11) can be used to determine estimates that recover very well the shape of the true bodies, with the corrects bottom depth and volume (e.g., the blue prisms in Figs. B9b and c). These estimates, associated with the well-defined minimum of  $s$  on the estimated  $v_p \times s$  curve, produce gravity-gradient components yielding acceptable data fits (e.g., black contour lines in Fig. B7). On the other hand, we concluded that estimated  $v_p \times s$  curves presenting ill-defined minima of  $s$  (e.g., the curve B in Fig. B11) can be used to determine, at most, the lower-bounds for the depth to the bottom and the volume of the true body. This is illustrated by the results obtained with the deep-bottomed body (red prism in Fig. B10). In this case, the estimated  $v_p \times s$  curve (curve B in Fig. B11) can be used to determine the estimate (blue prisms in Figs. B10b and c) having the minimum depth to the bottom ( $z_{\max} = 800 \text{ m}$ ) and minimum volume ( $v_p = 0.031 \text{ km}^3$ ) needed to produce predicted gravity gradient components (e.g., black contour lines in Figs. B8a-c) that fit the synthetic noise-corrupted data (grey scale maps in Fig. B8). Notice that the estimated 3-D source (blue prisms in Figs. B10b and c) retrieves the geometry of the upper part of the true body (red prisms in Fig. B10) completely. This result confirmed numerically that our criterion for

determining the lower bounds for both the source's bottom and its volume, based on an ill-defined minimum value of  $s$  on the  $v_p \times s$  curve, is empirically sound.

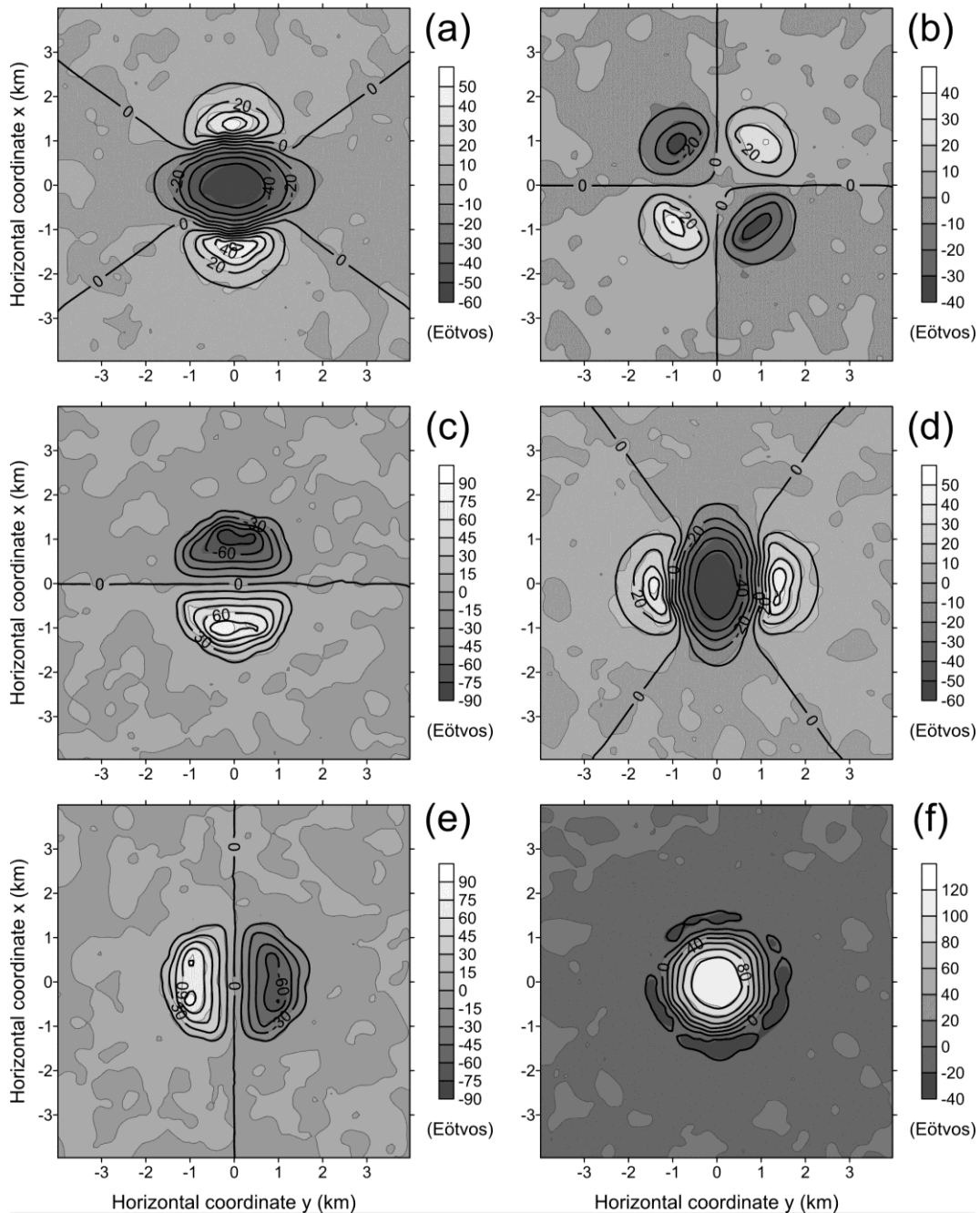


**Figure B4.** Test with synthetic data. Synthetic noise-corrupted (grey scale maps) and predicted (black contour maps) of the (a)  $xx$  -, (b)  $xy$  -, (c)  $xz$  -, (d)  $yy$  -, (e)  $yz$  - and (f)  $zz$  - components of the gravity gradient tensor. The synthetic components are produced by the simulated body shown in Fig. B5 (red prisms). The predicted components are produced by the estimated body shown in Figs. B5(b) and (c) (blue prisms).

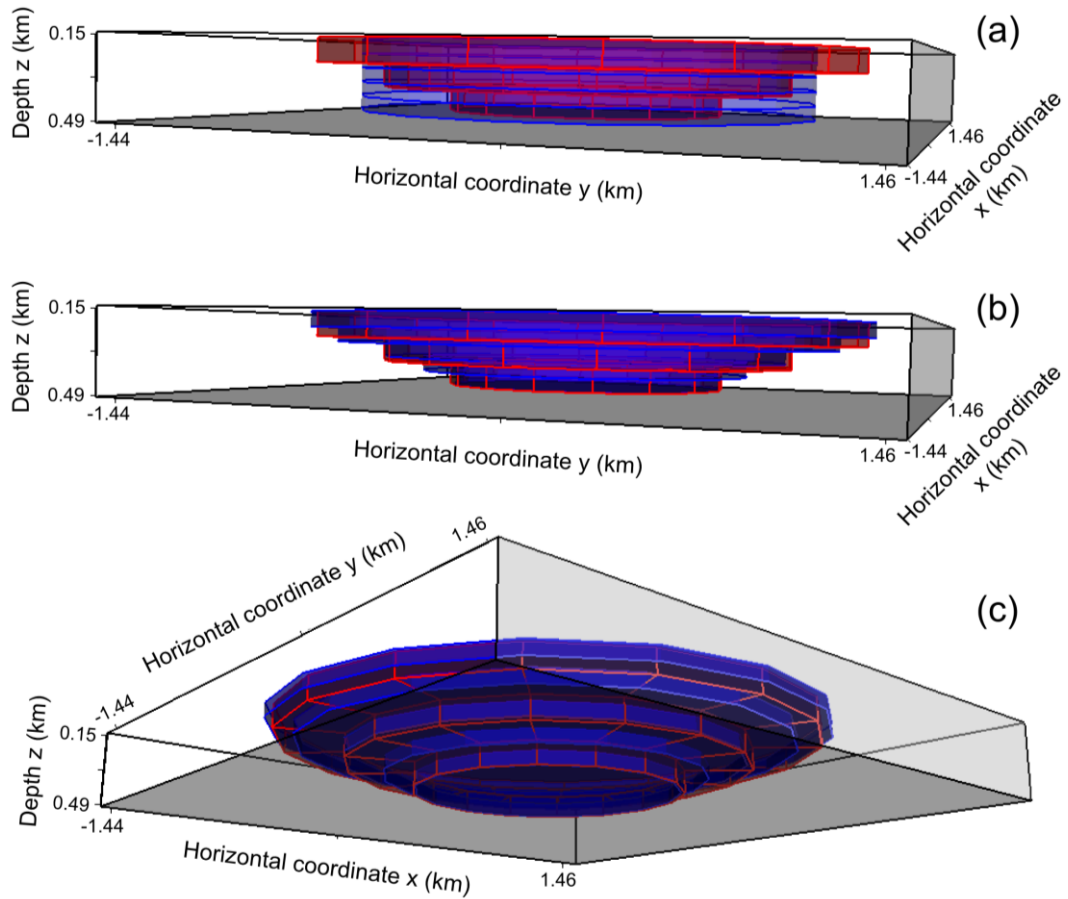


**Figure B5.** Test with synthetic data. Perspective views of the simulated body (red prisms) with depth to the bottom of 450 m and volume of 0.8 km<sup>3</sup>. Perspective views in blue prisms of the (a) initial approximation, (b) and (c) estimated body. The estimated body in (b) and (c) is obtained by inverting the noise-corrupted data shown in Fig. B4 (grey scale maps) and assuming an interpretation model with depth to the bottom  $z_{\max} = 450$  m. The estimated body has a predicted volume  $v_p = 0.8$  km<sup>3</sup> and produces the predicted gravity gradient data shown in Fig. B4 (black contour maps).

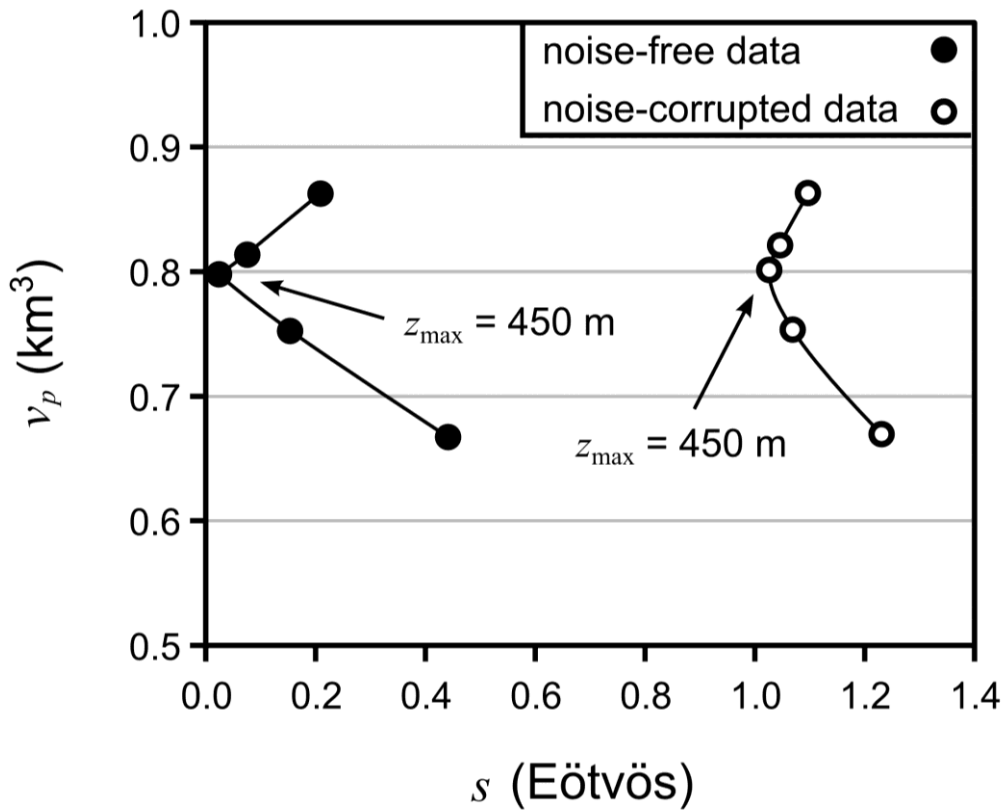


**Figure B6.** Test with synthetic data. Estimated  $v_p \times s$  curves obtained by inverting the noise-free (black dots) and noise-corrupted (open circles) data produced by the simulated body shown in Fig. B5 (red prisms). These curves are produced by varying the maximum depth to the bottom  $z_{\max}$  of the interpretation model from 350 m to 550 m, in steps of 50 m. The estimated body producing the well-defined minimum  $s$  on the  $v_p \times s$  curve (open circles) obtained with the noise-corrupted data (grey scale maps in Fig. B4) is shown in Figs. B5(b) and (c).

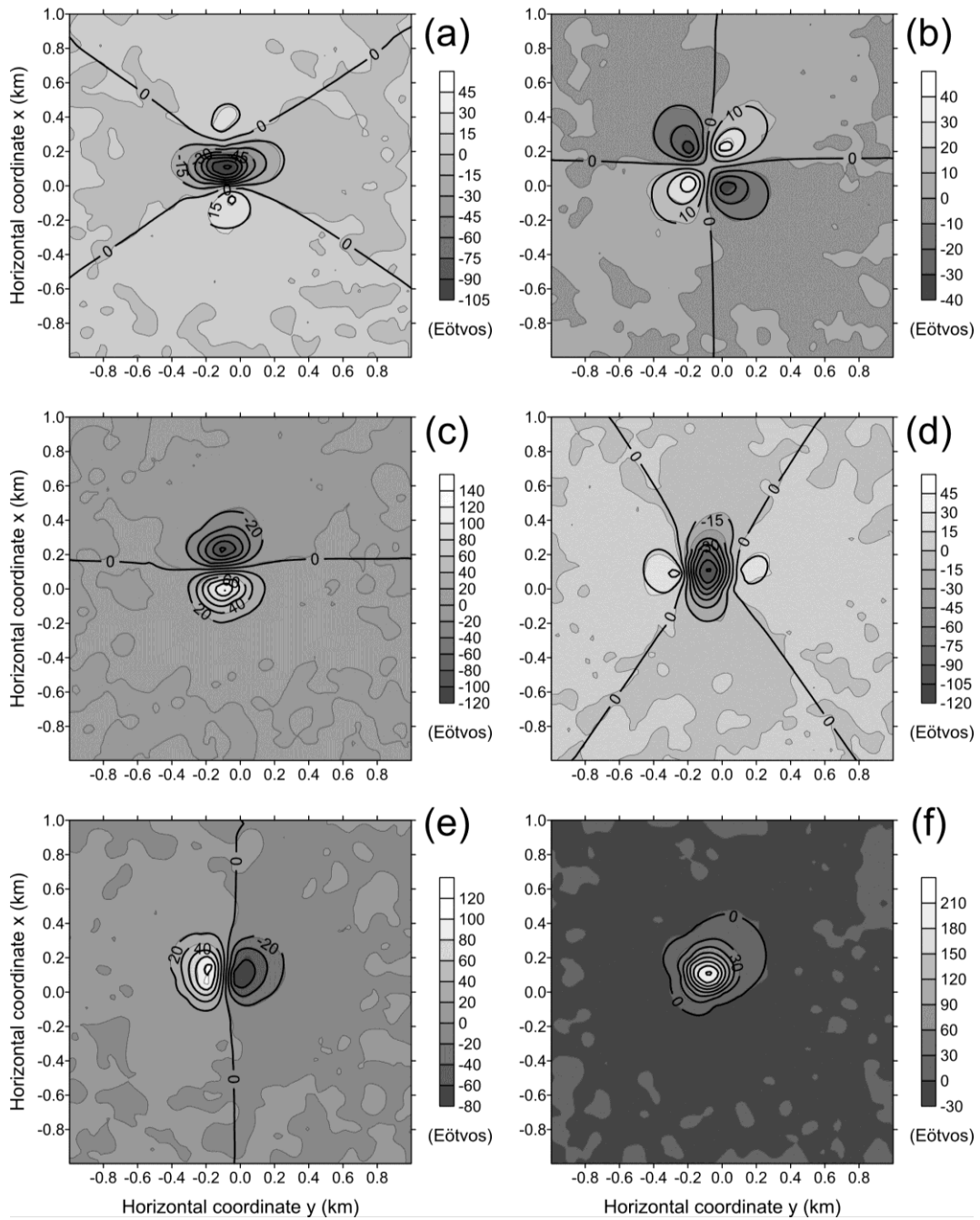


**Figure B7.** Test with synthetic data produced by dipping bodies. The grey scale maps represent the noise-corrupted (a)  $xx$ -, (b)  $xy$ -, (c)  $xz$ -, (d)  $yy$ -, (e)  $yz$ - and (f)  $zz$ - components of the gravity gradient tensor produced by the simulated shallow-bottomed body shown in Fig. B9 (red prisms). The black contour maps are the predicted data produced by the estimated body (blue prisms) shown in Figs. B9(b) and (c).

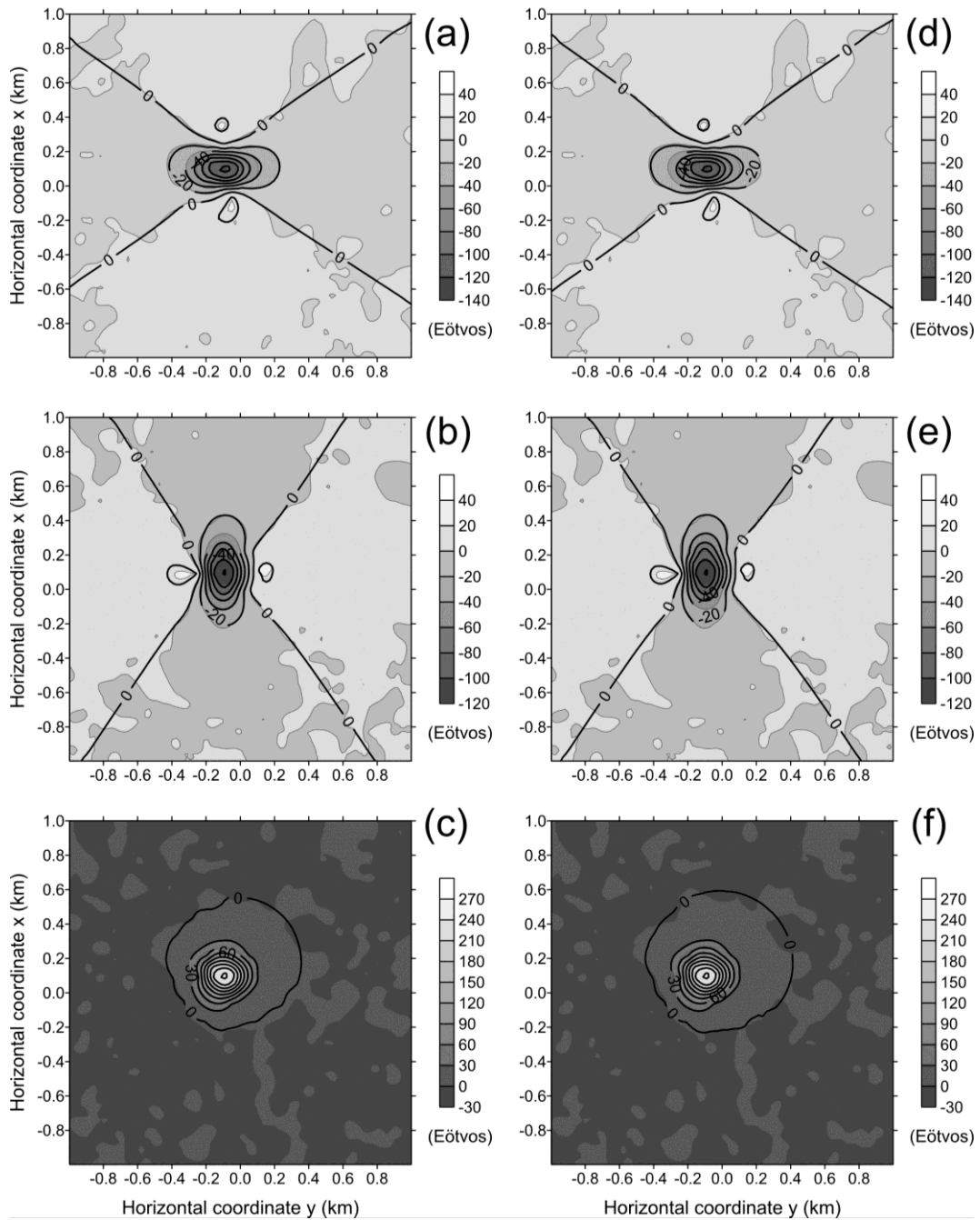


**Figure B8.** Test with synthetic data produced by dipping bodies. The grey scale maps represent the noise-corrupted (a) and (d)  $\alpha\alpha$ -, (b) and (e)  $\beta\beta$ - and (c) and (f)  $\gamma\gamma$ - components of the gravity gradient tensor produced by the simulated deep-bottomed body shown in Fig. B10 (red wire-frame body). The black contour maps shown in (a)-(c) and (d)-(f) are, the  $\alpha\alpha$ -,  $\beta\beta$ - and  $\gamma\gamma$ - components of the predicted data produced by the estimated bodies (blue prisms) shown in Figs. B10(b) and (c) and Figs. B10(e) and (f), respectively. The other components of gravity gradient data are not shown.

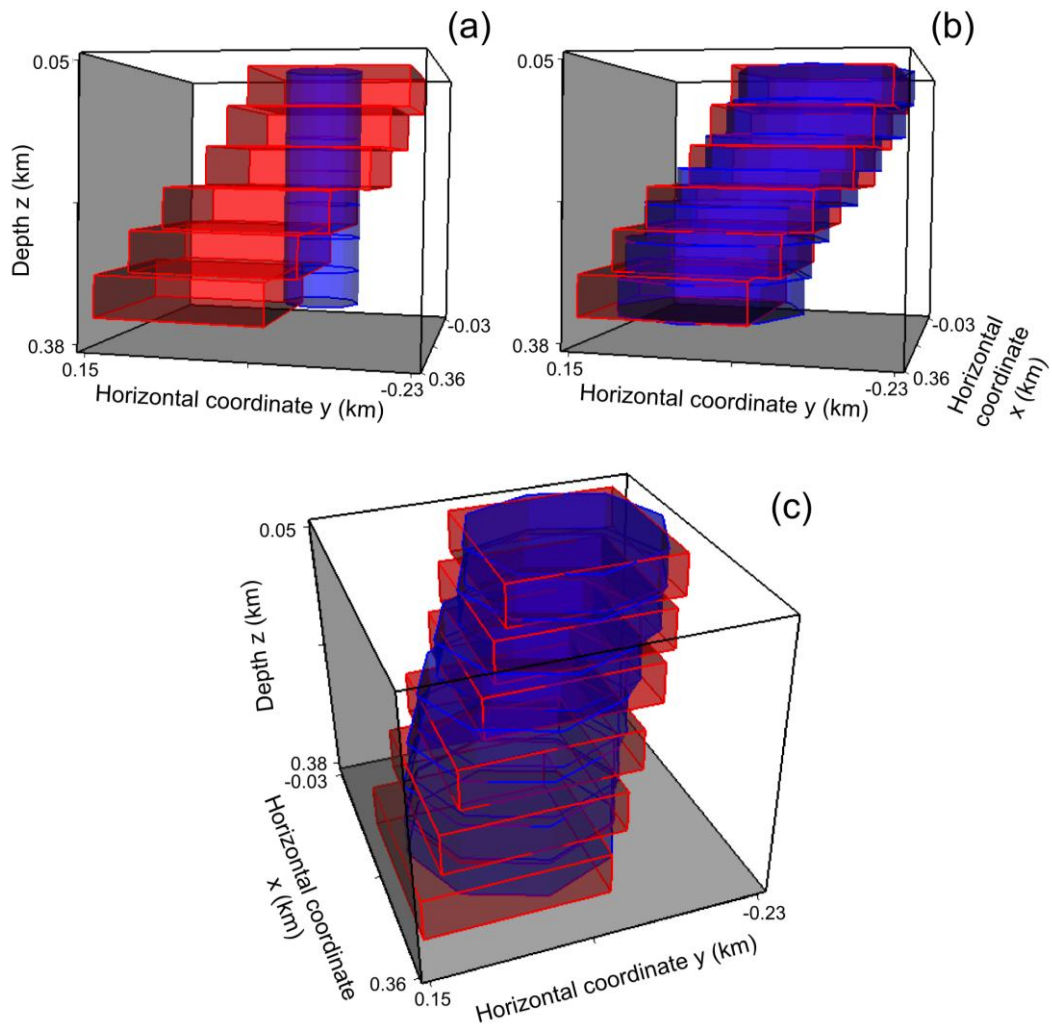


**Figure B9.** Test with synthetic data produced by dipping bodies. Perspective views of the simulated shallow-bottomed body (red prisms) with depth to the bottom of 350 m and volume 0.012 km<sup>3</sup>. Perspective views in blue prisms of the (a) initial approximation and (b) and (c) estimated body. The estimated body (b) and (c) is obtained by inverting the noise-corrupted data shown in Fig. B7 (grey scale maps) and assuming an interpretation model with depth to the bottom  $z_{\max} = 350$  m. The estimated body has a predicted volume  $v_p = 0.012$  km<sup>3</sup> and produces the predicted gravity gradient data shown in Fig. B7 (black contour maps).

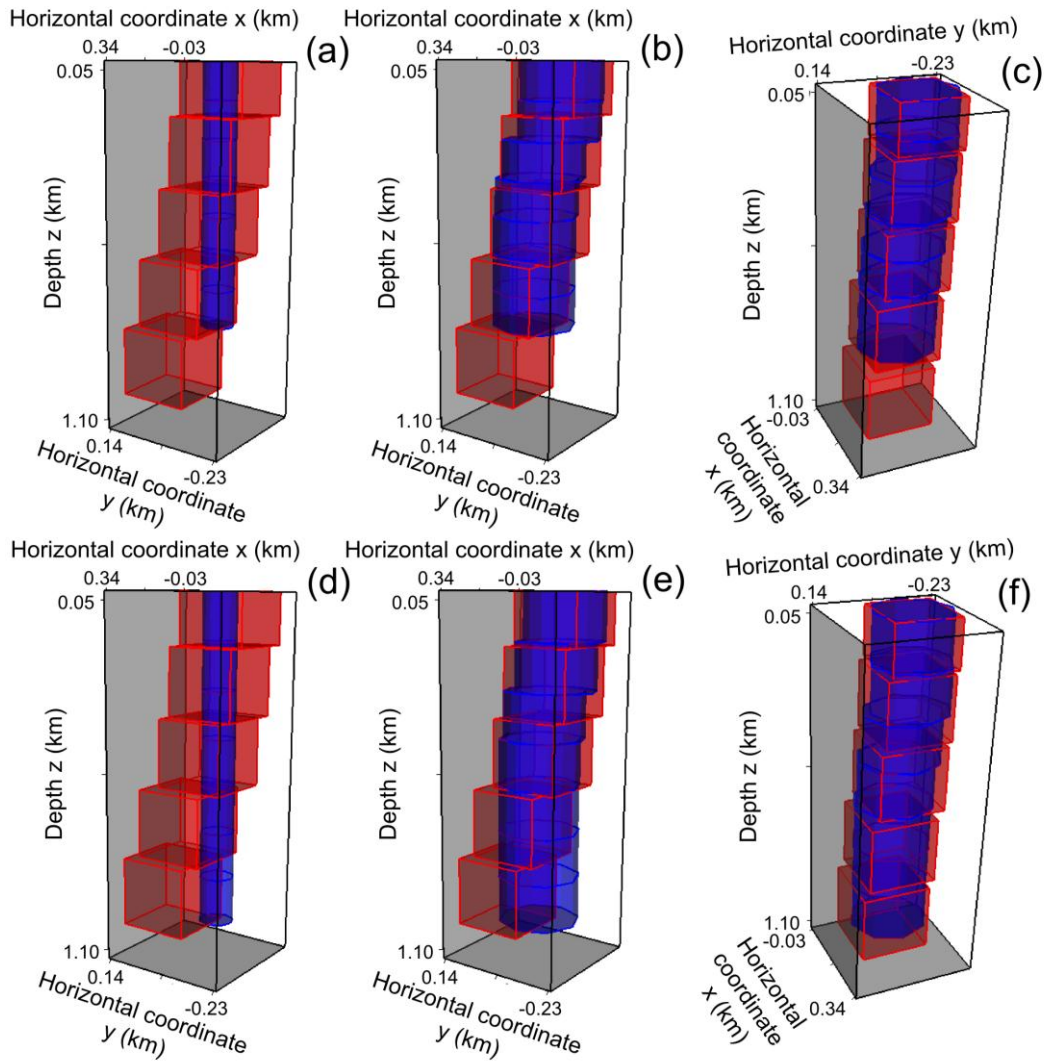


**Figure B10.** Test with synthetic data produced by dipping bodies. Perspective views of the simulated deep-bottomed body (red prisms) with depth to the bottom of 1000 m and volume  $0.038 \text{ km}^3$ . Perspective views in blue prisms of the (a) and (d) initial approximations and (b)-(c) and (e)-(f) estimated bodies. The estimated bodies shown in (b)-(c) and (e)-(f) are obtained by inverting the noise-corrupted data shown in Fig. B8 (grey scale maps). The maximum depths to the bottoms assumed for interpretation models to obtain the estimates shown in (b)-(c) and (e)-(f) are, respectively,  $z_{\text{max}} = 800 \text{ m}$  and  $z_{\text{max}} = 1000 \text{ m}$ . The estimated body (blue prisms) in (b)-(c) has a predicted volume  $v_p = 0.031 \text{ km}^3$  and produces the predicted gravity gradient data shown in Figs. B8(a)-(c) (black contour maps). The estimated body (blue prisms) in (e)-(f) has a predicted volume  $v_p = 0.038 \text{ km}^3$  and produces the predicted gravity gradient data shown in Figs. B8(d)-(f) (black contour maps).

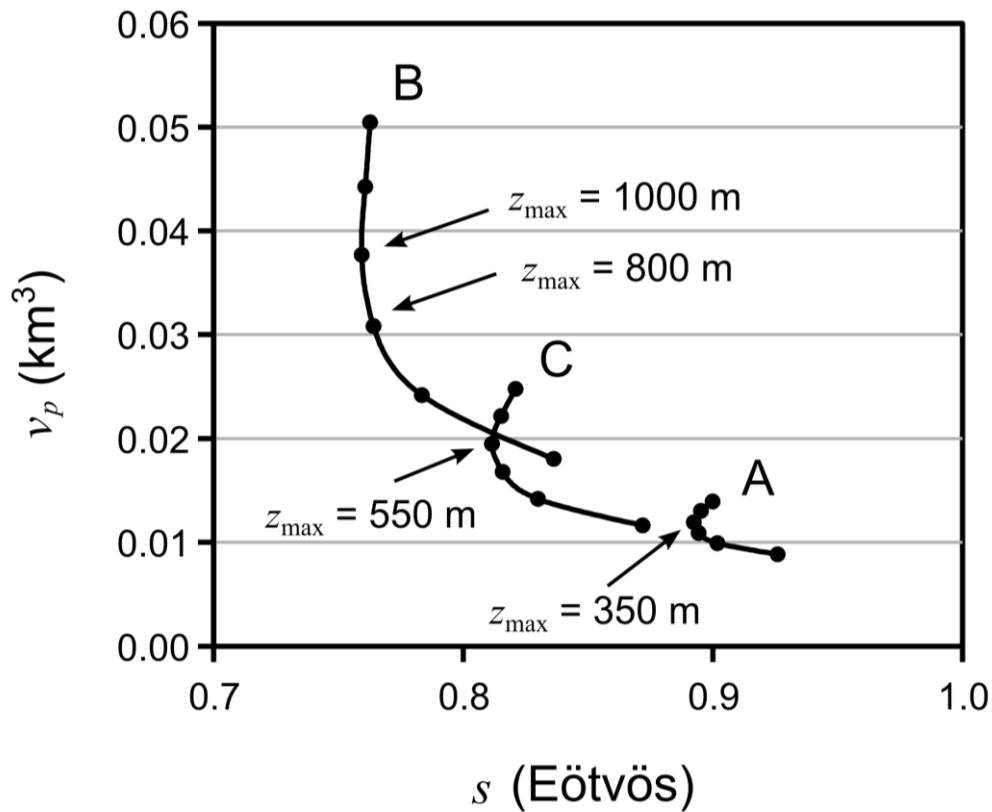


**Figure B11.** Test with synthetic data produced by dipping bodies. The estimated  $v_p \times s$  curves A, B and C are obtained by inverting the noise-corrupted data produced, respectively, by the shallow- (red prisms in Fig. B9), intermediate- (not shown) and deep- (red prisms in Fig. B10) bottomed bodies. The estimated body (blue prisms in Figs. B9b and c) producing the well-defined minimum of  $s$  on the curve A has a depth to the bottom  $z_{\max} = 350$  m and a predicted volume  $v_p = 0.012$  km<sup>3</sup>. The estimated bodies producing the two pinpointed ill-defined minima of  $s$  on the curve B are shown in Figs. B10(b)-(c) and B10(e)-(f) (blue prisms). The estimated body shown in Figs. B10(b)-(c) has a depth to the bottom  $z_{\max} = 800$  m and a predicted volume  $v_p = 0.031$  km<sup>3</sup>. The estimated body shown in Figs. B10(e)-(f) has a depth to the bottom  $z_{\max} = 1000$  m a predicted volume  $v_p = 0.038$  km<sup>3</sup>. The estimated body (not shown) producing the well-defined minimum  $s$  on the curve C has a depth to the bottom  $z_{\max} = 550$  m and a predicted volume  $v_p = 0.020$  km<sup>3</sup>.

## 5. APPLICATION TO SYNTHETIC DATA

We evaluate the performance of the proposed method by simulating two geologic settings based on a real geologic environment. The first one is based on the forward modeling of a gravity-gradient survey over the Vinton salt dome, USA, reported by Ennen & Hall (2011). The second geologic setting is based on the prior geologic information about the Vinton salt dome and the surrounded rocks.

### 5.1. Cap rock model based on Ennen & Hall (2011) forward modeling

We computed, at  $z = -80$  m, the  $xx$ -,  $xy$ -,  $xz$ -,  $yy$ -,  $yz$ - and  $zz$ - noise-corrupted components of the gravity-gradient tensor (grey scale maps in Fig. B12) produced by a synthetic body simulating a salt-dome cap rock. To simulate experimental errors, all components of the gravity-gradient tensor are corrupted with a pseudorandom Gaussian noise with zero mean and a standard deviation of 5.0 Eötvös. The simulated body is based on the forward modeling of a gravity-gradient survey over the Vinton salt dome, USA, reported by Ennen & Hall (2011). This simulated salt-dome cap rock (red wire-frame body in Fig. B13) is a pyramid with skewed shape extending in depth from 160 m to 360 m, with density contrast  $\rho$  of 1.23 g/cm<sup>3</sup> and volume 0.176 km<sup>3</sup>.

We applied our method by using an interpretation model formed by an ensemble of  $L = 7$  prisms, all of them with the true density contrast  $\rho^k = 1.23$  g/cm<sup>3</sup> ( $k = 1, \dots, 7$ ) and the same number of polygon vertices  $M^k = 16$  ( $k = 1, \dots, 7$ ), which describe the horizontal cross-sections. We also assumed the

knowledge about the actual depth to the top of the simulated source, hence we set the depth to the top of the interpretation model as  $z_0 = 160$  m. The seven prisms which make up the initial approximation have the same horizontal Cartesian coordinates  $x_0^k = 1284$  m and  $y_0^k = 1739$  m,  $k = 1, \dots, 7$ , of the arbitrary origins. The radii forming the shallowest prism ( $r_j^1$ ,  $j = 1, \dots, 16$ ) are equal to 100 m; the radii forming the second prism ( $r_j^2$ ,  $j = 1, \dots, 16$ ) are equal to 200 m. The sizes of radii of the third prism up to the seventh prism are increased successively by adding 100 m, until the radii of the deeper prism ( $r_j^7$ ,  $j = 1, \dots, 16$ ) attain 700 m.

We construct the estimated  $v_p \times s$  curve (Fig. B14) by producing eight estimated sources, each one with a fixed maximum depth  $z_{\max}$  of the interpretation model. The  $z_{\max}$  varies from 300 m to 440 m, in steps of 20 m leading to an uncertainty of  $\pm 10$  m in the estimated depth to the bottom. Each one of the eight estimates produces a pair of  $s$  and  $v_p$  (black dots in Fig. B14) on the estimated  $v_p \times s$  curve. This curve presents a well-defined minimum of  $s$ , associated with  $z_{\max} = 360$  m of the interpretation model. Fig. B13 shows the initial approximation (blue prisms in Fig. B13a) and two perspective views of the estimated salt-dome cap rock (blue prisms in Figs. B13b and c) using the maximum depth  $z_{\max} = 360$  m to set up the interpretation model. Notice that this estimated salt-dome cap rock completely retrieves the geometry of the simulated source (red wire-frame body in Fig. B13) with the correct depth to the bottom ( $z_{\max} = 360$  m) and volume ( $v_p = 0.177$  km<sup>3</sup>). The predicted data (black contour maps in Fig. B12) produced by this new estimated salt-dome cap rock

fit acceptably the observed gravity-gradient data (grey scale maps in Fig. B12). The histograms of the residuals (Fig. B15) confirm the acceptance of the data fitting. These histograms resemble bell-shaped patterns indicating that the residuals of all components follow normal distributions. Moreover, the sample standard deviations  $\sigma$  calculated from the residuals (Fig. B15) are very close to the standard deviation of 5.0 Eötvös of the pseudorandom Gaussian noise realizations added to the synthetic data aiming at simulating experimental errors. These results show the good performance of our method in recovering the entire geometry of a salt-dome cap rock like the one modeled by Ennen & Hall (2011).

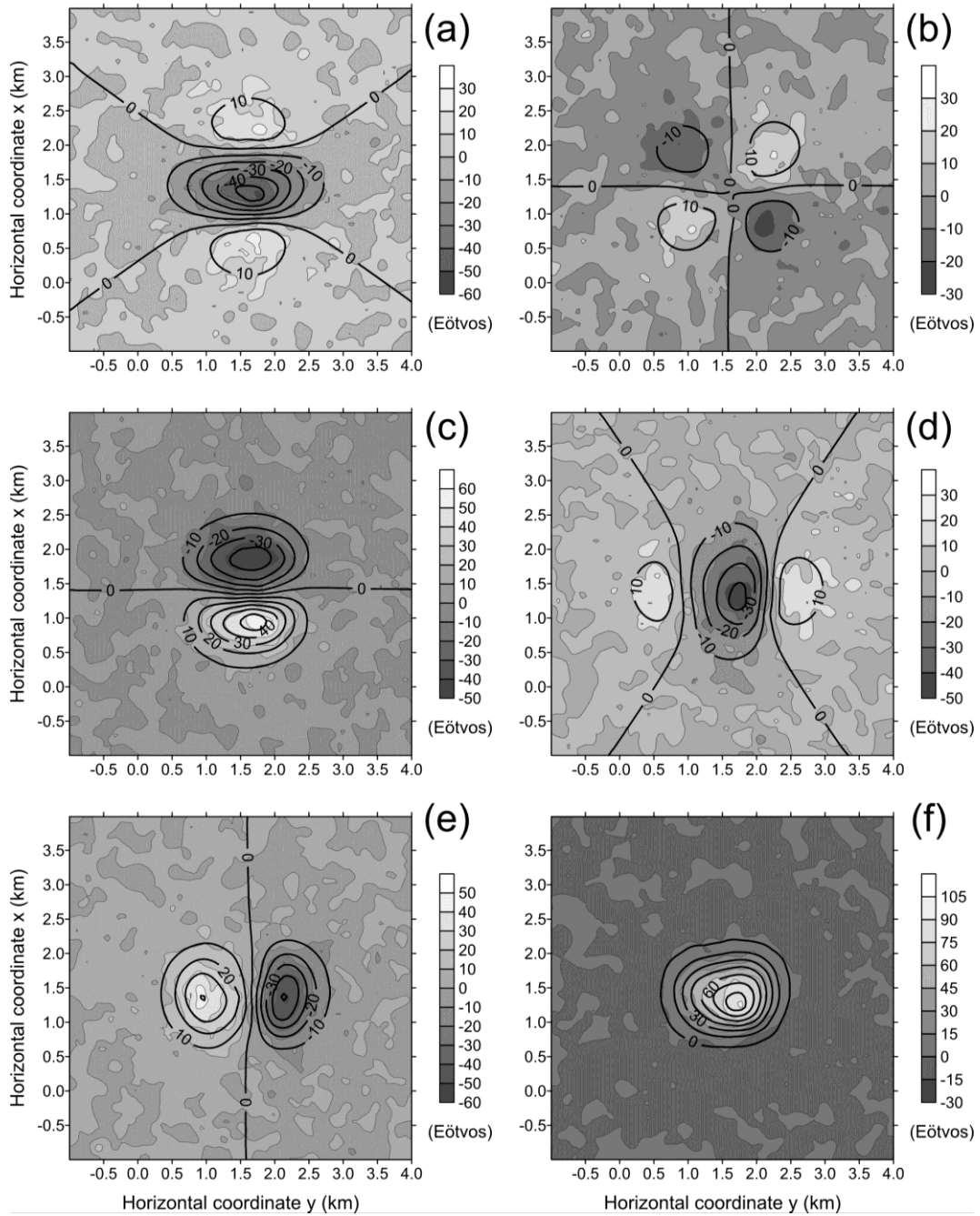


**Figure B12.** Test with synthetic data produced by a simulated salt-dome cap rock based on Ennen & Hall's (2011) work. Synthetic noise-corrupted (grey scale maps) and predicted (black contour maps) of the (a)  $xx$ -, (b)  $xy$ -, (c)  $xz$ -, (d)  $yy$ -, (e)  $yz$ - and (f)  $zz$ - components of the gravity gradient tensor. The synthetic components are produced by the simulated salt-dome cap rock shown in Fig. B13 (red wire-frame body). The predicted components are produced by the estimated body shown in Figs. B13(b) and (c) (blue prisms).

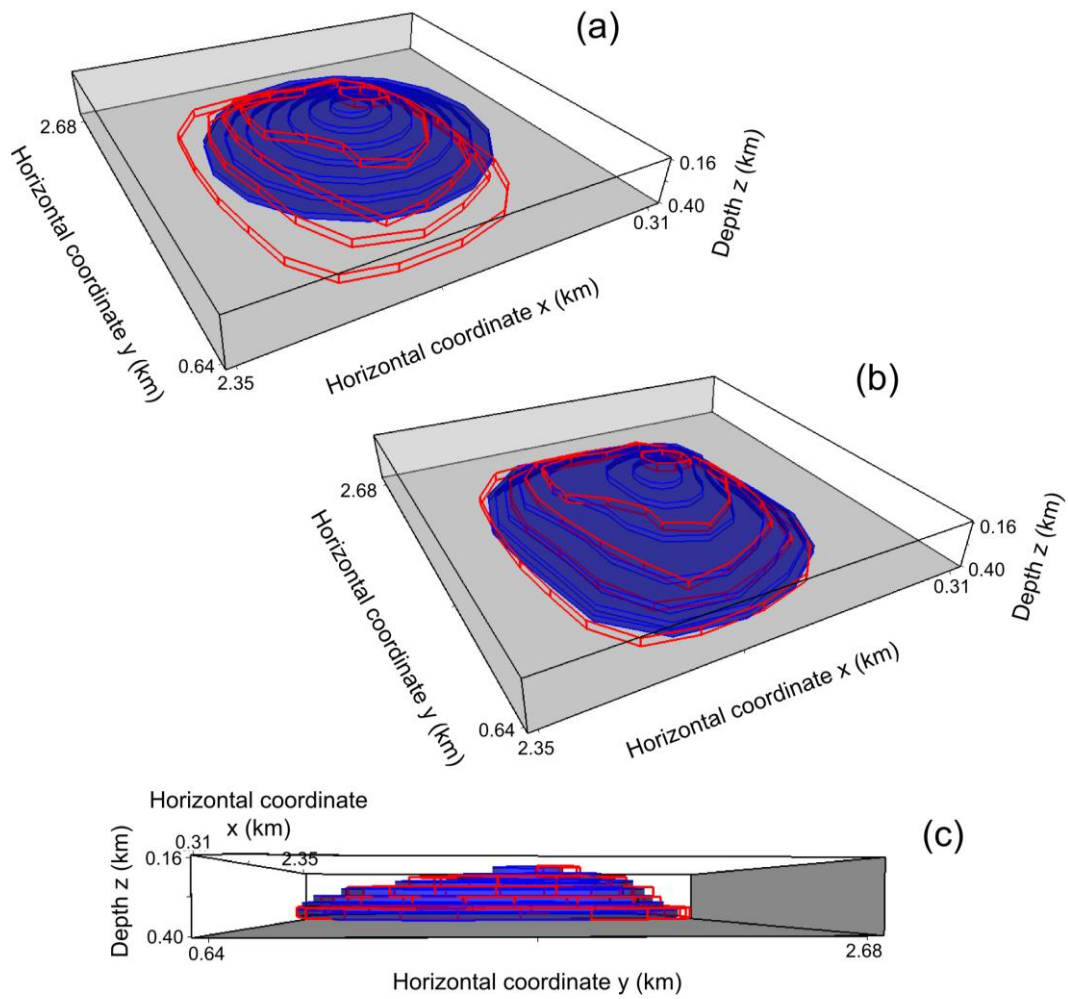


**Figure B13.** Test with synthetic data produced by a simulated salt-dome cap rock based on Ennen & Hall's (2011) work. Perspective views of the simulated salt-dome cap rock (red wire-frame body) with depth to the bottom at 360 m and volume 0.177 km<sup>3</sup>. Perspective views in blue prisms of the (a) initial approximation, (b) and (c) estimated body. The estimated body in (b) and (c) is obtained by inverting the noise-corrupted data shown in Fig. B12 (grey scale maps) and assuming an interpretation model with depth to the bottom  $z_{\max} = 360$  m. The estimated body has a predicted volume  $v_p = 0.177$  km<sup>3</sup> and produces the predicted gravity-gradient data shown in Fig. B12 (black contour maps).

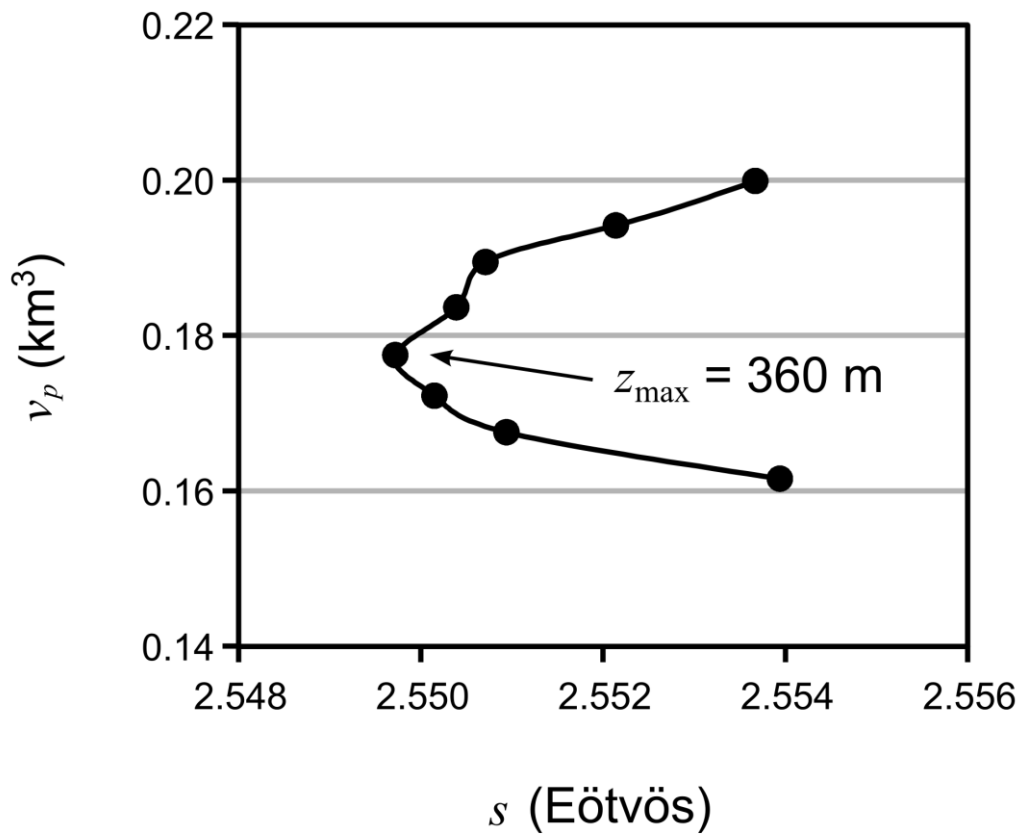


**Figure B14.** Test with synthetic data produced by a simulated salt-dome cap rock based on Ennen & Hall's (2011) work. Estimated  $v_p \times s$  curve obtained by inverting the noise-corrupted data (grey scale maps in Fig. B12) produced by the simulated salt dome cap rock shown in Fig. B13 (red wire-frame body). This curve is produced by varying the depth to the bottom  $z_{\max}$  of the interpretation model from 300 m to 440 m, in steps of 20 m. The estimated body producing the well-defined minimum  $s$  on the estimated  $v_p \times s$  curve is shown in Figs. B13(b) and (c).

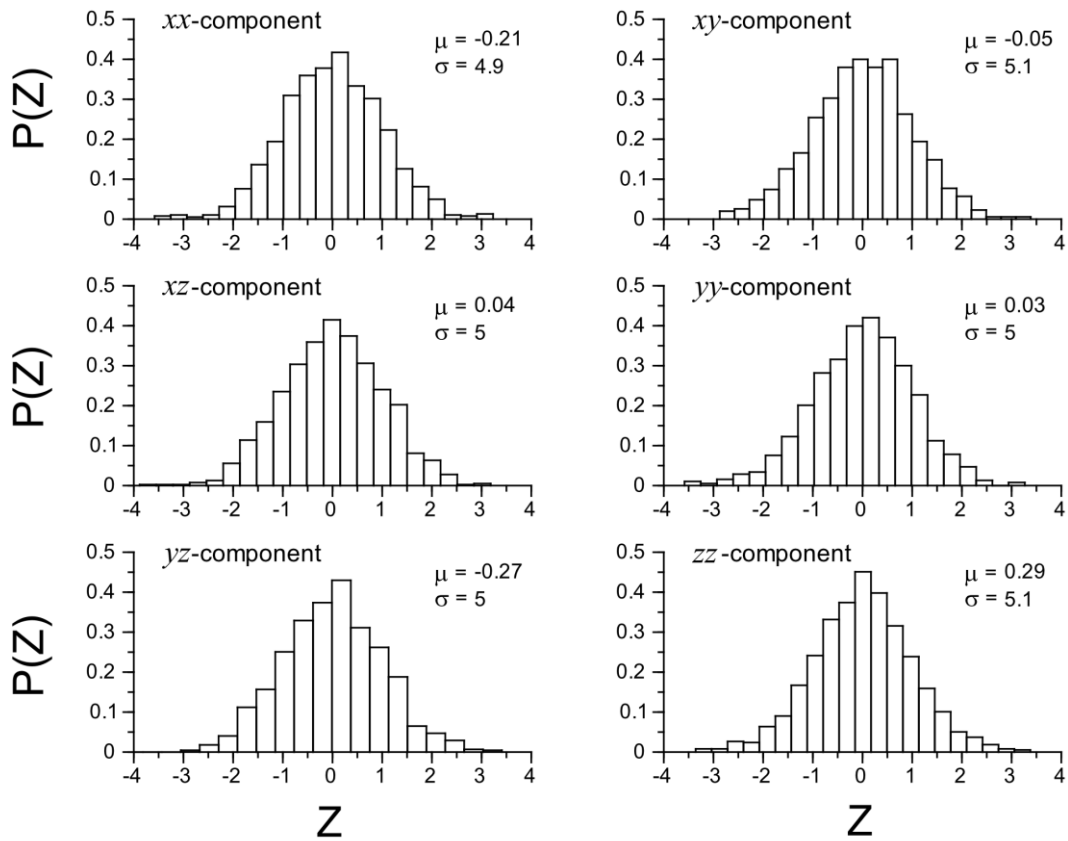


**Figure 15.** Test with synthetic data produced by a simulated salt-dome cap rock based on Ennen & Hall's (2011) work. Histograms of the residuals between the predicted data (black contour maps in Fig. B12) and the noise-corrupted data (grey scale maps in Fig. B12). The sample mean  $\mu$  and the sample standard deviation  $\sigma$  are shown in each histogram. The residuals are transformed in a dimensionless variable  $Z$  by subtracting the residual value from the sample mean  $\mu$  and then dividing the difference by the sample standard deviation  $\sigma$ .  $P(Z)$  is the frequency curve of the variable  $Z$ .

## 5.2. Cap rock model based on the prior geologic information about the Vinton salt dome and the surrounded rocks

We computed the  $xx$ -,  $xy$ -,  $xz$ -,  $yy$ -,  $yz$ - and  $zz$ - noise-corrupted components of the gravity-gradient tensor (grey scale maps in Fig. B16) produced by a synthetic body simulating a salt-dome cap rock. The data was calculated at coordinates following the same flight pattern of a real gravity-gradient survey over the Vinton salt dome, USA (Ennen & Hall, 2011). To simulate experimental errors, each component of the gravity-gradient tensor is corrupted with a pseudorandom Gaussian noise with zero mean and a different standard deviation  $\sigma$  in Eötvös (Table B1). We also simulate systematic errors by shifting each component of the gravity-gradient tensor by a different constant  $b$  in Eötvös (Table B1). The simulated body is based on the geological knowledge about the region where the Vinton salt dome, USA, is located. The simulated cap rock extends in depth from 160 m to 460 m, with density contrast  $\rho$  of 0.55 g/cm<sup>3</sup> and volume 0.366 km<sup>3</sup> (red wire-frame body in Fig. B17).

We applied our method by using an interpretation model formed by an ensemble of  $L = 10$  prisms, all of them with the true density contrast  $\rho^k = 0.55$  g/cm<sup>3</sup> ( $k = 1, \dots, 10$ ) and the same number of polygon vertices  $M^k = 16$  ( $k = 1, \dots, 10$ ), which describe the horizontal cross-sections. We also assumed the knowledge about the actual depth to the top of the simulated source, hence we set the depth to the top of the interpretation model as  $z_0 = 160$  m. The ten prisms which make up the initial approximation have the same horizontal Cartesian coordinates  $x_0^k = 1150$  m and  $y_0^k = 1606$  m,  $k = 1, \dots, 10$ , of the arbitrary origins. The radii forming the shallowest prism ( $r_j^1$ ,  $j = 1, \dots, 16$ ) are

equal to 100 m; the radii forming the second prism ( $r_j^2, j=1,\dots,16$ ) are equal to 200 m. The sizes of radii of the third prism up to the tenth prism are increased successively by adding 100 m, until the radii of the deeper prism ( $r_j^{10}, j=1,\dots,16$ ) attain 1000 m.

We construct the estimated  $v_p \times s$  curve (Fig. B18) by producing fifteen estimated sources, each one with a fixed maximum depth  $z_{\max}$  of the interpretation model. The  $z_{\max}$  varies from 300 m to 580 m, in steps of 20 m leading to an uncertainty of  $\pm 10$  m in the estimated depth to the bottom. Each one of these eight estimates produces a pair of  $s$  and  $v_p$  (black dots in Fig. B18) on the estimated  $v_p \times s$  curve. This curve presents a well-defined minimum of  $s$ , associated with  $z_{\max} = 420$  m of the interpretation model. Fig. B17 shows the initial approximation (blue prisms in Fig. B17a) and two perspective views of the estimated salt-dome cap rock (blue prisms in Figs. B17b and c) using the maximum depth  $z_{\max} = 420$  m to set up the interpretation model. Although this estimated salt-dome cap rock is associated with a well-defined minimum of  $s$  on the estimated  $v_p \times s$  curve (Fig. B18), it produces a predicted data (black contour maps in Fig. B16) that do not fit acceptably the noise-corrupted gravity-gradient data (grey scale maps in Fig. B16). This aspect is confirmed by the histograms (Fig. B19) of the residuals between the predicted (black contour maps in Fig. B16) and the simulated (grey scale maps in Fig. B16) noise-corrupted gravity-gradient data. These histograms resemble bell-shaped patterns indicating that the residuals of all components follow normal distributions. Moreover, the sample standard deviations  $\sigma$  calculated from the

residuals (Fig. B19) are very close to the standard deviations  $\sigma$  (Table B1) of the pseudorandom Gaussian noise realizations added to the synthetic data aiming at simulating experimental errors. However, the sample means  $\mu$  calculated from the residuals (Fig. B19) are not close to zero, indicating that the predicted data do not fit the synthetic data which were corrupted by with pseudorandom zero-mean Gaussian noise. Notice that the absolute values of these sample means  $\mu$  (Fig. B19) are very close to the absolute values of the constants  $b$  (Table B1) that were added to the synthetic data aiming at simulating systematic errors. The most striking feature of these histograms (Fig. B19) is that they correctly characterize both the experimental and the systematic errors. Hence, by using these histograms, we can correct the systematic errors from the data. This correction consists in adding each sample non-zero mean  $\mu$  calculated from the residuals (Fig. B19) to the corresponding component of the synthetic gravity-gradient data (grey scale maps in Fig. B16). This data preprocessing to correct systematic errors leads to a new set of components of the gravity-gradient data shown in Fig. B20 (grey scale maps). By inverting these corrected gravity-gradient data, we recalculate the estimated  $v_p \times s$  (Fig. B21). This new  $v_p \times s$  curve shows a well-defined minimum of  $s$  associated with  $z_{\max} = 460$  m of the interpretation model. Figs. B22(b) and (c) show the perspective views of the estimated salt-dome cap rock (blue prisms) using the maximum depth  $z_{\max} = 460$  m to set up the interpretation model. This estimate is obtained by using the initial approximation (blue prisms) shown in Fig. B22(a). Notice that the estimated salt-dome cap rock (blue prisms in Figs. B22b and c) completely retrieves the geometry of the simulated source (red wire-frame body shown in Figs. B17 and B22), with the correct depth to the

bottom ( $z_{\max} = 460$  m) and a volume of  $v_p = 0.372$  km<sup>3</sup>, which is very close to the true one (0.366 km<sup>3</sup>). The predicted data (black contour maps in Fig. B20) produced by this new estimated salt-dome cap rock fit acceptably the corrected gravity-gradient data (grey scale maps in Fig. B20). The histograms of the residuals (Fig. B23) corroborate the acceptance of the data fitting. In contrast with the histograms in Fig. B19, that show sample non-zero means, the sample means  $\mu$  calculated from the new residuals (Fig. B23) are close to zero, indicating that the systematic errors were successfully removed from the data. These results show that our method is able to completely recover the geometry of a salt-dome cap rock, even in the presence of systematic errors in the data.

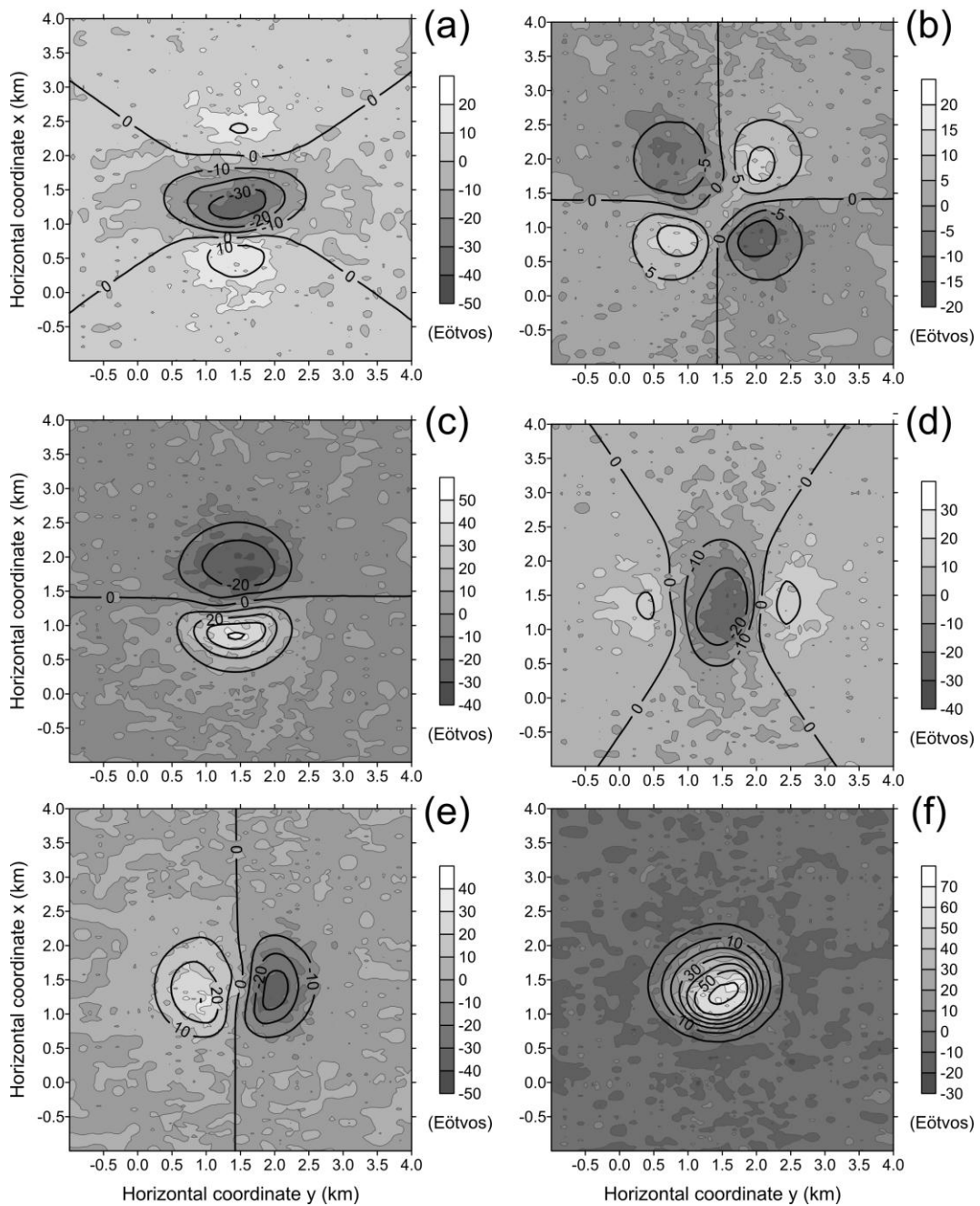


**Figure B16.** Test with synthetic data produced by a simulated salt-dome cap rock based on the geologic knowledge at the Vinton salt dome's region. Synthetic noise-corrupted (grey scale maps) and predicted (black contour maps) of the (a)  $xx$ -, (b)  $xy$ -, (c)  $xz$ -, (d)  $yy$ -, (e)  $yz$ - and (f)  $zz$ -components of the gravity gradient tensor. The synthetic components are produced by the simulated salt-dome cap rock shown in Fig. B17 (red wire-frame body). The predicted components are produced by the estimated body shown in Figs. B17(b) and (c) (blue prisms).

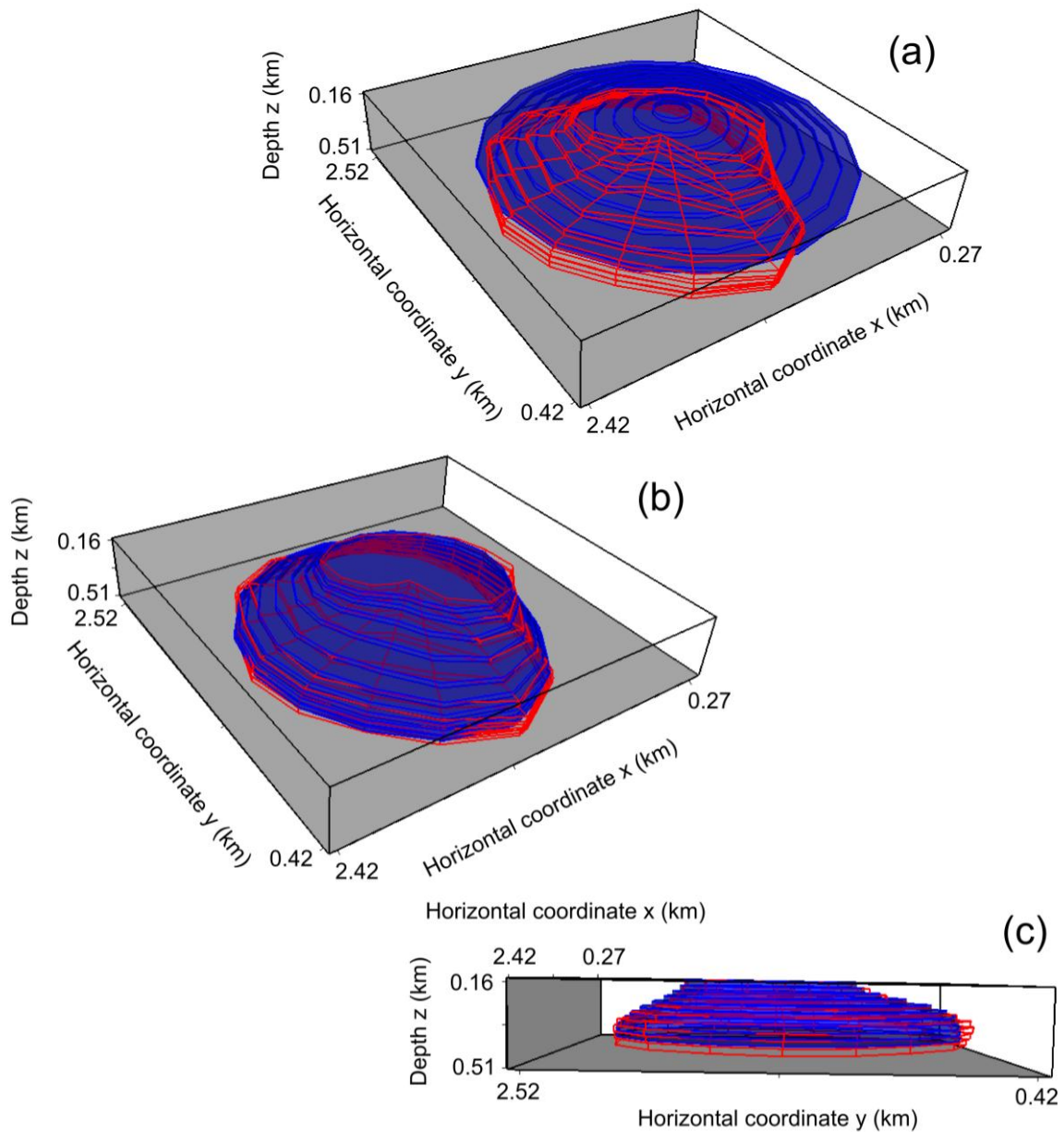


**Figure B17.** Test with synthetic data produced by a simulated salt-dome cap rock based on the geologic knowledge about the Vinton salt dome's region. Perspective views of the simulated salt-dome cap rock (red wire-frame body) with depth to the bottom at 460 m and volume 0.372 km<sup>3</sup>. Perspective views in blue prisms of the (a) initial approximation, (b) and (c) estimated body. The simulated salt-dome cap rock (red wire-frame body) is based on the geologic knowledge at the region where the Vinton salt dome, USA, is located. The estimated body in (b) and (c) is obtained by inverting the noise-corrupted data shown in Fig. B16 (grey scale maps) and assuming an interpretation model with depth to the bottom  $z_{\max} = 420$  m. The estimated body has a predicted volume  $v_p = 0.326$  km<sup>3</sup> and produces the predicted gravity-gradient data shown in Fig. B16 (black contour maps).

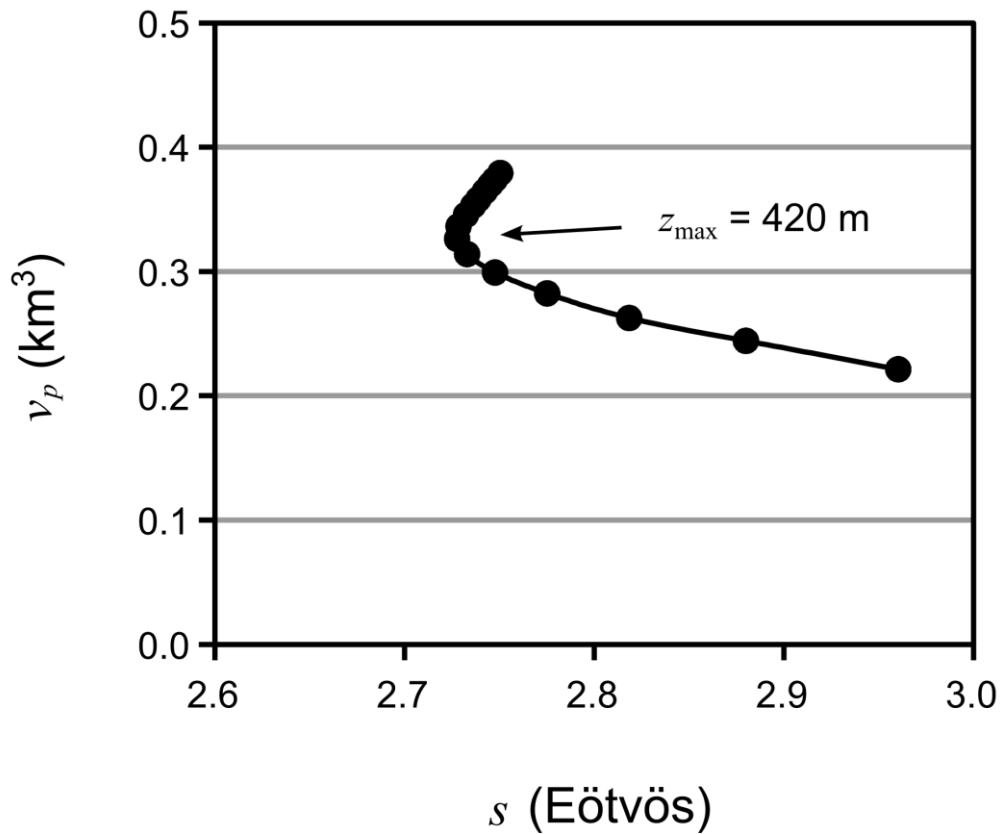


**Figure B18.** Test with synthetic data produced by a simulated salt-dome cap rock based on the geologic knowledge about the Vinton salt dome's region. Estimated  $v_p \times s$  curve obtained by inverting the noise-corrupted data (grey scale maps in Fig. B16) produced by the simulated salt dome cap rock shown in Fig. B17 (red wire-frame body). This curve is produced by varying the depth to the bottom  $z_{\max}$  of the interpretation model from 300 m to 580 m, in steps of 20 m. The estimated body with  $z_{\max} = 420$  m produces the well-defined minimum  $s$  on the estimated  $v_p \times s$  curve and it is shown in Figs. B17(b) and (c).

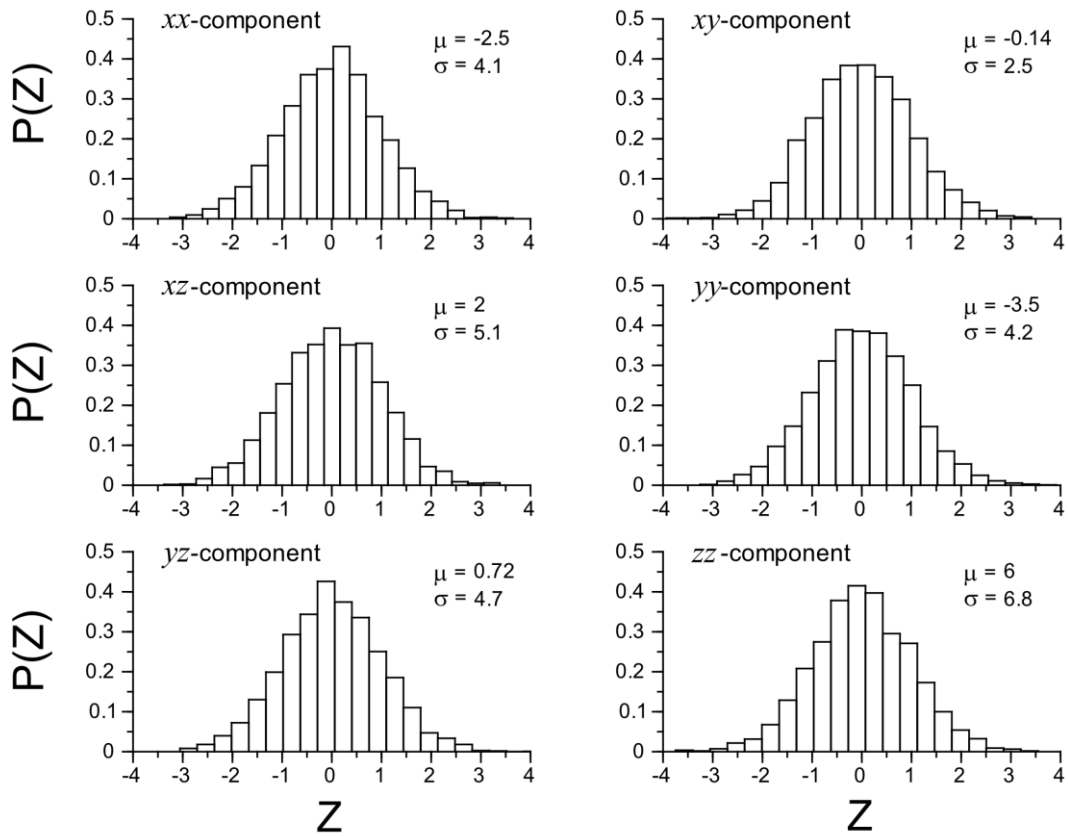


**Figure B19.** Test with synthetic data produced by a simulated salt-dome cap rock based on the geologic knowledge about the Vinton salt dome's region. Histograms of the residuals between the predicted data (black contour maps in Fig. B16) and the noise-corrupted data (grey scale maps in Fig. B16). The sample mean  $\mu$  and the sample standard deviation  $\sigma$  are shown in each histogram. The residuals are transformed in a dimensionless variable  $Z$  by subtracting the residual value from the sample mean  $\mu$  and then dividing the difference by the sample standard deviation  $\sigma$ .  $P(Z)$  is the frequency curve of the variable  $Z$ .

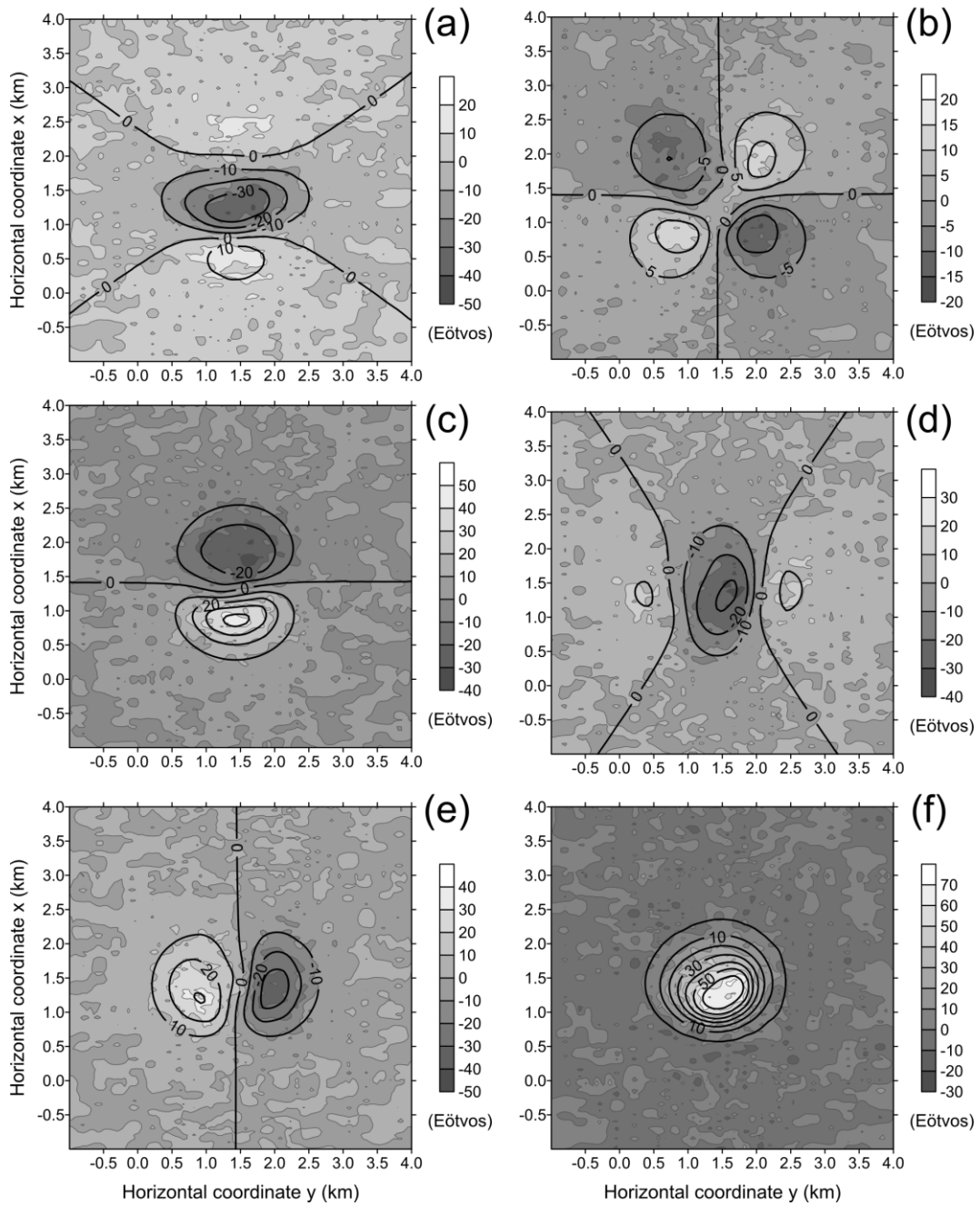


**Figure B20.** Test with synthetic data produced by a simulated salt-dome cap rock based on the geologic knowledge about the Vinton salt dome's region. Synthetic noise-corrupted data (grey scale maps) corrected for the effect of systematic errors (Table B1) and predicted data (black contour maps) of the (a)  $xx$ -, (b)  $xy$ -, (c)  $xz$ -, (d)  $yy$ -, (e)  $yz$ - and (f)  $zz$ - components of the gravity gradient tensor. The systematic errors are removed by adding the sample means of the residuals ( $\mu$  in Fig. B19) to the original noise-corrupted data shown in Fig. B16 (grey scale maps). The predicted components are produced by the estimated body (blue prisms in Figs B22b and c).

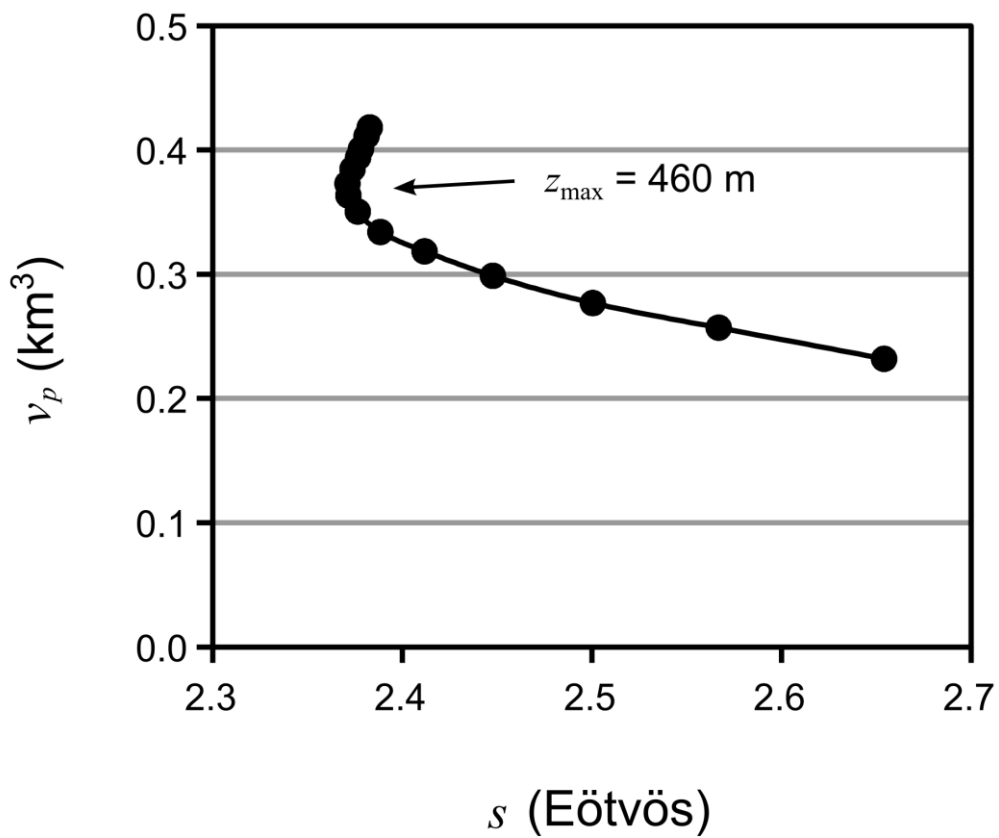


**Figure 21.** Test with synthetic data produced by a simulated salt-dome cap rock based on the geologic knowledge about the Vinton salt dome's region. Estimated  $v_p \times s$  curve obtained by inverting the corrected noise-corrupted data (grey scale maps in Fig. B20) produced by the simulated salt-dome cap rock (red wire-frame body in Figs. B17 and B22). This curve is produced by varying the depth to the bottom  $z_{\max}$  of the interpretation model from 300 m to 580 m, in steps of 20 m. The estimated body with  $z_{\max} = 460$  m produces the well-defined minimum of  $s$  on the estimated  $v_p \times s$  curve and is shown in Figs. B22(b) and (c) (blue prisms).

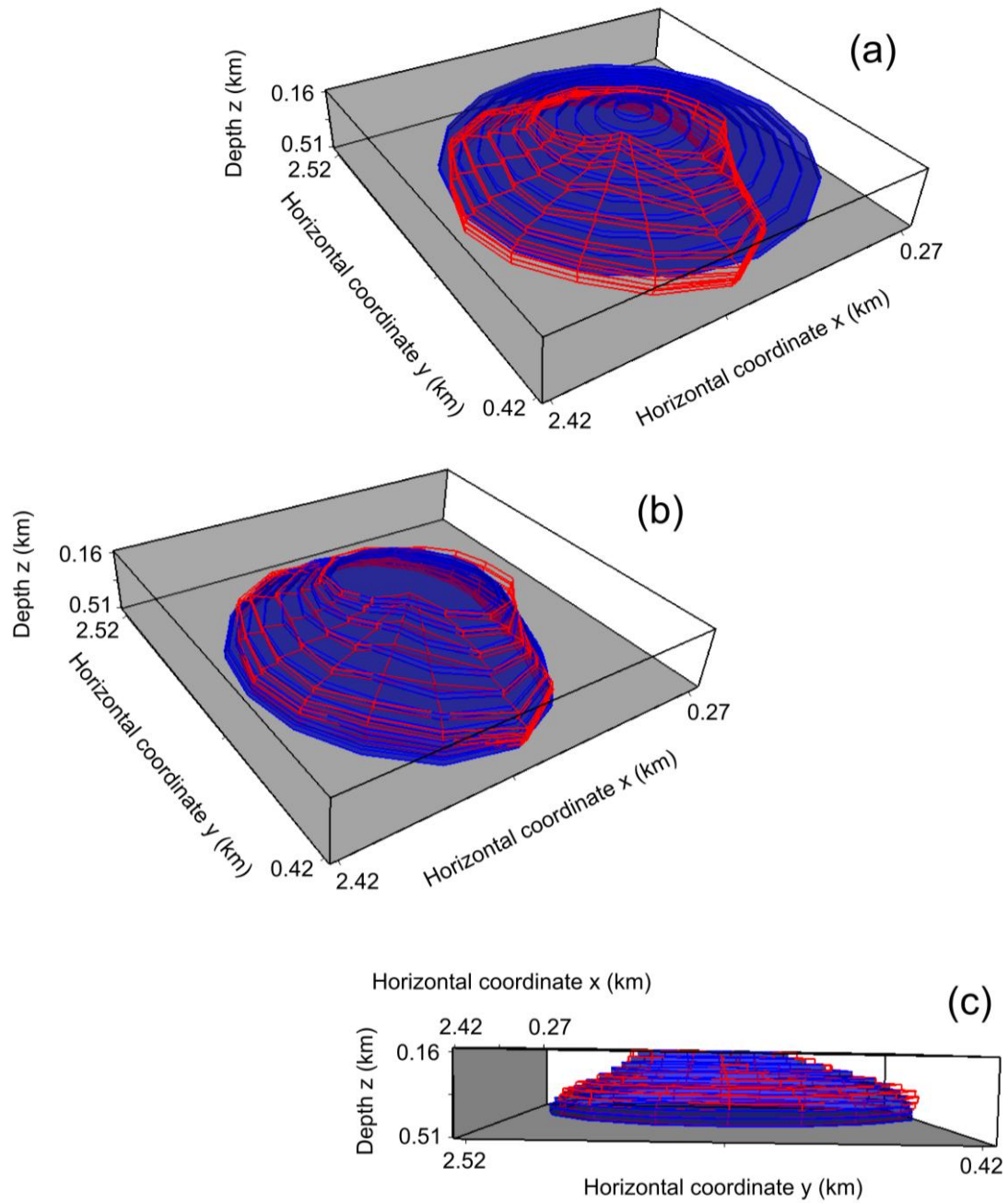


**Figure 22.** Test with synthetic data produced by a simulated salt-dome cap rock based on the geologic knowledge about the Vinton salt dome's region. Perspective views of the simulated salt-dome cap rock (red wire-frame body) with depth to the bottom at 460 m and volume  $0.366 \text{ km}^3$ . Perspective views (blue prisms) of the (a) initial approximation, (b) and (c) estimated body. The estimated body in (b) and (c) is obtained by inverting the corrected noise-corrupted data shown in Fig. B20 (grey scale maps) and assuming an interpretation model with depth to the bottom  $z_{\max} = 460 \text{ m}$ . The estimated body has a predicted volume  $v_p = 0.372 \text{ km}^3$  and produces the predicted gravity-gradient data shown in Fig. B20 (black contour maps).

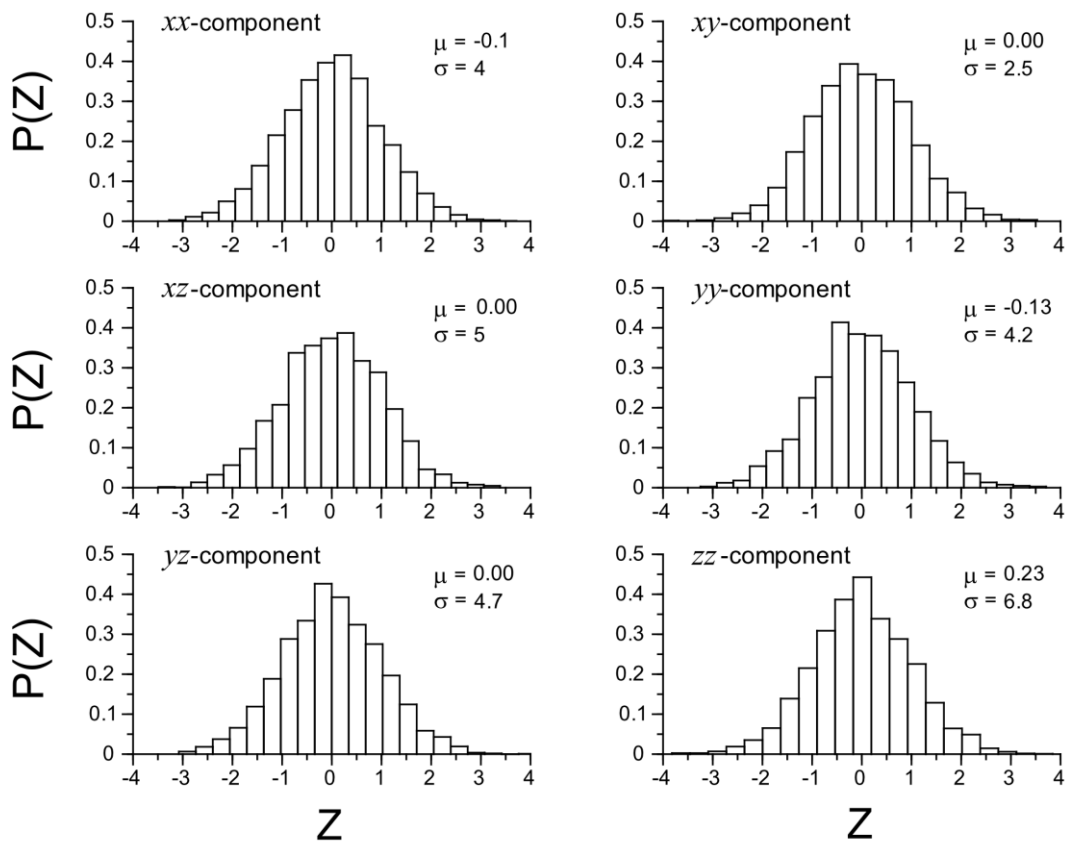


**Figure 23.** Test with synthetic data produced by a simulated salt-dome cap rock based on the geologic knowledge about the Vinton salt dome's region. Histograms of the residuals between the predicted data (black contour maps in Fig. B20) and the corrected noise-corrupted data (grey scale maps in Fig. B20). The sample mean  $\mu$  and the sample standard deviation  $\sigma$  are shown in each histogram. The residuals are transformed in a dimensionless variable  $Z$  by subtracting the residual value from the sample mean  $\mu$  and then dividing the difference by the sample standard deviation  $\sigma$ .  $P(Z)$  is the frequency curve of the variable  $Z$ .

**Table B1.** Test with synthetic data produced by a simulated salt-dome cap rock. Each component of the gravity-gradient tensor shown in Fig. B16 (grey scale maps) is corrupted with a pseudorandom Gaussian noise with zero mean and a standard deviation  $\sigma$ , simulating experimental errors. Additionally, a constant  $b$  is added to each component of the gravity-gradient tensor to simulate systematic errors.

gravity-gradient component	$\sigma$ (Eötvös)	$b$ (Eötvös)
$xx$	4.00	2.60
$xy$	2.50	0.14
$xz$	5.10	-2.00
$yy$	4.10	3.60
$yz$	4.70	-0.72
$zz$	6.80	-6.20

## 6. APPLICATION TO REAL DATA

We applied our method to interpret the Full Tensor Gravity Gradiometry (FTG) data acquired by Bell Geospace Inc. over the Vinton salt dome, at southwestern Louisiana, USA (grey scale maps in Fig. B24). The gravity-gradient data were terrain corrected using a density of  $2.2 \text{ g/cm}^3$ . This salt dome is located in the onshore Gulf of Mexico, which is considered an important region producing oil and gas for more than one century (Coker *et al.*, 2007; Ennen & Hall, 2011). According to Coker *et al.* (2007), the Vinton salt dome is characterized by a massive cap rock extending above the salt rock. This cap rock is formed by gypsum and anhydrite which is embedded in sediments characterized by intercalated layers of sandstone and shale. Fig. B25 shows the density ranges of the principal rocks and minerals (Telford *et al.* 1990) present on the lithologies found in the study area. Following Ennen & Hall (2011), we assumed that the cap rock has a depth of the top at 160 m. Based on the density ranges of the lithologies (Fig. B25), we assumed that the surrounding sediments (shale and sandstone) and the salt dome have the same density  $2.2 \text{ g/cm}^3$ . This implies that the observed gravity-gradient data (grey scale maps in Fig. B24) are predominantly caused by the cap rock.

We applied our method to estimate the 3-D geometry of the cap rock. We tested a geologic hypothesis about the Vinton salt dome and adjacent rocks in which the cap rock has the density  $\rho = 2.75 \text{ g/cm}^3$  (based on Ennen & Hall, 2011), resulting in a density contrast of  $0.55 \text{ g/cm}^3$  with the host rocks. Notice that this possible density of the cap rock is within the density ranges shown in Fig. B25. To test this hypothesis, we applied our method by using an

interpretation model with density contrast equal to  $0.55 \text{ g/cm}^3$ . The interpretation model is formed by an ensemble of  $L = 10$  prisms, each one with the same number of polygon vertices  $M^k = 16$  ( $k = 1, \dots, 10$ ) describing the horizontal cross-sections. Based on the prior information, we also assumed the knowledge about the actual depth to the top of the cap rock, hence we set the depth to the top of all interpretation models as  $z_0 = 160 \text{ m}$ . The ten prisms which make up the used initial approximation has the same horizontal Cartesian coordinates of  $x_0^k = 3334150 \text{ m}$  and  $y_0^k = 442606 \text{ m}$ ,  $k = 1, \dots, 10$ . Based on the synthetic application to interpret a simulated cap rock (Subsection 5.2), the radii forming the shallowest prism ( $r_j^1$ ,  $j = 1, \dots, 16$ ) are equal to  $100 \text{ m}$  and the radii forming the second prism ( $r_j^2$ ,  $j = 1, \dots, 16$ ) are equal to  $200 \text{ m}$ . The sizes of radii of the third prism up to the tenth prism are increased successively by adding  $100 \text{ m}$ , until the radii of the deeper prism ( $r_j^{10}$ ,  $j = 1, \dots, 16$ ) attain  $1000 \text{ m}$ . We construct the estimated  $v_p \times s$  curve (Fig. B26) formed by 15 pairs of  $s$  and  $v_p$  (black dots), each one produced by an estimated 3-D source with a different maximum depth to the bottom  $z_{\max}$  of the interpretation model. The value of  $z_{\max}$  varies from  $300 \text{ m}$  to  $580 \text{ m}$ , in steps of  $20 \text{ m}$ , leading to an uncertainty of  $\pm 10 \text{ m}$  in the estimated depth to the bottom. The estimated  $v_p \times s$  curve (Fig. B26) presents a well-defined minimum of  $s$  associated with an estimated 3-D cap rock (not shown) having maximum depth to the bottom  $z_{\max} = 440 \text{ m}$  and a predicted volume  $v_p = 0.327 \text{ km}^3$ . This estimated 3-D cap rock (not shown) produces a predicted data (black contour maps in Fig. B24) that do not fit acceptably the observed gravity-gradient data (grey scale maps in Fig. B24).

Similar to the results shown in the Subsection 5.2, the histograms (Fig. B27) of the residuals between the predicted and the observed gravity-gradient data confirm the unacceptable data fittings, because of the sample non-zero means  $\mu$  (Fig. B27). These sample non-zero means  $\mu$  (Fig. B27) are calculated from the residuals and they are revealing the presence of systematic errors in the observed data (grey scale maps in Fig. B24). By adding each sample non-zero mean  $\mu$  (Fig. B27) to the corresponding component of the gravity-gradient data (grey scale maps in Fig. B24), we produce corrected components of the gravity-gradient data (grey scale maps in Fig. B28). By inverting these corrected gravity-gradient data, we repeat the procedure for calculating a new estimated  $v_p \times s$  curve (Fig. B29). This curve shows a well-defined minimum of  $s$  associated with  $z_{\max} = 460$  m of the interpretation model. The estimated 3-D cap rock (Figs B30b and c) producing the minimum of  $s$  on the estimated  $v_p \times s$  curve (Fig. B29) has a maximum depth  $z_{\max} = 460$  m and a predicted volume  $v_p = 0.366$  km<sup>3</sup>. Fig. B30(a) shows the initial approximation used in this inversion. This 3-D estimated salt-dome cap rock (Figs. B30b and c) yields acceptable data fittings, which are confirmed by the histograms of the residuals shown in Fig. B31. The predicted data (black contour maps) are shown in Fig. B28.

The upper part of our estimated salt-dome cap rock (Figs. B30b and c) has a northeast-southwest elongated form, being consistent with the strike of the main fault in the study area (Coker *et al.*, 2007). We stress that this estimate represents a possible 3-D source that fits the observed gravity-gradient data over the Vinton salt dome, within the experimental errors. So, this estimated can

be accepted as a possible geometry of the salt-dome cap rock. To confirm this estimated geometry, more prior geologic information about the Vinton salt dome and the surrounded rocks must be introduced.

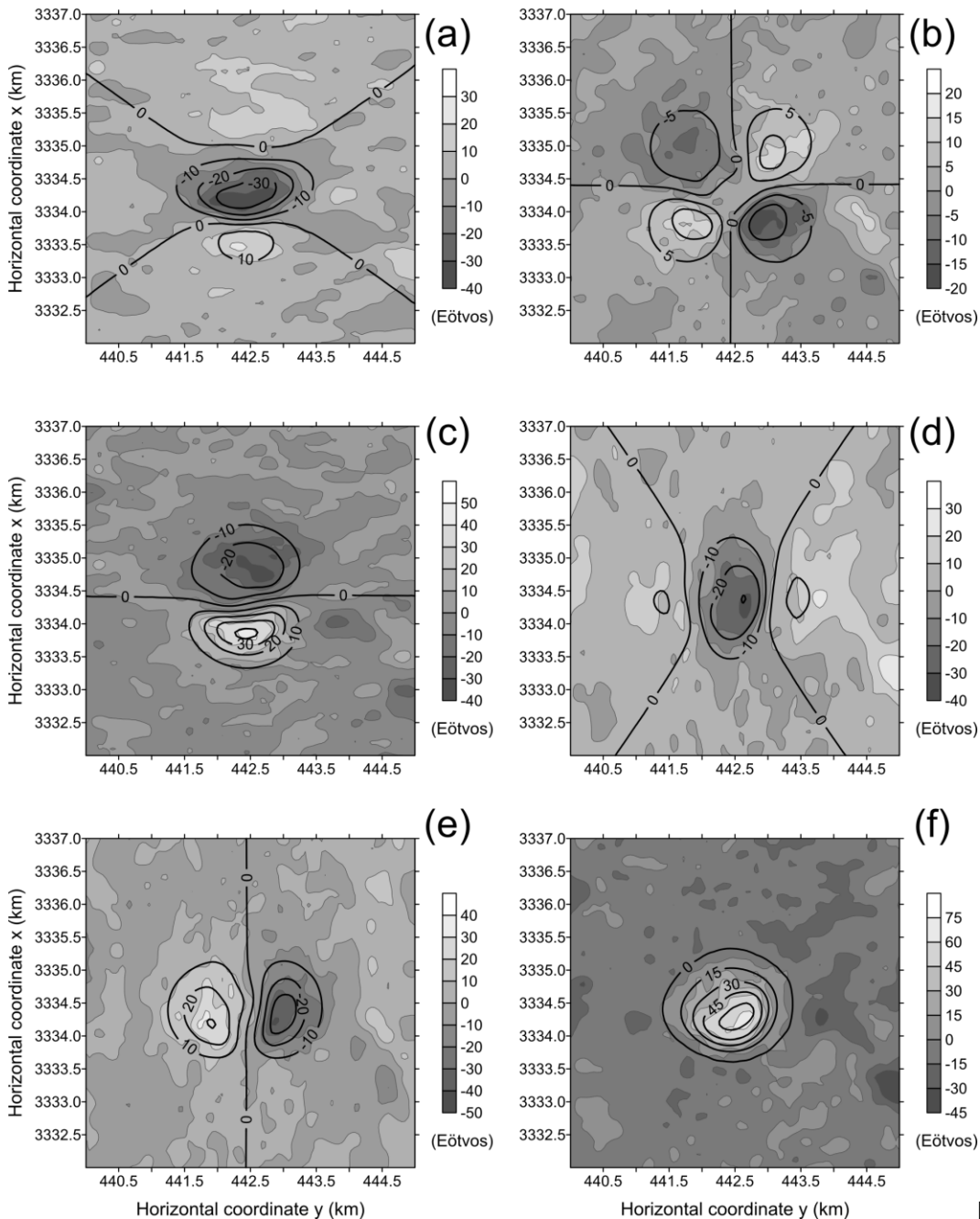


**Figure B24.** Interpretation of real data over the Vinton salt dome, USA. Observed (grey scale maps) and predicted (black contour maps) of the (a)  $xx$ -, (b)  $xy$ -, (c)  $xz$ -, (d)  $yy$ -, (e)  $yz$ - and (f)  $zz$ -components of the gravity-gradient tensor. The observed data are terrain corrected by using a density of  $2.20 \text{ g/cm}^3$ . The predicted data are produced by an estimated body (not shown).

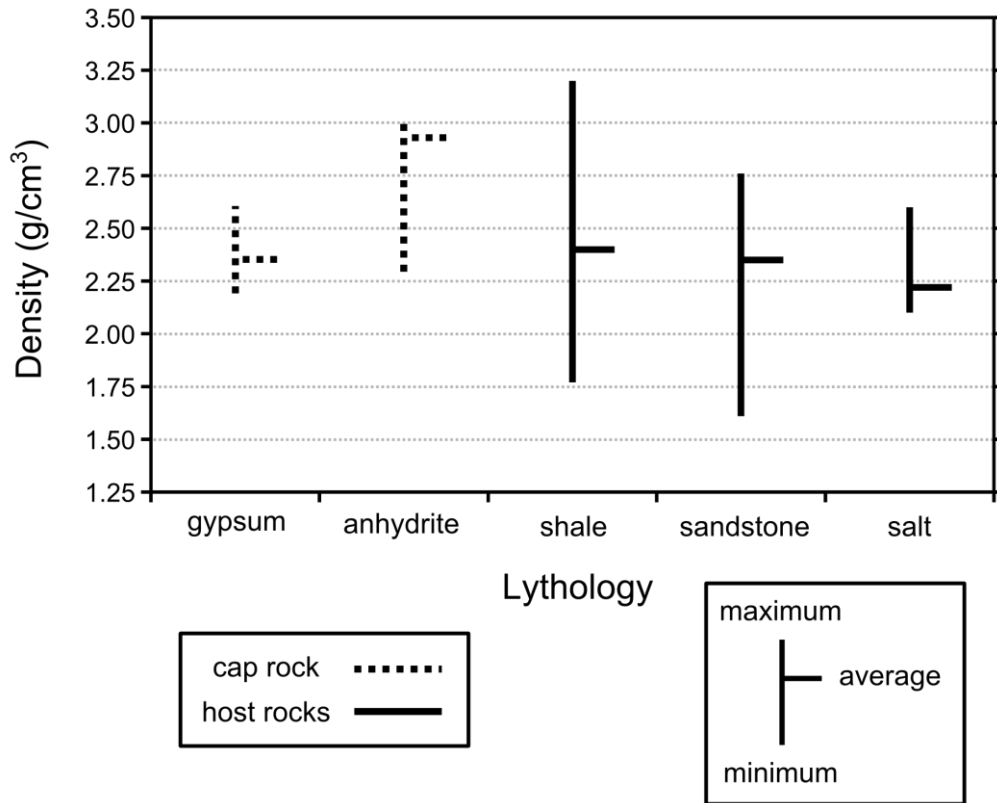


**Figure B25.** Interpretation of real data over the Vinton salt dome, USA. The graph shows the density ranges and the average values of the rock types and minerals according to Telford *et al.* (1990). These lithologies are identified in the studied geologic setting reported by Ennen & Hall (2011).

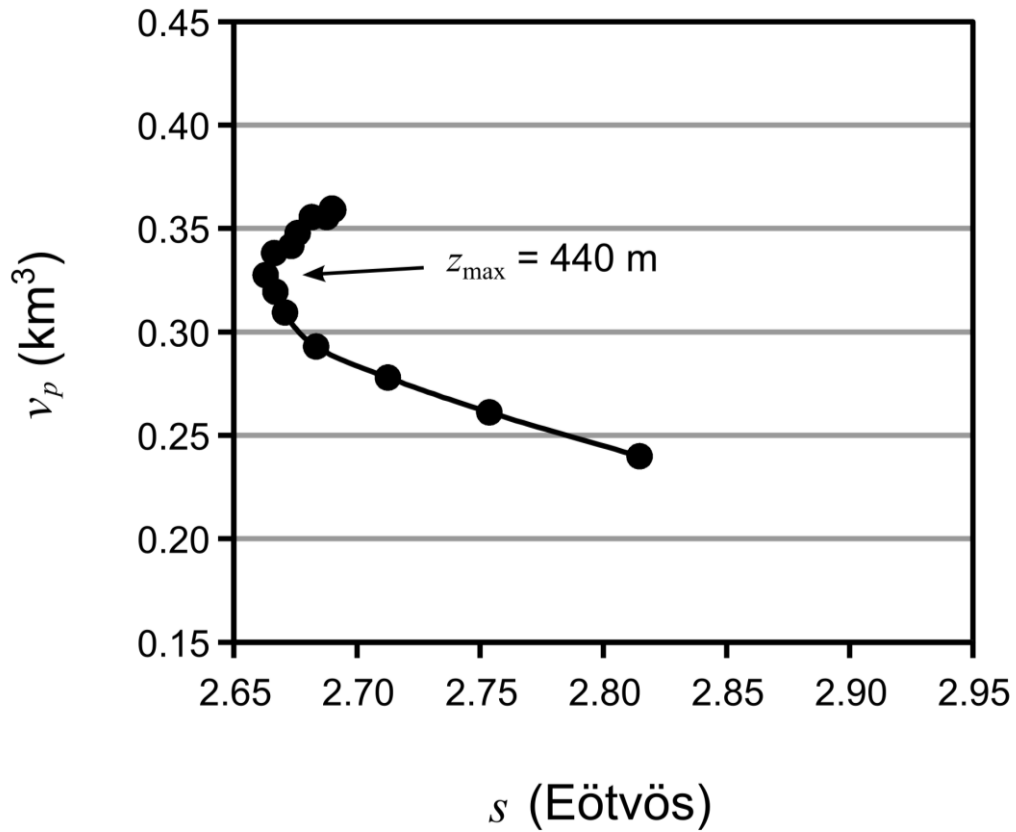


**Figure B26.** Interpretation of real data over the Vinton salt dome, USA. Estimated  $v_p \times s$  curve obtained by inverting the real data shown in Fig. B24 (grey scale maps). This curve is constructed by varying the depth to the bottom  $z_{\max}$  of the interpretation model from 300 m to 580 m, in steps of 20 m. The estimated body (not shown) producing the well-defined minimum of  $s$  on this  $v_p \times s$  curve has a maximum depth to the bottom  $z_{\max} = 440$  m and a predicted volume  $v_p = 0.327 \text{ km}^3$ .

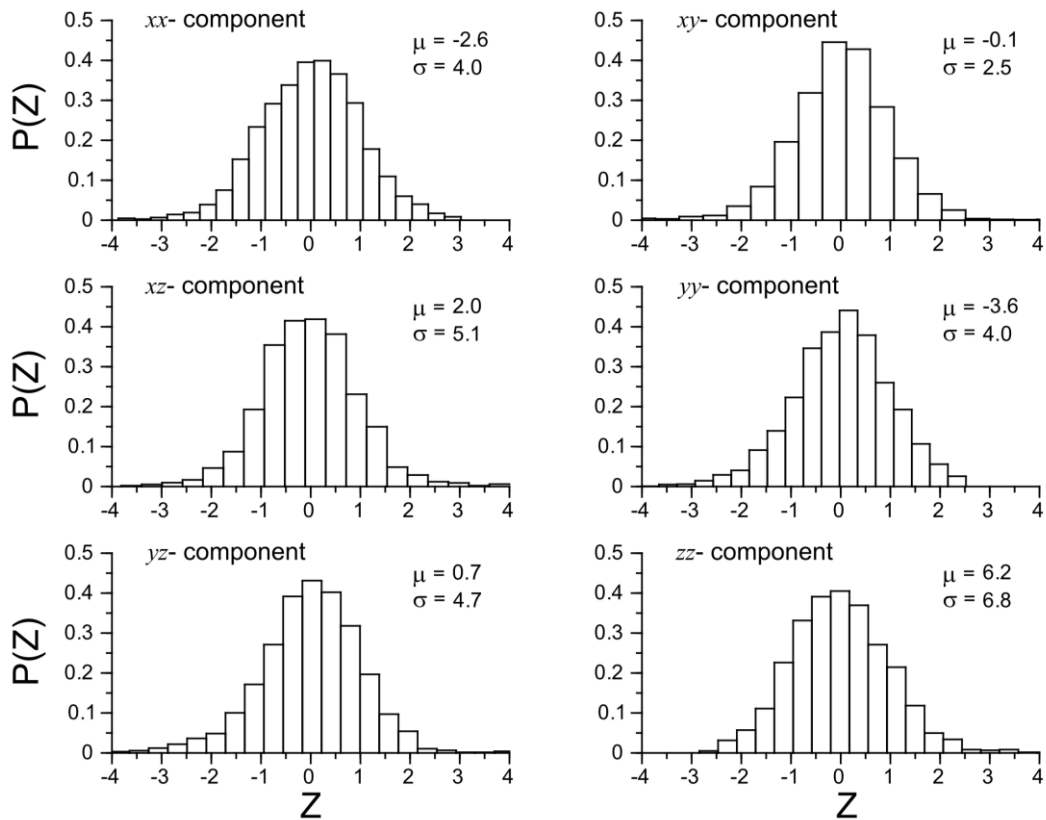


**Figure B27.** Interpretation of real data over the Vinton salt dome, USA. Histograms of the residuals between the predicted data (black contour maps in Fig. B24) and the real data (grey scale maps in Fig. B24). The sample mean  $\mu$  and the sample standard deviation  $\sigma$  are shown in each histogram. The residuals are transformed in a dimensionless variable  $Z$  by subtracting the residual value from the sample mean  $\mu$  and then dividing the difference by the sample standard deviation  $\sigma$ .  $P(Z)$  is the frequency curve of the variable  $Z$ .

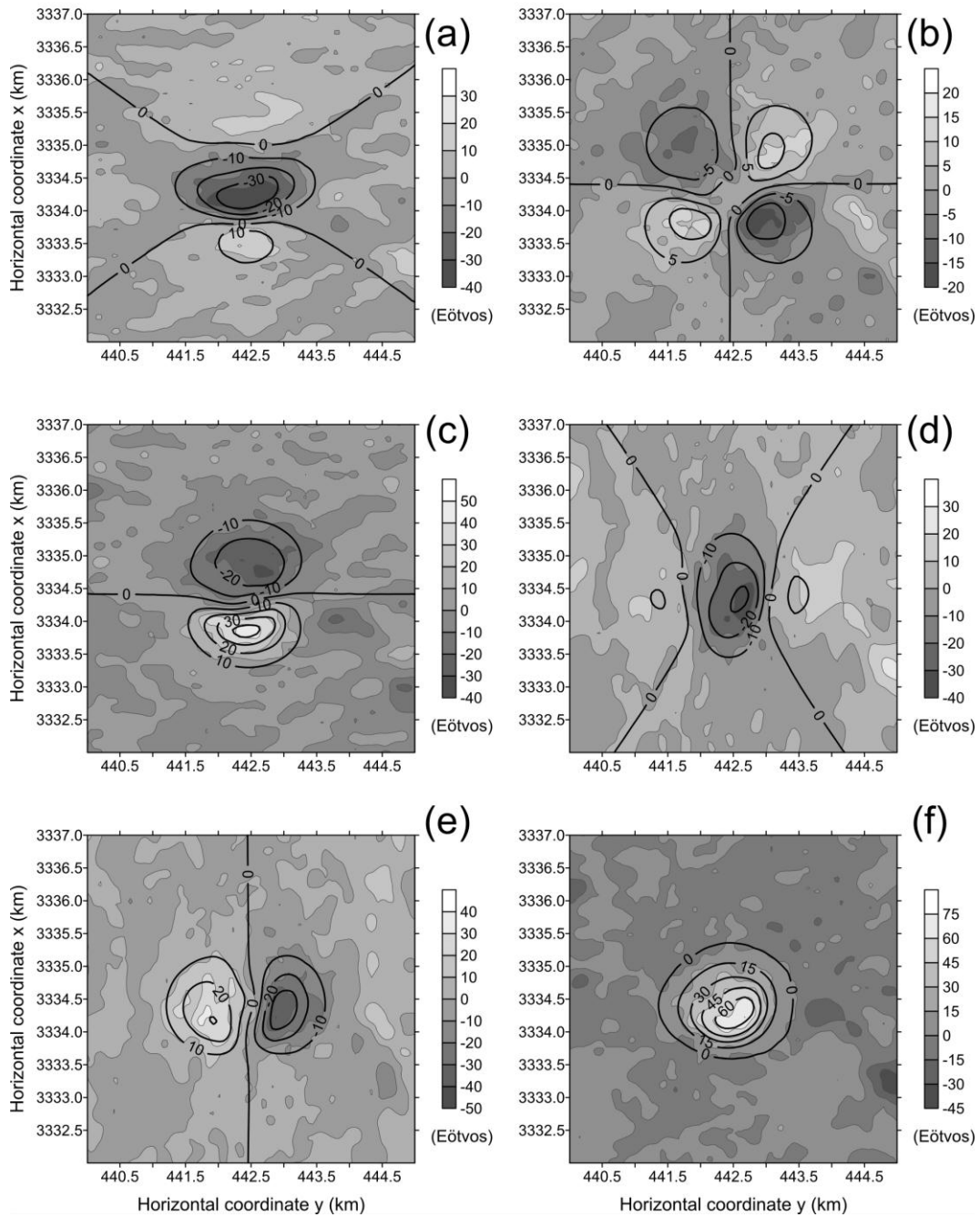


**Figure B28.** Interpretation of real data over the Vinton salt dome, USA. Real data (grey scale maps) corrected for the effect of systematic errors and predicted data (black contour maps) of the (a)  $xx$ -, (b)  $xy$ -, (c)  $xz$ -, (d)  $yy$ -, (e)  $yz$ - and (f)  $zz$ - components of the gravity-gradient tensor. The systematic errors are removed by adding the sample means of the residuals ( $\mu$  in Fig. B27) to the original real data shown in Fig. B24 (grey scale maps). The predicted components are produced by the estimated body (Figs. B30b and c).

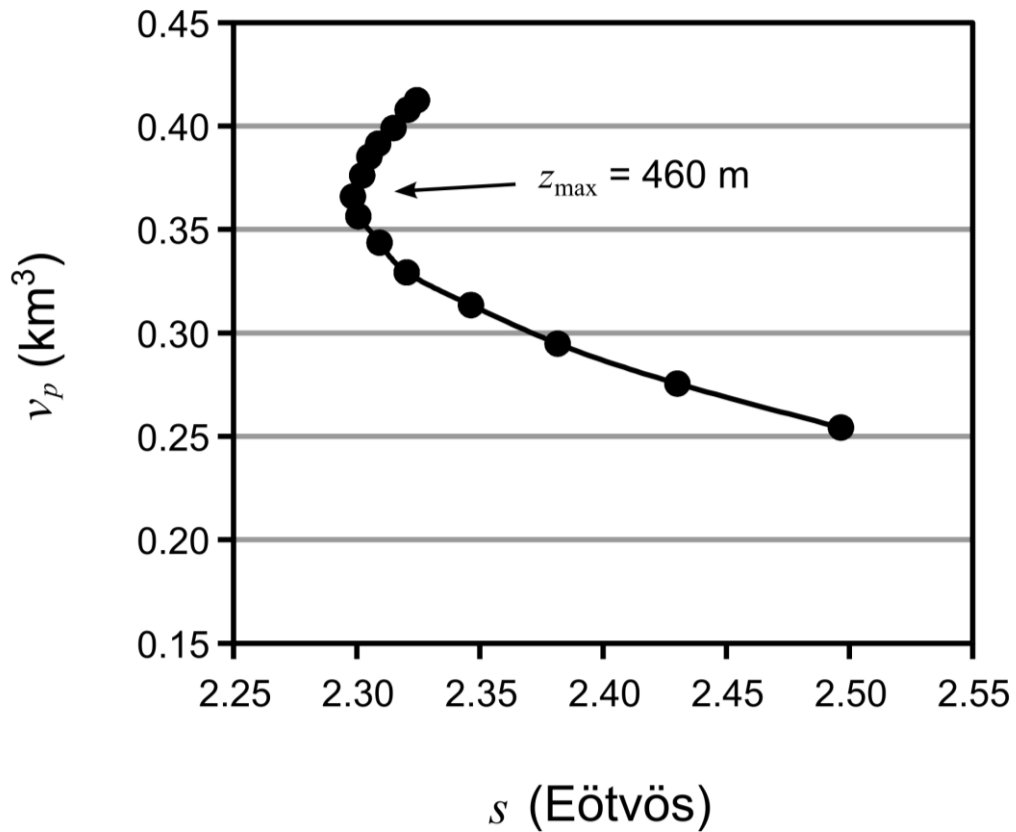


**Figure B29.** Interpretation of real data over the Vinton salt dome, USA. Estimated  $v_p \times s$  curve obtained by inverting the corrected real data shown in Fig. B28 (grey scale maps). This curve is constructed by varying the depth to the bottom  $z_{\max}$  of the interpretation model from 300 m to 580 m, in steps of 20 m. The estimated body (Figs B30b and c) producing the well-defined minimum of  $s$  on this  $v_p \times s$  curve has a maximum depth to the bottom  $z_{\max} = 460$  m and a predicted volume  $v_p = 0.366 \text{ km}^3$ .

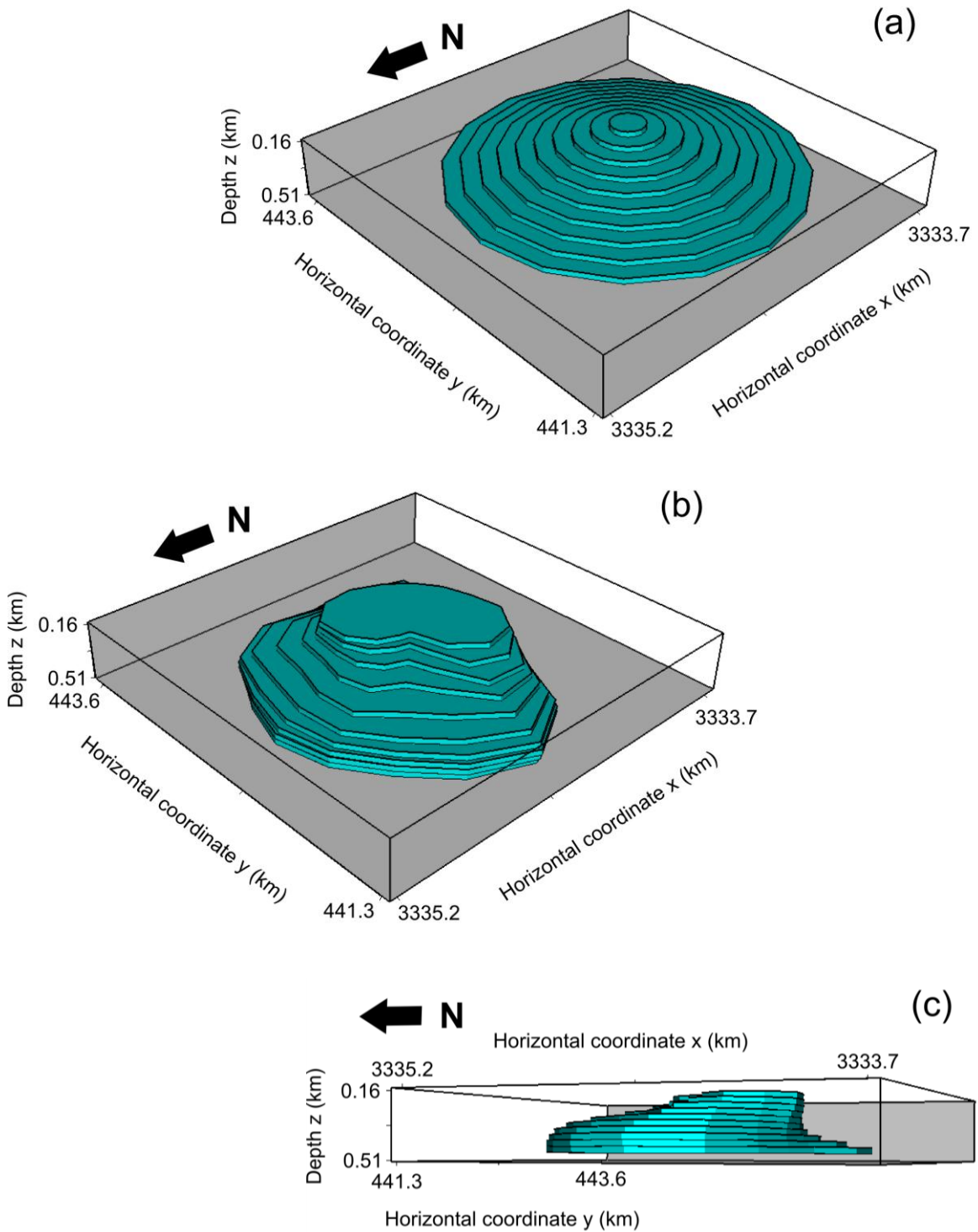


**Figure B30.** Interpretation of real data over the Vinton salt dome, USA. Perspective views of the (a) initial approximation, (b) and (c) estimated body. The estimated body in (b) and (c) is obtained by inverting the corrected real data shown in Fig. B28 (grey scale maps) and assuming an interpretation model with depth to the bottom  $z_{\max} = 460$  m. The estimated body has a predicted volume  $v_p = 0.366$  km<sup>3</sup> and produces the predicted gravity gradient data (black contour maps in Fig. B28).

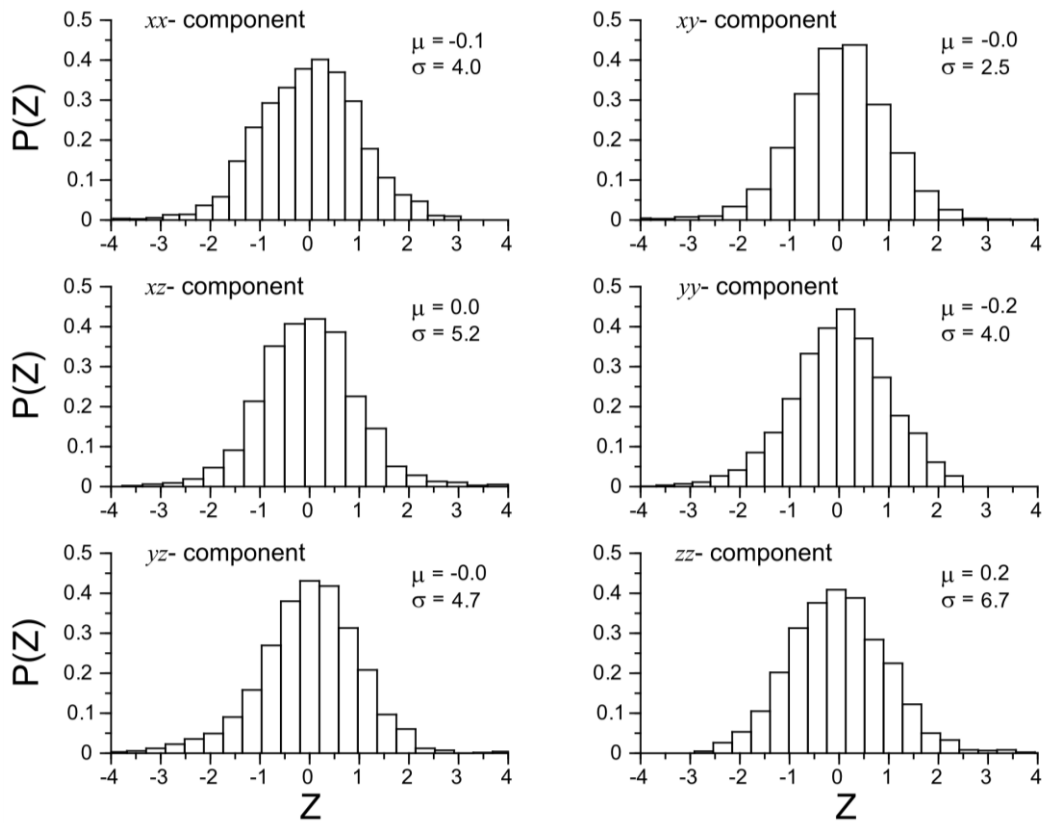


**Figure B31.** Interpretation of real data over the Vinton salt dome, USA. Histograms of the residuals between the predicted data (black contour maps in Fig. B28) and the corrected real data (grey scale maps in Fig. B28). The sample mean  $\mu$  and the sample standard deviation  $\sigma$  are shown in each histogram. The residuals are transformed in a dimensionless variable  $Z$  by subtracting the residual value from the sample mean  $\mu$  and then dividing the difference by the sample standard deviation  $\sigma$ .  $P(Z)$  is the frequency curve of the variable  $Z$ .

## 7. CONCLUSIONS

We present a new gravity-gradient inversion for estimating the shape of an isolated 3-D geologic body, given its depth to the top and density contrast. Our method approximates the geologic body by an ensemble of 3-D right prisms which are juxtaposed in the vertical direction. All prisms have the same known thickness and a polygonal horizontal cross-section defined by the same known fixed number of vertices, which are equally spaced from  $0^\circ$  to  $360^\circ$ . The horizontal positions of these vertices are described in polar coordinates referred to an arbitrary origin located inside the polygon. By estimating the horizontal Cartesian coordinates of the arbitrary origins and the radii associated with all vertices defining the horizontal cross-section of each prism, our method retrieves the geometry of depth slices of the 3-D geologic body. This estimate is formulated as a non-linear constrained inverse problem. By inverting the same gravity-gradient data set, our method can obtain different estimates produced by interpretation models with different maximum depths. This is a consequence of the fundamental ambiguity involving the product of a physical property and a volume in the interpretation of potential-field data. To deal with this ambiguity and reduce the class of possible 3-D estimates compatible with the gravity-gradient data, we used a criterion based on the relationship between the  $\ell - 1$  norm of the residuals  $s$  and the volume  $v_p$  of different estimates obtained by using interpretation models with different maximum depths. The estimated  $v_p$  and  $s$  produced by each one of these estimates are plotted one against another, forming an estimated  $v_p \times s$  curve. On this curve, the estimate producing the minimum  $s$  and fitting the gravity-gradient data is chosen as the

*optimum* choice of the bottom's depth of the source. If the estimated  $v_p \times s$  curve shows a well-defined minimum of  $s$ , the gravity-gradient data have sufficient resolution for recover the geometry of the 3-D geologic body with both the correct volume and the correct maximum depth to the bottom. In contrast, if the gravity-gradient data do not have enough resolution, the estimated  $v_p \times s$  curve presents multiple minima of  $s$  produced by 3-D estimated source with different maximum depths. In this case, among these minima of  $s$  producing virtually the same data fit, the one associated with the minimum depth to the bottom of the source and producing an acceptable data fit is chosen as the *optimum* estimate.

By analyzing the histograms of the residuals between the observed and predicted gravity-gradient data, we show that our method is able to identify systematic errors and to correct the gravity-gradient data for these errors. If the corrected gravity-gradient data have sufficient resolution our method obtains a stable estimate which recovers the geometry of the geologic body completely. On the other hand, if the corrected gravity-gradient data have insufficient resolution our method obtains a stable estimate which retrieves the upper part of the body only. In this case, the estimated 3-D source has the minimum volume and the minimum depth to the bottom which is required to yield an acceptable data fit.

In comparison with inverse methods that estimate the density-contrast distribution within a user-specified grid of 3D right, juxtaposed prisms in the horizontal and vertical directions, our method is more computationally efficient because it does not require an intractable number of parameters and consequently does not deal with a large-scale 3-D inverse problem. Our method

requires neither the use of depth-weighting functions adopted as a strategy to estimate sources at their correct depths nor the introduction of compactness and homogeneity constraints on the actual sources. On the other hand, our method is restricted to isolated bodies and assumes the knowledge about the correct depth of the top and density contrast of the 3-D geologic body.

Our method can be extended, for example, to estimate the 3-D shape of multiple bodies producing interfering gravity-gradient anomalies, to perform a joint-inversion of gravity and gravity-gradient data and to invert magnetic data. Additionally, in order to overcome problems with local minima, other optimization methods combining gradient-based and heuristic strategies could be employed.

## REFERENCES

- Barbosa, V.C.F. & Silva, J.B.C., 1994. Generalized compact gravity inversion, *Geophysics*, **59**, 57–68.
- Barbosa, V.C.F., Silva, J.B.C. & Medeiros, W.E., 1997. Gravity inversion of basement relief using approximate equality constraints on depths, *Geophysics*, **62**, 1745–1757.
- Barbosa, V.C.F., Silva, J.B.C. & Medeiros, W.E., 1999. Gravity inversion of a discontinuous relief stabilized by weighted smoothness constraints on depth, *Geophysics*, **64**, 1429–1437.
- Barbosa, V.C.F. & Silva, J.B.C., 2011. Reconstruction of geologic bodies in depth associated with a sedimentary basin using gravity and magnetic data, *Geophys. Prospect.*, **59**, 1021–1034.
- Barnes, G. & Barraud, J., 2012. Imaging geologic surfaces by inverting gravity gradient data with depth horizons, *Geophysics*, **77**, G1–G11.
- Beiki, M. & Pedersen, L. B., 2010. Eigenvector analysis of gravity gradient tensor to locate geologic bodies, *Geophysics*, **75**, I37–I49.

- Bertete-Aguirre, H., Cherkaev, E. & Oristaglio, M., 2002. Non-smooth gravity problem with total variation penalization functional, *Geophys. J. Int.*, **149**, 499–507.
- Caratori-Tontini, F., Cocchi, L. & Carmisciano, C., 2009. Rapid 3-D forward model of potential fields with application to the Palinuro seamount magnetic anomaly (southern Tyrrhenian Sea, Italy), *J. Geophys. Res.*, **114**, B02103.
- Coker, M. O., J. P. Bhattacharya, and K. J. Marfurt, 2007, Fracture patterns within mudstones on the flanks of a salt dome: Syneresis or slumping?: *Gulf Coast Association of Geological Societies Transactions*, **57**, 125-137.
- Ennen, C. & Hall, S., 2011. Structural mapping of the Vinton salt dome, Louisiana, using gravity gradiometry data, In: SEG Annual Meeting, *SEG International Exposition and 83rd Annual Meeting*, San Antonio, 18-23 September 2011, SEG.
- Farquharson, C. G., 2008. Constructing piecewise-constant models in multidimensional minimum-structure inversions. *Geophysics*, **73**, K1–K9.
- Fregoso, E. & Gallardo, L. A., 2009. Cross-gradients joint 3-D inversion with applications to gravity and magnetic data, *Geophysics*, **74**, L31–L42.
- Gordon, A. C., Mohriak, W. U. & Barbosa, V. C. F., 2012. Crustal architecture of the Almada Basin, NE Brazil: An example of a non-volcanic rift segment of

the South Atlantic passive margin, in *Conjugate divergent margins*, Vol. 369, eds Mohriak, W.U., Danforth, A., Post, P. J., Brown, D. E., Tari, G. C., Nemcok, M. & Sinha, S. T., Geological Society London Special Publications, London.

Guillen, A. & Menichetti, V., 1984. Gravity and magnetic inversion with minimization of a specific functional, *Geophysics*, **49**, 1354–1360.

Guspí, F., 1993. Noniterative nonlinear gravity inversion, *Geophysics*, **58**, 935–940.

Last, B.J. & Kubik, K., 1983. Compact gravity inversion, *Geophysics*, **48**, 713–721.

Lelièvre, P.G. & Oldenburg, D.W., 2009. A comprehensive study of including structural orientation information in geophysical inversions, *Geophys. J. Int.*, **178**, 623–637.

Li, Y., 2001. 3-D inversion of gravity gradiometer data, 71st Annual International Meeting, SEG, Expanded Abstracts, 1470–1473.

Li, Y. & Oldenburg, D.W., 1998. 3-D inversion of gravity data, *Geophysics*, **63**, 109–119.

- Luo, X., 2010. Constraining the shape of a gravity anomalous body using reversible jump Markov chain Monte Carlo, *Geophys. J. Int.*, **180**, 1067–1089.
- Marquardt, D. W., 1963. An algorithm for least-squares estimation of nonlinear parameters, *J. Soc. Ind. Appl. Math.*, **2**, 601–612.
- Martins C.M., Barbosa V.C.F. & Silva J.B.C., 2010. Simultaneous 3-D depth-to-basement and density-contrast estimates using gravity data and depth control at few points, *Geophysics*, **75**, I21–I28.
- Martins C.M., Lima W.A., Barbosa V.C.F., & Silva J.B.C. 2011. Total variation regularization for depth-to-basement estimate: Part 1 – Mathematical details and applications, *Geophysics*, **76**, I1–I12.
- Mikhailov, V., Pajot, G., Diament, M. & Price, A., 2007. Tensor deconvolution: A method to locate equivalent sources from full tensor gravity data, *Geophysics*, **72**, I61–I69.
- Moraes, R.A.V. & Hansen, R.O., 2001. Constrained inversion of gravity fields for complex 3-D structures, *Geophysics*, **66**, 501–510.
- Oezsen, R., 2004. Velocity modelling and prestack depth imaging below complex salt structures: A case history from on-shore Germany, *Geophys. Prospect.*, **52**, 693–70.

- Oliveira Jr, V.C., Barbosa, V.C.F. & Silva, J.B.C. 2011. Source geometry estimation using the mass excess criterion to constrain 3-D radial inversion of gravity data, *Geophys. J. Int.*, **187**, 754–772.
- Parker, R.L., 1973. The rapid calculation of potential anomalies. *Geophys. J. Roy. Astr. S.*, **31**, 447–455.
- Plouff, D., 1976. Gravity and magnetic fields of polygonal prisms and application to magnetic terrain corrections, *Geophysics*, **41**, 727–741.
- Portniaguine, O. & Zhdanov, M.S., 1999. Focusing geophysical inversion images, *Geophysics*, **64**, 874–887.
- Richardson, M.R. & MacInnes, S.C., 1989. The inversion of gravity data into three-dimensional polyhedral models, *J. Geophys. Res.*, **94**, 7555–7562.
- Silva, J.B.C., Medeiros, W. E. & Barbosa, V.C.F., 2001. Pitfalls in nonlinear inversion, *Pure Appl. Geophys.*, **158**, 945–964.
- Silva, J.B.C. & Barbosa, V.C.F., 2004. Generalized radial inversion of 2D potential field data, *Geophysics*, **69**, 1405–1413.
- Silva, J.B.C. & Barbosa, V.C.F., 2006. Interactive gravity inversion, *Geophysics*, **71**, J1–J9.

- Silva, J.B.C., Medeiros, W.E. & Barbosa, V.C.F., 2000. Gravity inversion using convexity constraint, *Geophysics*, **65**, 102–112.
- Silva, J.B.C., Oliveira, A.S. & Barbosa, V.C.F., 2010. Gravity inversion of 2D basement relief using entropic regularization, *Geophysics*, **75**, 129–135.
- Silva Dias, F.J.S., Barbosa, V.C.F. & Silva, J.B.C., 2007. 2D gravity inversion of a complex interface in the presence of interfering sources, *Geophysics*, **72**, 113–122.
- Silva Dias, F.J.S., Barbosa, V.C.F. & Silva, J.B.C., 2009. 3-D gravity inversion through an adaptive learning procedure, *Geophysics*, **74**, 19–121.
- Silva Dias, F.J.S., Barbosa, V.C.F. & Silva, J.B.C., 2011. Adaptive learning 3-D gravity inversion for salt-body imaging, *Geophysics*, **76**, 149–157.
- Telford, W. M., Geldart, L. P. & Sheriff, R. E., 1990. *Applied Geophysics*. New York: Cambridge University Press.
- Tikhonov, A.N. & Arsenin, V.Y., 1977. *Solutions of Ill-Posed Problems*. Washington: W. H. Winston & Sons.
- Uieda, L. & Barbosa, 2012. Robust 3-D gravity gradient inversion by planting anomalous densities, *Geophysics*, **77**, G55–G66.

Wildman R.A. & Gazonas, G.A., 2009. Gravitational and magnetic anomaly inversion using a tree-based geometry representation, *Geophysics*, **74**, 123–135.

Zhang, C., Mushayandebvu, M. F., Reid, A. B., Fairhead, J. D. & Odegard, M. E., 2000. Euler deconvolution of gravity tensor gradient data, *Geophysics*, **65**, 512–520.

Zhdanov, M. S., Ellis, R. & Mukherjee, S., 2004. Three-dimensional regularized focusing inversion of gravity gradient tensor component data, *Geophysics*, **69**, 925–937.